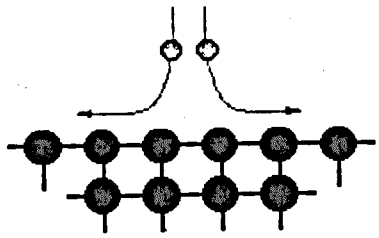

SURFACE SCIENCE RESEARCH CENTRE

"Charge Transfer and Disorder Broadening in Disordered Transition Metal Alloys."

Thesis submitted in accordance with the requirements of the University of Liverpool for the degree of Doctor in Philosophy

By

Angus William Newton

February 2001

Contents

Abstract

Acknowledgements

Abstract

In the following work, the charge transfer in disordered transition metal alloys is investigated. Four alloy systems are studied and they are CuPt, NiPt, AgPd and CuPd. The charge transfer is determined using two methodologies. The first method utilises core level photoelectron lineshapes obtained from the elements in the alloys and analyses them in terms of a potential model.

The second method interprets the shift in the binding energy and Auger peaks in terms of charge transfer. The two methods used for determining the charge transfer are then compared and the conclusions drawn.

The influence of surface preparation techniques on the core level lineshapes obtained from the alloys is investigated. A determination of the magnitude of the charge transfer in the four alloy systems is then made.

Acknowledgements

Writing this thesis was probably the hardest and most stressful thing that I have ever done. I feel immensely proud that it is finished and that the work is of a high standard. There are so many people to thank and I apologise to anyone who I forget to mention.

The biggest thanks must go to my supervisor Peter. A more knowledgeable and kind man you will never meet. His endless enthusiasm for research and his students is unsurpassed and without his influence and belief in me I would not have submitted my thesis.

The personnel who work in the surface science research centre are good people and I have enjoyed working with them all. John Murray is one said person and I will miss our deep and meaningful chats in the corridor, but I must learn to forgive him for being a Liverpool FC supporter. Big thanks to all the lads in the zoo who have helped create the joyful banter including Ben (Oldham), Julian (France), Michael (Germany), and the token scouser Erik. Must include the resident Mick (John H) who I heard about more than seen.

My family must get huge thanks for their patients with me during my long academic career and the almost endless financial help. Thanks to Mum, Dad, Helen and Ian, oh and the dog Andy who will sadly not be long of this earth.

This last thank you is for the most important person in my life, my girlfriend Louise. What a wonderful, loving, caring, beautiful and kind person you are and I hope you realise how much you mean to me. Thank you for being there. Louise's family have been extremely kind to me and I wish to thank all of them a great deal, from Mad Max to Dizzy Lizzy.

Thank you. Enjoy.

CHAPTER 1.

Preface

Alloys are strange things. You think you understand them, and then you change one constituent with the next element along in the periodic table and its all gone wrong!

Most of this thesis tries to gain a deeper understanding of charge transfer in disordered polycrystalline alloys. Four alloys have been studied and the mass of data analysed has been huge. The alloys are CuPt, NiPt, AgPd and CuPd. The previous work on this subject covered the CuPd alloy system [1-4] and so little is known about the factors, which may enhance or reduce the amount of charge transfer which one alloy system may possess to another. Therefore, this work endeavours to characterise which elements may be alloyed together to enable us to investigate the charge transfer further.

The CuPt alloy system was the first to be studied after the CuPd work [1-4]. There are a few reasons for doing this. Obviously, one alloy constituent is unchanged (Cu) and the other is replaced with the next one down in the periodic table group (Pd – Pt). Pt is a much larger atom than that of Pd and therefore relativistic effects must be accounted for in its bandstructure. Below in Figure a, is the calculated bandstructure for Cu near the Fermi energy [5].

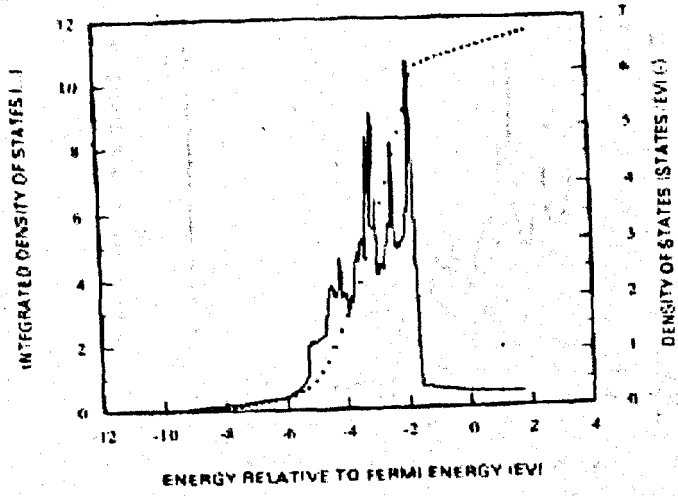

Figure a: - Calculated Bandstructure of Cu metal.

One can see from figure a above that the d band of Cu lies ~2eV from the Fermi energy (E_f) . The band structure at E_f is s-p in character. Below in figure b, the Pt bandstructure is shown [6].

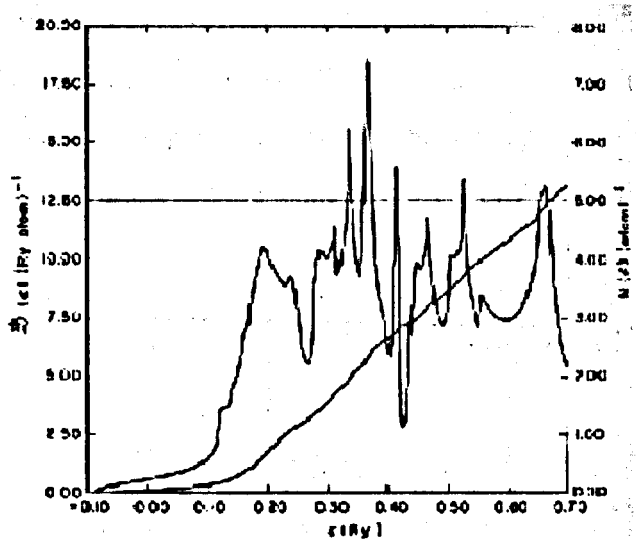

Figure b: - Calculated Bandstructure of Pt metal.

One can see in Figure b above that the Pt density of states at the Fermi level is much greater than that for Cu. Therefore, from studying this alloy system we would expect to see a similar magnitude of charge transfer as that found in CuPd [1-4] as the band structure is not dissimilar.

NiPt was the next alloy system studied. The Ni bandstructure is shown below in figure c.

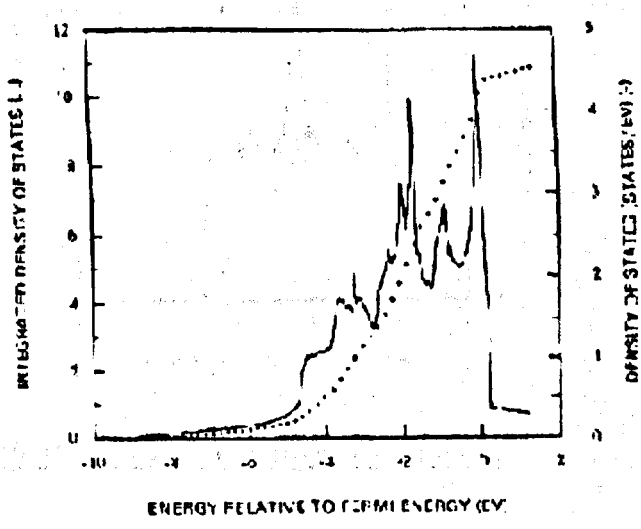

Figure c: - Calculated Bandstructure of Ni metal.

Ni and Pt have very similar bandstructures (Fig b and c) and this alloy system was chosen because of this fact. Both elements belong to the same group in the periodic table and so one would expect that this alloy system would have little charge transfer between one constituent element and the other.

AgPd alloys were the next alloy to be investigated. The elements are in adjoining groups in the periodic table, but have very different bandstructures. Below in Figure d and e are the bandstructures for Ag and Pd respectively.

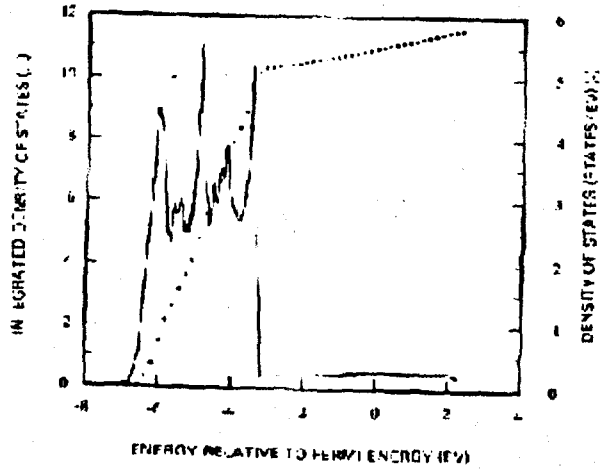

Figure d: - Calculated Bandstructure of Ag metal.

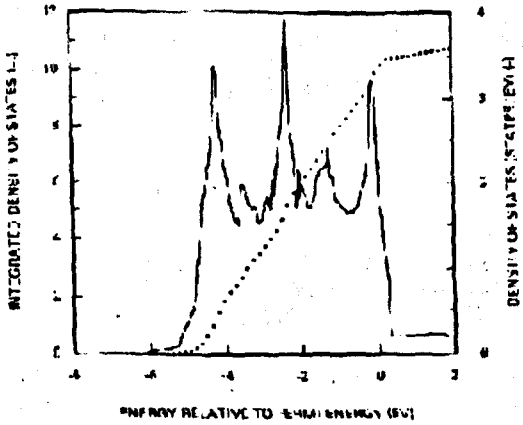

Figure e: - Calculated Bandstructure of Pd metal.

The d band of Pd is at the E_f and for Ag the d band is 3.3eV away from the Fermi level. This alloy system was studied because we expected it to have greater

charge transfer because of the varying band structure. Also, when these two elements are alloyed, no ordered phases are present.

Finally, the CuPd alloy system was investigated again to recheck the previous work [1-4] and conclude this work.

1. INTRODUCTION

1.1 X-Ray Photoelectron Spectroscopy

X-ray photoelectron spectroscopy (XPS) is an important tool in many fields including surface science. The majority of the experimental data collected for this thesis was done using X-ray photoelectron spectroscopy (XPS). The technique is very versatile and enables the user to gain much information about the chemical surface of a sample. XPS can be used for core-level to surface elemental studies with a degree of accuracy that is heavily dependent on the characteristics of the apparatus. There are three main types of spectra that have been collected for this work using XPS (or angled XPS): core-level, Auger and valence band.

1.11 The Photoelectric Effect

In 1905, Einstein [7] used quanta theory to explain the photoelectric effect. He assumed that light has its energy concentrated in little packets or 'light quanta', and that the energy of each of these quanta was:

$$E = h\nu \tag{1.1}$$

h was Planck's constant with ν being the light frequency. Many experiments have proved this relation for the photon and it is fundamental to the understanding of the photoelectric effect. If we shine light onto a metallic surface, with correct conditions, then we will get the emission of photoelectrons. The energy of these electrons is heavily dependant on the type of incident radiation and the specific elements used for the illuminated sample. The kinetic energy of the electrons E_e obtained from the sample is found from:

$$E_e = h\nu - E_b - \phi_s \tag{1.2}$$

Where hν is the incident photon energy, E_b is the binding energy of the energy level that the photoelectron originated from and ϕ_s is the work function of the spectrometer. The work function of a material can range from 1-10eV. A graphical representation of the photoelectric effect is shown below in Fig1.1

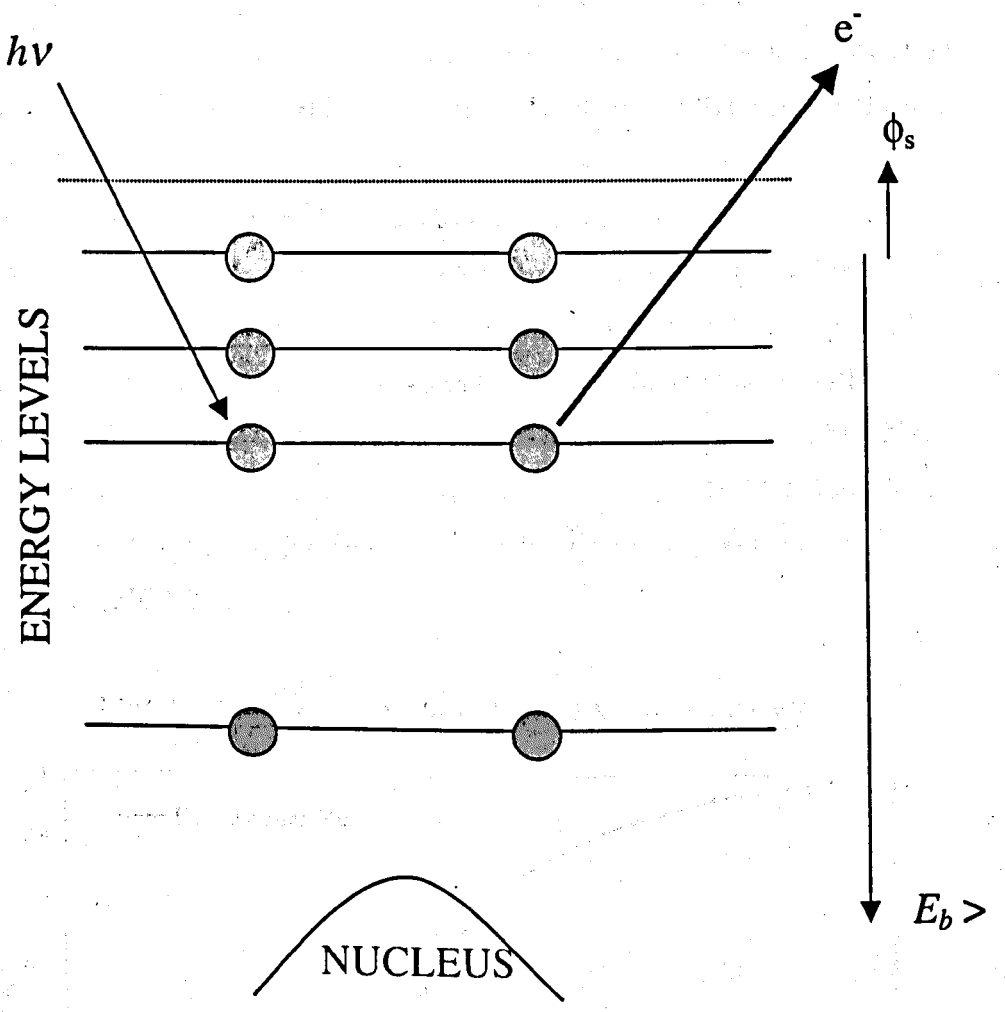

FIGURE 1.1: The Photoelectric effect.

1.12 X-RAYS

X-rays were discovered by Rontgen during the latter stages of the 19th century. The wavelength of x-rays vary from $10^{-9} \rightarrow 10^{-15}$m. They have high energy and high penetration into matter. Several elements have an intrinsic x-ray energy that is utilised in XPS. The three most commonly used, as sources are Aluminium, Copper and Titanium. For experimentation an anode of the

specific material is bombarded with high-energy electrons (~15keV), characteristic X-ray emission lines from the sample are then produced. In addition to the X-rays, a continuous breaking radiation or Bremsstrahlung is observed. This is caused by the high energy incident electrons being in the vicinity of the nucleus, the strength of the effect increases as the fourth power of the atomic number (Z^4) increases i.e. it is proportional to the nuclear charge. The energy of this radiation is a function of the energy of the incident electron beam. Therefore, in order to reduce noise in the XPS spectrum it is advantageous to use an anode with a low atomic number.

When an incident photon impinges on a sample, it may interact in three different ways: Compton scattering, pair production and photo-ionisation. If the energy of the incident photon is less than 10eV, then the latter will dominate. Once photo-ionisation occurs, two decay chains are possible: X-ray fluorescence (FIG1.1 above) and the Auger processes (FIG1.3A below). The dominance of one decay process over the other depends upon the atomic number Z (FIG1.2 below).

Fig1.2: Fluorescence Yield of K shell X-rays against Z

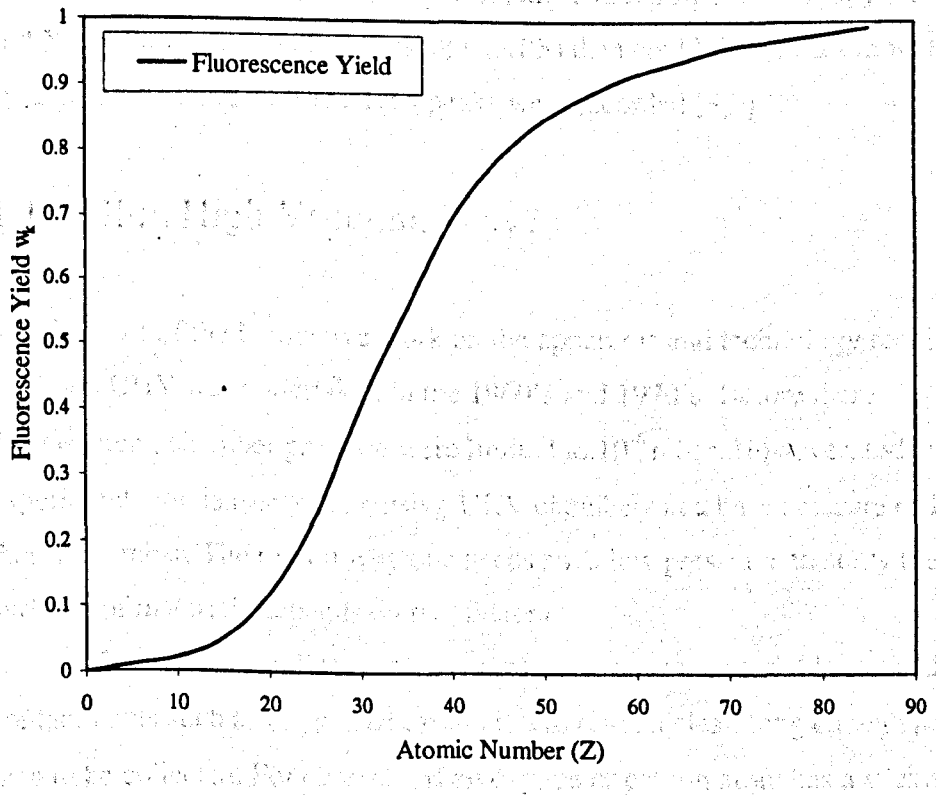

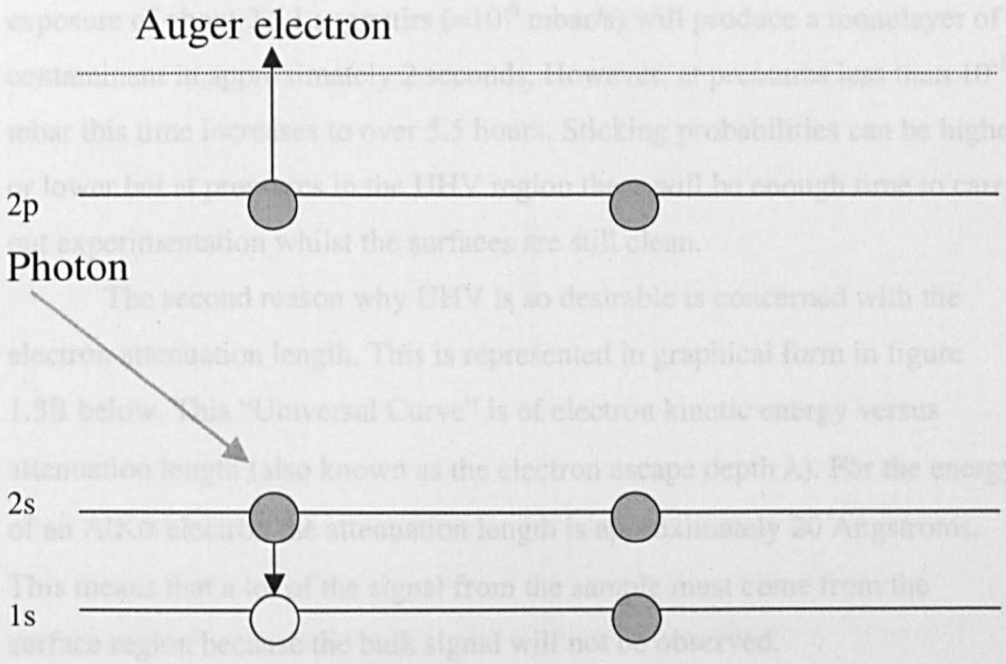

FIGURE 1.3A: Auger Process.

Much work was done on x-rays in the early part of last century, since X-rays can be detected in air. The XPS technique only came into its own as a surface sensitive tool in the 1960's with the invention of Ultra High Vacuum (UHV) chambers and high-resolution analysers. Auger Electron Spectroscopy (AES) and X-ray Photoelectron Spectroscopy (XPS) data could then be taken with good resolution and well-resolved peaks were recorded.[8,9]

1.13 Ultra High Vacuum, Why?

Most of the innovative work on the apparatus and technology required to obtain UHV was undertaken in the 1960's and 1970's. Before there development, chamber pressure were limited to 10^{-6} mbar. However, today experimentation is easily done using UHV chambers at a base pressure of less than 10^{-10} mbar. The reason why one needs such low pressures to study the surfaces of materials depends on two factors.

The first is cleanliness. At low pressures, once a material is cleaned of contaminants such as oxygen or carbon it will remain clean long enough for data to be collected. For example, if an oxygen or carbon atom has a sticking probability of 0.5, (if two atoms hit a surface then one will stick) then an

exposure of about 2.5 Langmuirs (=10^{-6} mbar/s) will produce a monolayer of contaminant in approximately 2 seconds. However, at pressures less than 10^{-10} mbar this time increases to over 5.5 hours. Sticking probabilities can be higher or lower but at pressures in the UHV region there will be enough time to carry out experimentation whilst the surfaces are still clean.

The second reason why UHV is so desirable is concerned with the electron attenuation length. This is represented in graphical form in figure 1.3B below. This "Universal Curve" is of electron kinetic energy versus attenuation length (also known as the electron escape depth λ). For the energy of an AlKα electron the attenuation length is approximately 20 Angstroms. This means that a lot of the signal from the sample must come from the surface region because the bulk signal will not be observed.

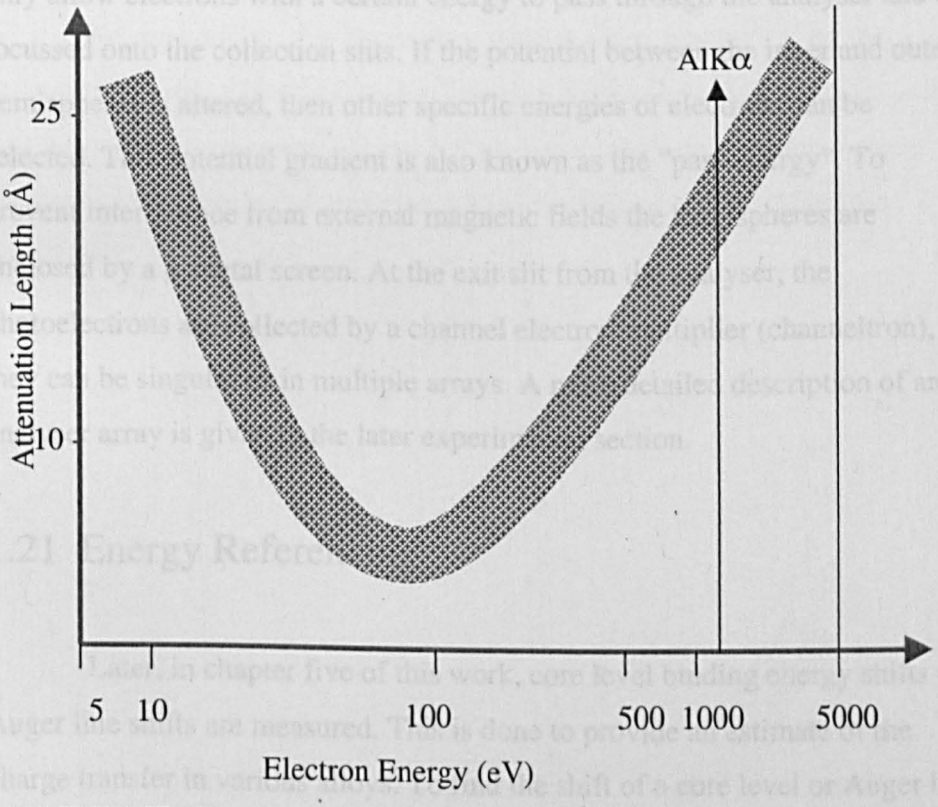

FIGURE 1.3B: The 'Universal Curve'.

1.2 High Resolution Analysers

To detect photoelectrons on an UHV chamber; hemi-spherical analysers are the preferred choice. The resolution (ΔE) obtained from an

analyser is dependant on three parameters, the slit width (ΔR), the sphere radius of the hemisphere (R) and the pass energy (E). It is derived from the Rudd equation [10]: -

$$\frac{\Delta E}{E} = \frac{\Delta R}{2R} \qquad (1.3)$$

A hemispherical analyser consists of three parts, the electrostatic lens, hemispherical analyser and the detector. The lens is used to retard the electrons then focus the electron beam onto the entrance slit of the hemisphere. There are various potentials applied to the inner and outer hemispheres, which creates a potential difference between them. This will only allow electrons with a certain energy to pass through the analyser and be focussed onto the collection slits. If the potential between the inner and outer hemispheres is altered, then other specific energies of electrons can be selected. This potential gradient is also known as the "pass energy". To prevent interference from external magnetic fields the hemispheres are enclosed by a μ-metal screen. At the exit slit from the analyser, the photoelectrons are collected by a channel electron multiplier (channeltron), they can be singular or in multiple arrays. A more detailed description of an analyser array is given in the later experimental section.

1.21 Energy Referencing

Later, in chapter five of this work, core level binding energy shifts and Auger line shifts are measured. This is done to provide an estimate of the charge transfer in various alloys. To find the shift of a core level or Auger line, we must reference the position of the photoelectron peak to a fixed point. The reference point used is the Fermi level (E_f). It is important to note that photoelectrons entering the analyser of the spectrometer are subject to a number of potentials which generate accelerating or retarding forces. If the zero of energy for the spectrometer (E^{spec}) differs from that of the Fermi level

then we must include a correction term ϕ_{spec}. The binding energy of a core level electron then becomes: -

$$E(i)_b^f = h\nu - E_k(i) - \phi_{spec} \qquad (1.4)$$

and the kinetic energy of the Auger electron: -

$$E(i)_k^f = E_k(i) + \phi_{spec} \qquad (1.5)$$

where $E_k(i)$ is the measured kinetic energy of the photoelectron, hν is the energy of the excitation source and ϕ_{spec} is the correction term or spectrometer work function.

We can confirm that the energy scale is linear by calibrating the spectrometer with a known core level energy e.g. $Cu2p_{3/2}$ and checking that E_f is at zero. Using equations 1.4 and 1.5 we are able to reference all energies to the Fermi level. Figure 1.4 presents the energy references considerations graphically.

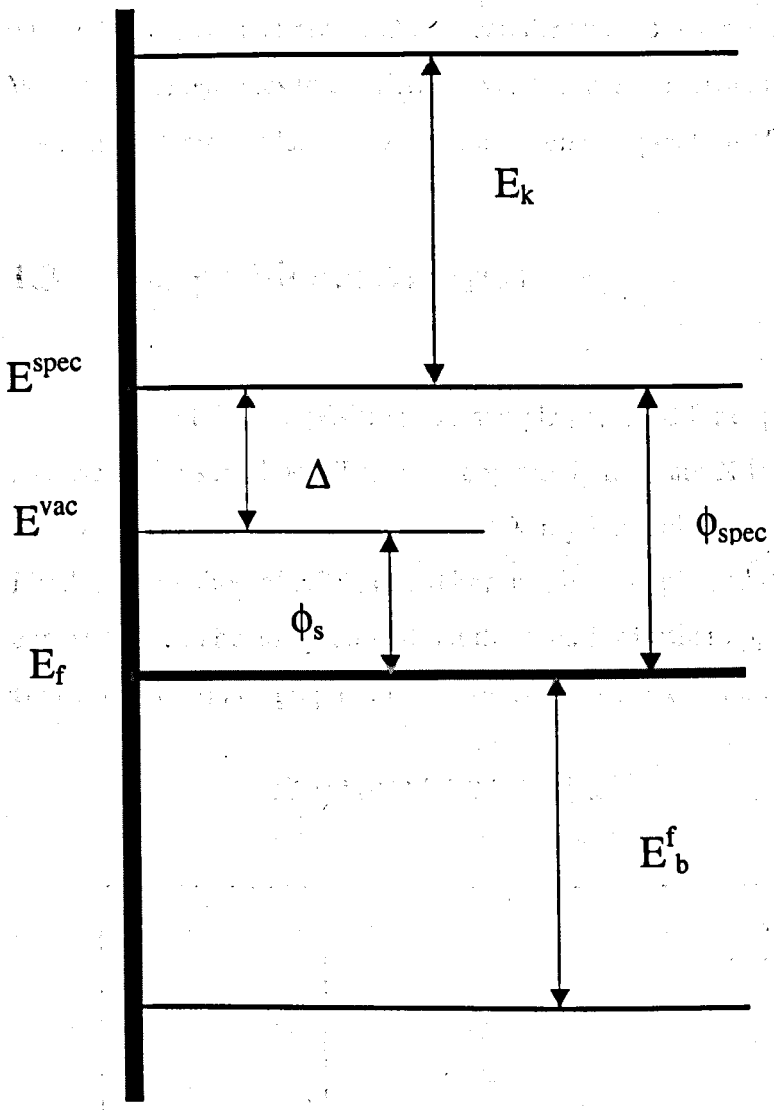

FIGURE 1.4: Energy level diagram defining E^{vac}, E^f to E_b and E_k.

One of the quantities in FIG 1.4, E^{vac}, has not been defined yet. It is the vacuum zero, which is the energy at which an electron is at zero potential. It can be seen that the energy of E^{vac} is related to the Fermi level by the sample workfunction ϕ_s. Similarily, the zero of the spectrometer scale (E^{spec}) is related to the Fermi level by the spectrometer workfunction ϕ_{spec}. It can be shown: -

$$\phi_{spec} - \phi_s = E^{spec} - E^{vac} = \Delta \qquad (1.6)$$

where Δ is the contact potential between the spectrometer and the specimen. We reference energies to the Fermi level because the errors in experimentally calculating Δ are too large to ascertain the energy position of E^{vac}.

1.3 Compositional Analysis

To find the composition of a sample prepared for experimentation, we can use various methods. The most commonly used are X-ray diffraction (XRD), X-ray fluorescence (XRF) and X-ray Photoelectron Spectra (XPS). Firstly, the method of XPS is used because it is simple and the data from the experiment can be analysed without the need for further apparatus or time. Below (FIG1.5) is a graph of the broad scan from $Cu_{50}Pt_{50}$ alloy.

Broad scan from $Cu_{50}Pt_{50}$ Alloy.

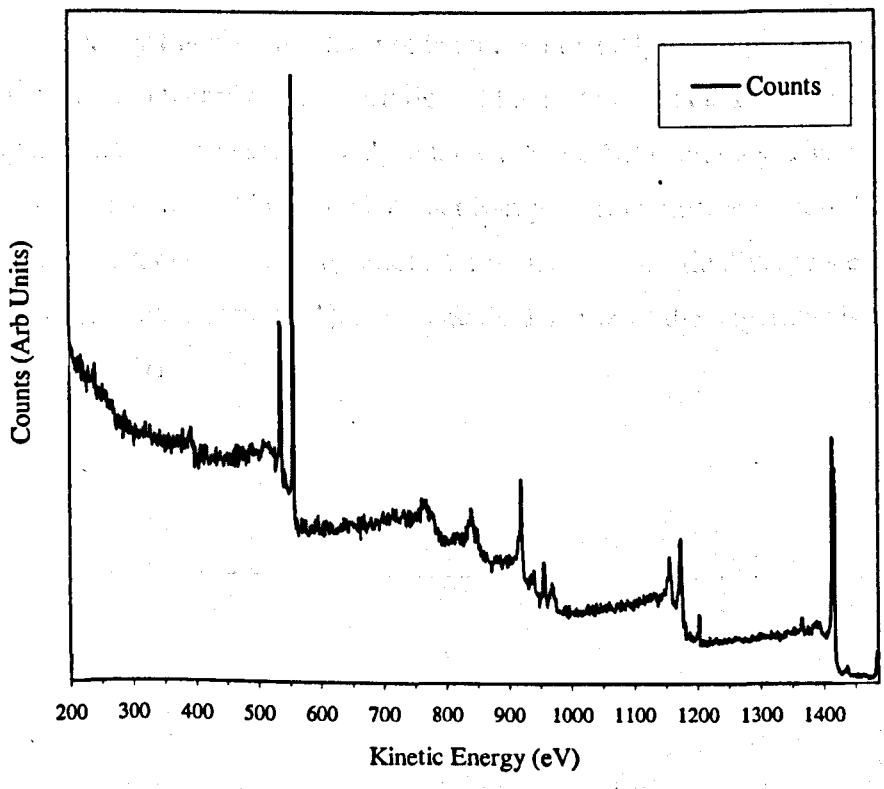

FIGURE 1.5: Broad scan from 50/50 CuPt alloy.

This is the raw data, counts versus kinetic energy. We can use this data to find the composition of an A_xB_{1-x} sample. The important parameters needed are the counts (N((A)B)), the escape depth of the A(B) atom (λ), the cross-section of the chosen core level (σ), and finally a multiplicative factor α. Alpha allows for the variation in sensitivity of the analyser with the kinetic energy of the photoelectron. If both core levels are similar in binding energy then α will be 1.We have: -

$$\frac{I(A)}{I(B)} = \frac{N(A)\sigma(A)\lambda(A)}{N(B)\sigma(B)\lambda(B)} \qquad (1.7)$$

Where I(A) / I(B) is the ratio of the photoelectron intensities observed from the core levels of the constituent elements. This method is very good technique for gaining composition information and an accuracy of ±1% can be obtained.

X-ray fluorescence has not been used to analyse sample composition in this work and therefore, a description of the technique is not included here. X-ray diffraction was used to analyse the CuPt and NiPt samples. The equipment used was a Phillips PW1840 Compact X-ray Diffractometer System. The diffractometer consists of a goniometer with an automatic divergence slit, X-ray source and detector [11]. A schematic diagram of the apparatus is shown below in FIG1.6: -

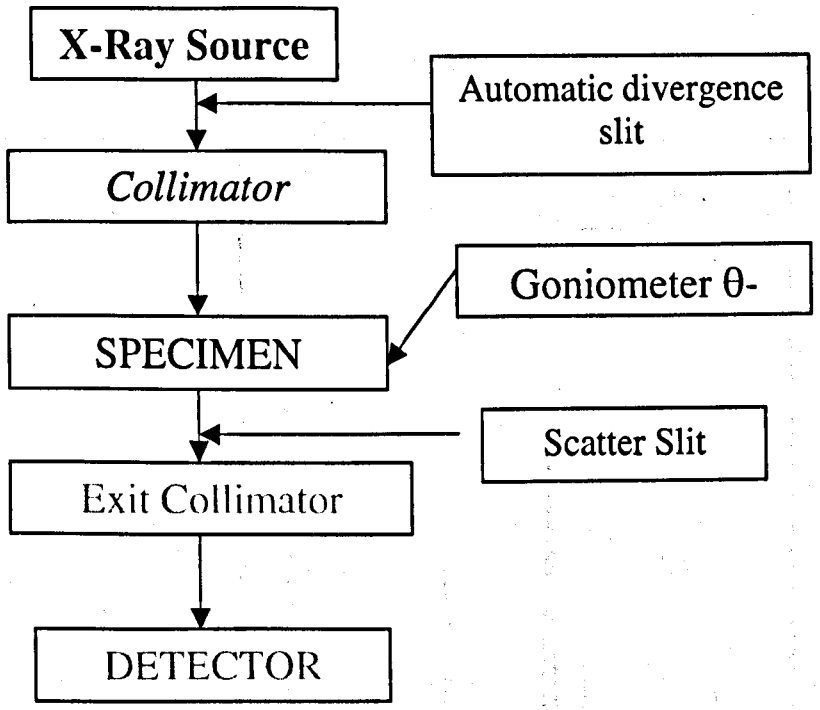

FIGURE 1.6: Schematic Diagram of a Phillips Diffractometer.

The Phillips diffractometer uses a copper anode as an x-ray source producing Kα radiation (λ=1542Å) with a nickel crystal used to filter out the Kβ radiation. The monochromated x-rays then pass through a collimator before hitting the sample at an angle θ. The angle of the sample is altered using a belt drive system which rotates the sample after the specified time period. The x-rays then pass through the exit collimator after being filtered for unwanted diffraction peaks such as those arising from the sample holder. The filter helps reduce the broadening to the lines and then the x-rays pass on to the detector.

The data is fed into a computer where software enables us to interpret each spectrum in terms of peak intensities and angle. The associated D value is then obtained. Below (FIG1.7) is a diffraction pattern obtained from a $Cu_{50}Pt_{50}$ alloy: -

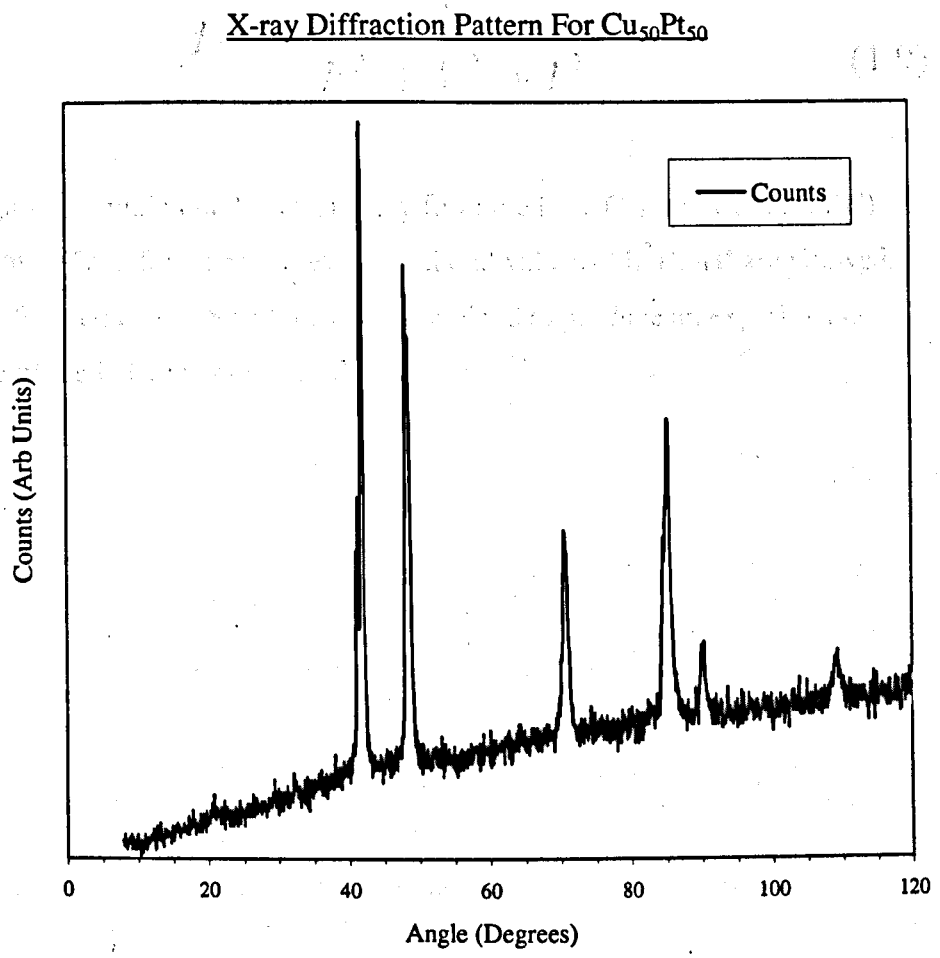

FIGURE 1.7: XRD Spectra from 50/50 CuPt Alloy.

1.31 X-ray Diffraction Theory

The theory used for diffraction is Bragg's Law:-

$$2D \sin \theta = n\lambda \qquad (1.8)$$

where D is the spacing between successive planes in the crystal lattice, λ is the wavelength of the x-rays used, n is the order of the diffraction and θ is the angle of diffraction. For a cubic lattice, with unit cell length 'a', using Pythagoras theorem we can show that the spacings between successive (hkl) planes is: -

$$D^2 = \frac{a^2}{h^2 + k^2 + l^2} \tag{1.9}$$

the samples studied in this thesis only form the Face Centred Cubic (FCC) structure. Therefore, only all even or all odd values of $h^2+k^2+l^2$ are allowed. Therefore, equations 8 and 9 can be combined to produce an experimental value of the lattice parameter 'a'.

1.4 References

[1] R.J. Cole, N.J. Brooks and P.Weightman,Phys. Rev. Lett. **78**, 3777 (1997).

[2] R.J. Cole, N.J. Brooks and P.Weightman, Phys. Rev. B **56**, 12178 (1997).

[3] R.J. Cole and P. Weightman,J. Phys: Condens. Matter **9**, 5609 (1997).

[4] R.J. Cole and P. Weightman,J. Phys: Condens. Matter **10**, 5679 (1998).

[5] V.L. Moruzzi, J.F. Janak and A.R. Williams, "*Calculated Electronic Properties of Metals.*" Pergamon 1978.

[6] A.H. MacDonald, J.M.Daams, S.H. Vosko and D.D. Koelling. Phys. Rev. B **23**, 6377 (1981).

[7] A.Einstein, Ann. Phys **17**, 132 (1905)

[8] K. Siegbahn *et al*, Nova Reg. Soc. Ups. Serv IV **20** 5 (1967)

[9] K. Siegbahn *et al*, ESCA Applied to Free Molecules (North Holland, Amsterdam, 1969)

[10] M. E. Rudd, in "Low Energy Electron Spectroscopy" K. D. Sevier New York: Wiley (1972)

[11] Philips PW1840 Diffractometer Instruction Manual

CHAPTER 2.

Experimental Details

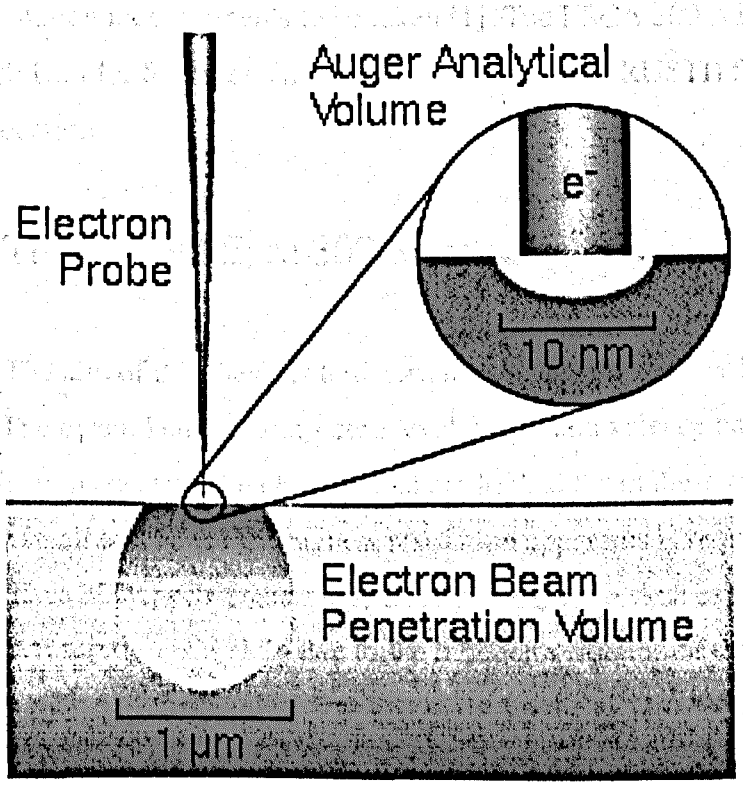

2.1 Introduction

This chapter describes the apparatus used and the theory behind it. The experimental data described in this thesis was collected over three years. All of the XPS data was collected using the SCIENTA ESCA 300 spectrometer, located at the Daresbury Laboratory, Warrington, UK. This spectrometer is used because of its high resolution x-ray monochromator that enables very high resolution measurements to be taken [1]. The ESCA 300 is situated at the Research Unit for Surfaces Transforms and Interfaces (RUSTI) facility at the above location.

2.11 The Scienta Esca 300 Spectrometer

The aim of this thesis is to determine the charge transfer in various alloys. The data taken include: - core level, auger and valence band photoelectron spectra. The changes that are looked for in these types of spectra are only small and hence the highest resolution apparatus is required. The Scienta Esca 300 spectrometer is particluarily suited to such experiments. The excellent resolution is mainly due to the monochronisation of the x-rays and the large radius of the hemispheres that make up the electrostatic analyser. The signal to noise ratio is increased by a special pre-focus lens which increases spatial resolution and a multi-channel detector system.

2.12 X-ray Source

The x-ray source on the Scienta consists of a rotating anode with a high power rotating electron gun. The diameter of the anode is 300mm. It is made of a high strength titanium alloy which on the outer rim incorporates a water cooled copper ring coated with aluminium. The anode uses a closed cycle pumping system. The other half of the copper ring is coated in titanium so both monochromated AlKα and TiKβ can be used for excitation. The titanium x-ray source is three times as energetic as the aluminium source and

so core levels with high binding energy and Auger electrons arising from excitation deep in atomic cores can also be studied.

The high power electron gun used to excite characteristic AlKα and TiKβ x-rays is a two stage Pierce-type electrostatic gun with a large emitting cathode surface in the second stage. The filament of the first stage, heats the cathode in the second stage by electron bombardment. The position of the focus can be altered mechanically from outside and so the operator can change between the AlKα and TiKβ radiation with a turn of a handle. A diagram of the Scienta is shown below in Fig2.1: -

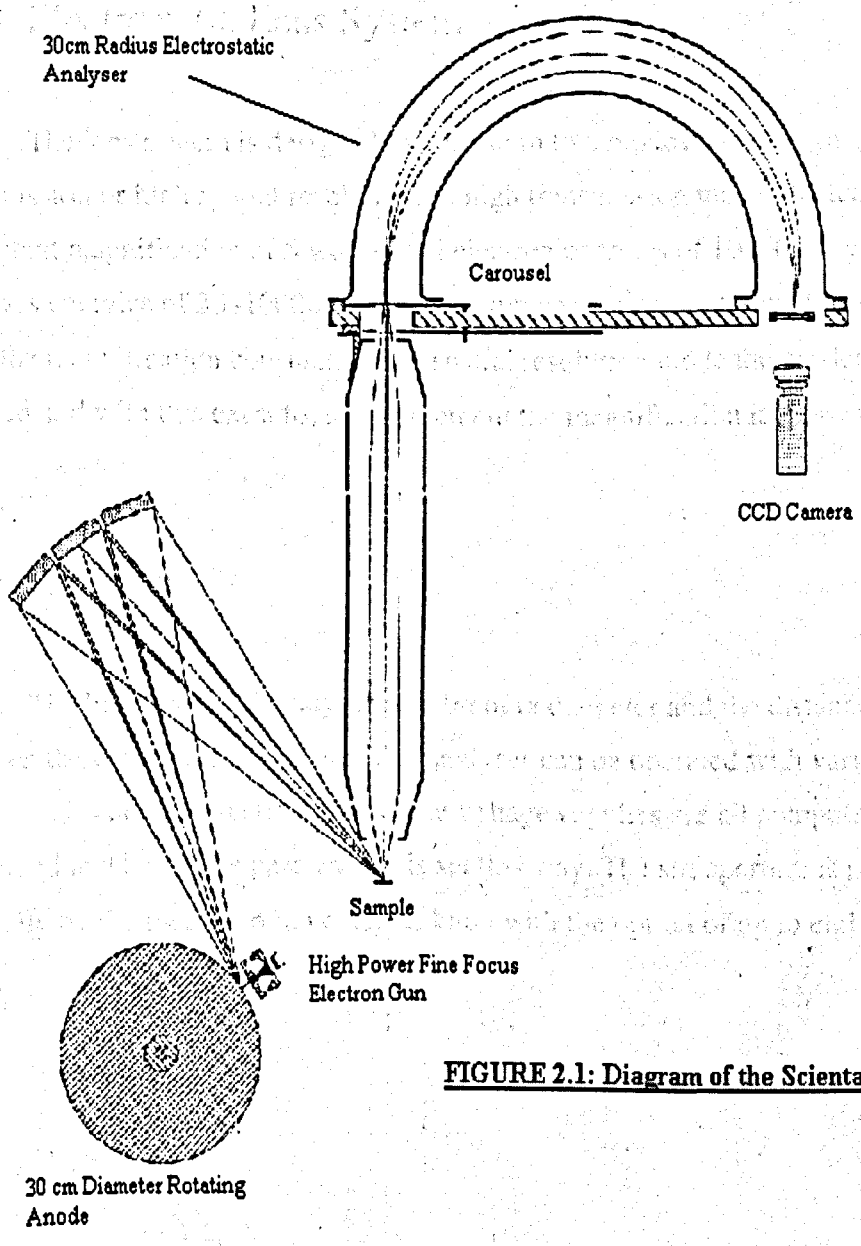

FIGURE 2.1: Diagram of the Scienta

The x-ray monochromator consists of seven double focussing three inch diameter quartz crystals. The thin single crystal wafers are quasi-toroidally bent to provide double focussing of the x-ray. The seven crystals are arranged with one in the centre and the other six in a close packed array around it. The crystals are placed on five Rowland circles of 650mm diameter all having a common source and focus. The temperature of the crystals is kept slightly above room temperature at 30°C with the use of two radiating lamps and are hence thermionically stabilised.

2.13 Electrostatic Lens System

The lens system is designed to operate in two modes, either high transmission or high spatial resolution. In high transmission mode, the lens has a constant magnification of 5 with initial electron energies of 100–6000 eV and pass energies of 20–1000eV. The lens voltages are computer controlled to keep the magnification constant. In the spatial resolution mode the pre-lens is inserted and with this extra focussing element the magnification increases to 10.

2.14 Analyser

The hemispherical analyser is 600mm in diameter and the distance between the electrodes is 100mm. The analyser can be operated with various pass energies and slit-aperture pairs. The voltage supplies are all computer controlled and hence the pass energy is set this way. The slit aperture is set manually by the rotation of an external knob with the option of up to eight slit pairs.

2.15 Detection System

To detect the photoelectrons leaving the analyser, a 2-dimensional position sensitive detection system is used. It utilises 2-micro-channel plates and a phosphor plate in series. The phosphor plate is much closer to the channel plates and the light spots are much smaller in size, hence increasing the spatial resolution. The CCD camera captures the images in real time and because the light sensitive elements are fixed on a silicon wafer it has the combined effect of increasing the spatial resolution.

2.16 Pumping Down to UHV

On the Scienta spectrometer, there are three main types of pump. They are the diffusion pump, turbo molecular pump and rotary pump. The hemispherical electrostatic analyser, main chamber and x-ray monochromator are all pumped by diffusion pumps. The diffusion pumps are backed by rotary pumps. The fast entry air lock and rotating anode are pumped by turbo molecular pumps.

The base pressure in the main chamber is $1x10^{-9}$ mbar and $1x10^{-8}$ mbar in the sample preparation chamber. The equipment is used on a weekly bases by various groups from all over the world and the pressure suffers because of this. Baking is only done twice a year to prevent damage to the analyser and with organic samples also experimented on, the pressure does not improve below the values quoted.

The pressure is still good enough to keep samples clean of contaminants such as oxygen and carbon for many hours therefore; experimental time is not an issue. The diagram below (FIG2.2) is a representation of the Scienta vacuum chamber.

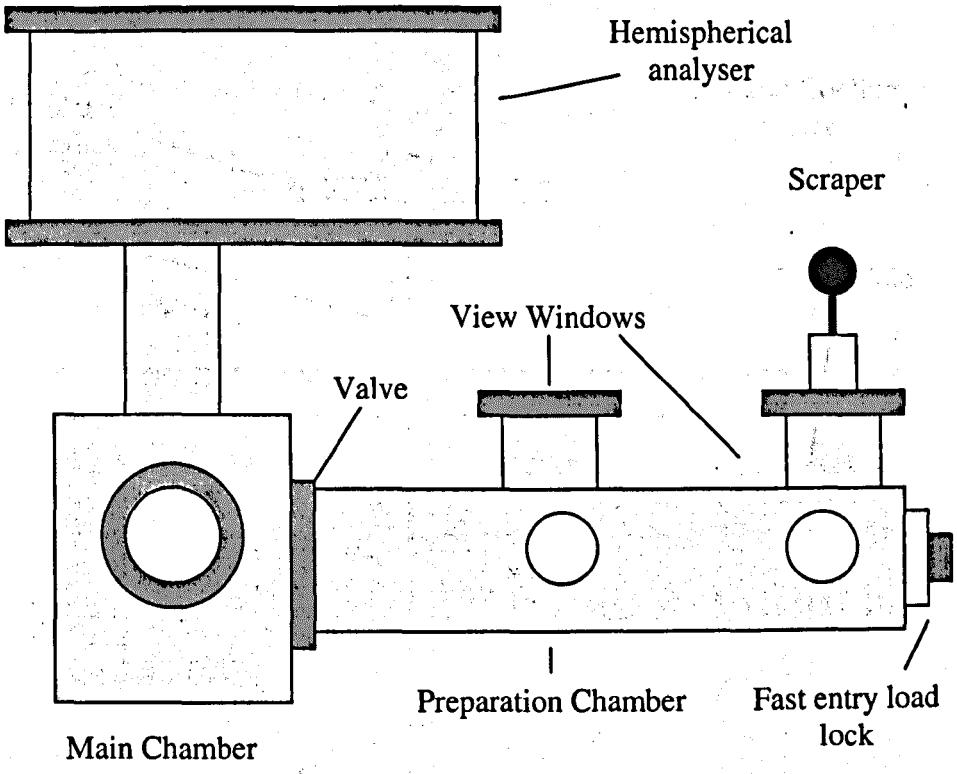

FIGURE 2.2: Scienta preparation chambers.

2.2 Sample Fabrication

The samples required for experimentation in this thesis were all disordered. This means that the fabrication was much less complex than if ordered specimens with specific planes were needed. The disorder was desirable because the broadening of core levels can only be seen if several sites are present on the volume of the specimen sampled in the experiments and not just a simple ordered phase. An in depth description of disorder broadening in given in chapter 3.

The four alloys studied in this work were CuPt, NiPt, AgPd and CuPd. They were all made in an arc furnace. A diagram of the arc furnace used is shown below in FIG2.3.

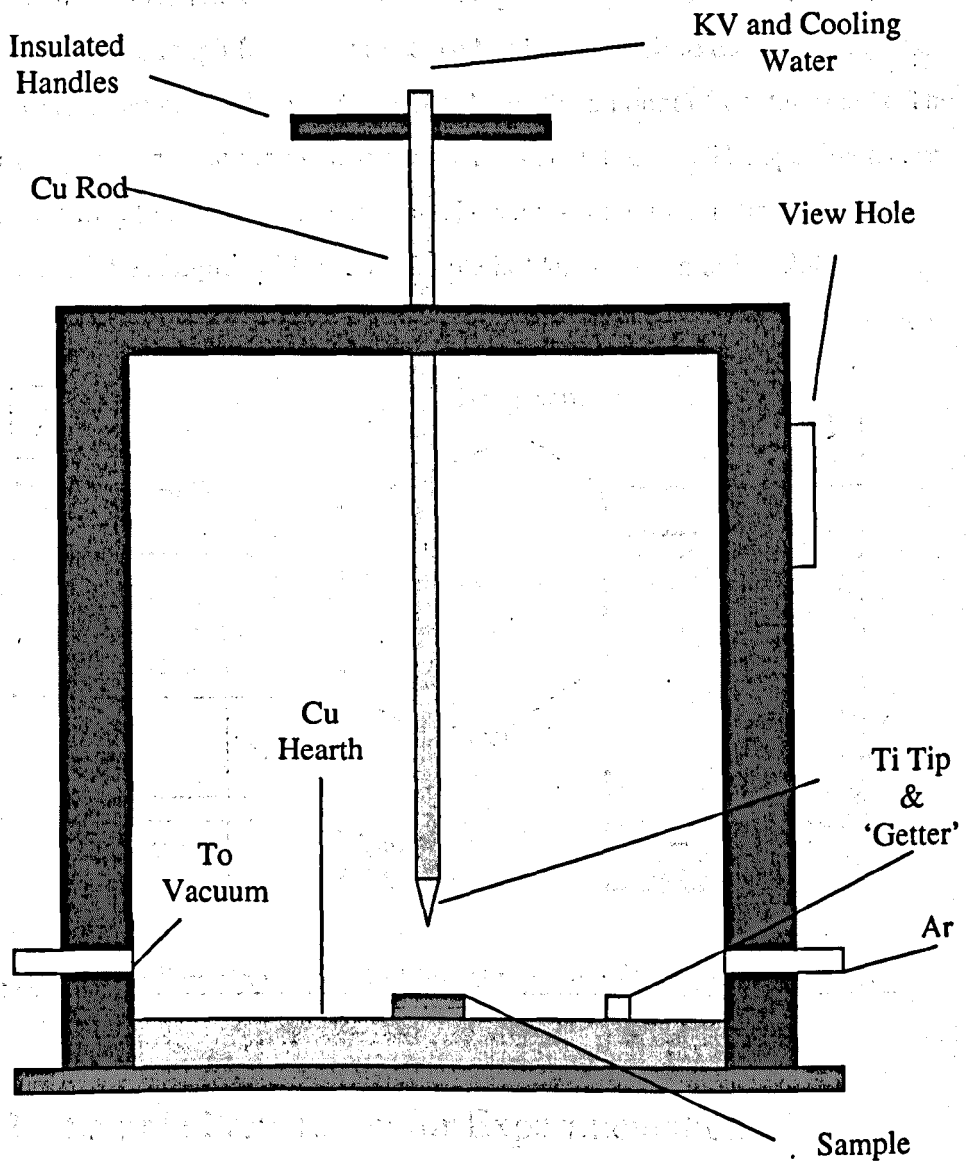

FIGURE 2.3: Arc Furnace Used in Sample Production.

Using the apparatus in FIG 2.3, disordered polycrystalline specimens were attained using the following method. Firstly, the correct weights of the elements in the alloys are collected. The elements are 99.99999% pure and bought in from Metal Crystals and Oxides of Cambridge. The raw materials are placed into the arc furnace and the chamber pumped down to $1x10^{-3}$ mbar. Argon (Ar) gas is then introduced and the pressure increased to just below that of atmosphere. The chamber is pumped down and then Ar gas introduced again. This step is repeated several times

to limit the amount of contaminants in the chamber. The pressure is then increased to approximately 450 Torr. The cooling water and high voltage are switched on. 450 Torr pressure is high enough for an arc to strike but low enough to eliminate flashes. The Ti getter is heated until white-hot which reduces the amount of contaminants. The constituent alloy materials are then co-melted with an electric arc. The specimens are melted several times to ensure homogeneity. The samples are then rolled and cut to the dimensions of the sample holder. The sample holder is shown in Fig 2.4.

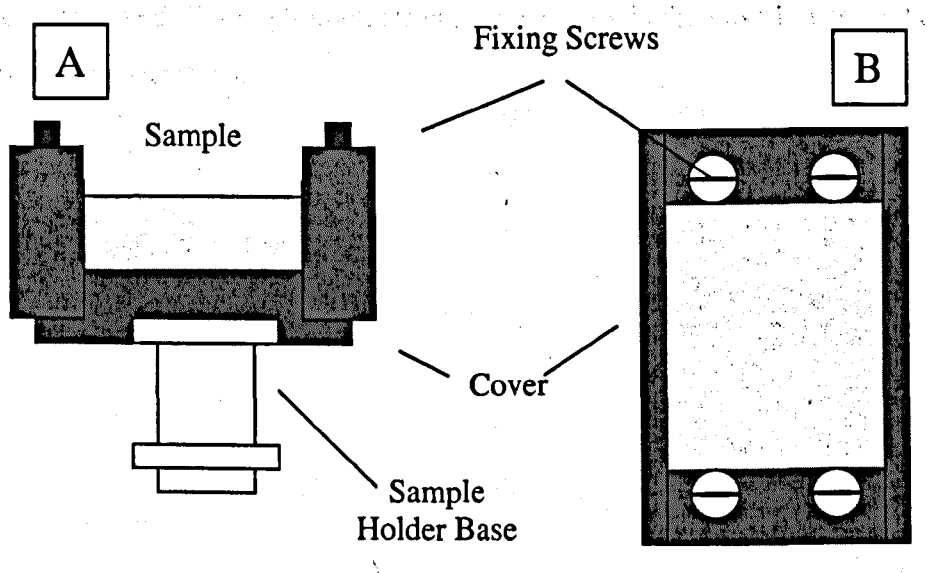

FIGURE 2.4: Scienta sample holder, side view 'A' and plan view 'B'.

2.3 Sample Preparation for Experimentation

The specimens need to be cleaned once fixed in the sample holder (Fig2.4). The pressure in the preparation chamber of the Scienta is increased to atmosphere by introducing nitrogen. The sample and holder are placed into the housing and the chamber pumped down to $1x10^{-8}$ mbar. There is a mechanical scraper attached to the chamber, which consists of a steel rod with a sharp titanium tip (Fig2.2).

The very top surface of the sample is then physically scraped off. This method of sample cleaning is preferred because other surface preparation techniques can produce surfaces with one alloy component dominant. One such technique is argon ion bombardment. This method uses Ar ions that have

been accelerated through a potential difference and are incident on the biased sample. The ions then physically knock off the atoms on the top surface of a specimen i.e. the contaminants. However, the effectiveness of this process can depend on the atomic weight and it is possible that it results in surface enrichment. The scraping is preferred because all atoms on the surface have the same probability of being removed. After cleaning the sample is then transferred to the main chamber.

The 1s levels of O and C are scanned to be sure all contaminants have been removed. X-ray photoelectron spectroscopy is then used to collect data from the specimens.

2.4 References

[1] Scienta 300 Instruction Manual.

CHAPTER 3

Charge Transfer and Disorder Broadening Determined from XPS in Disordered Transition Metal Alloys

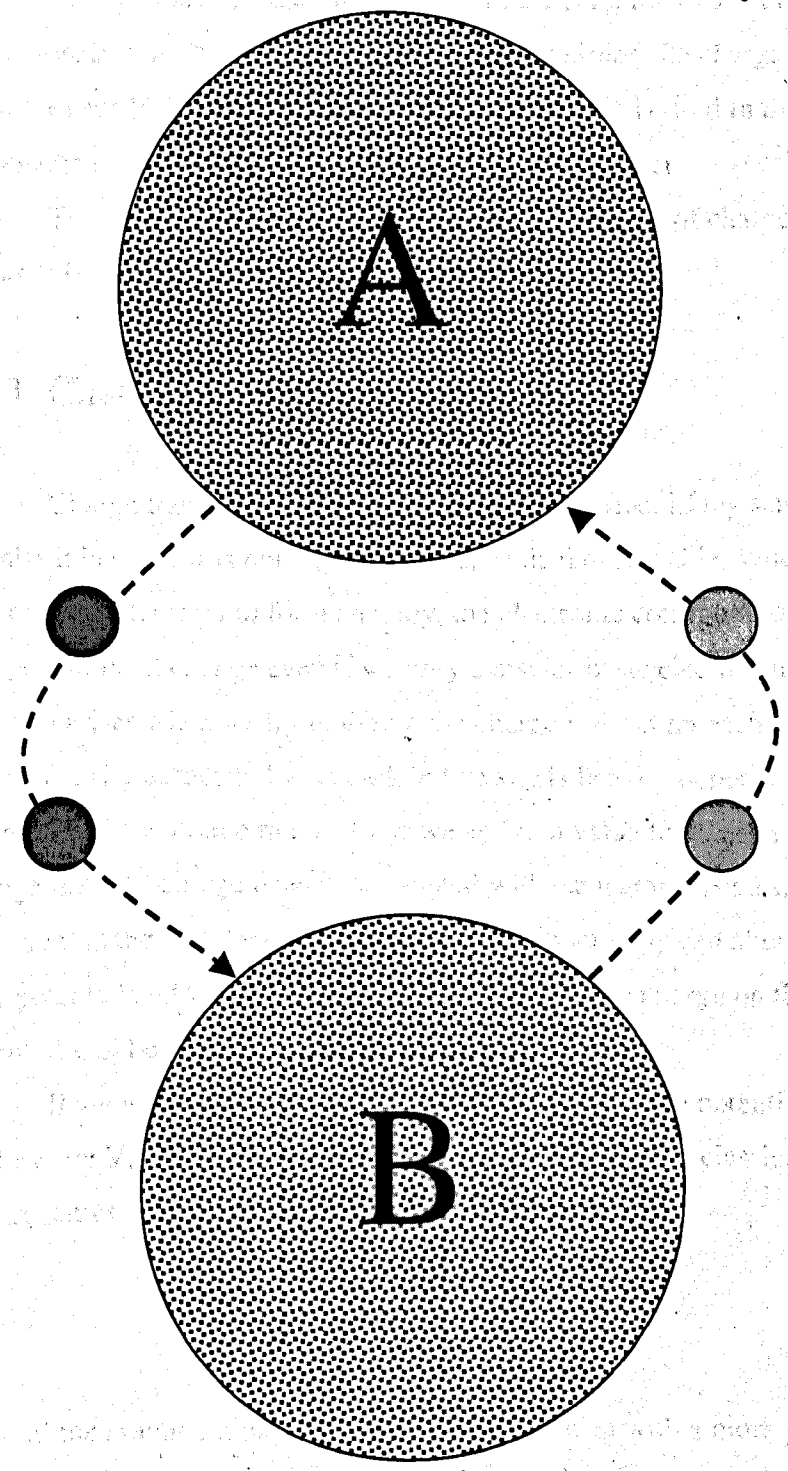

3.1 Introduction

Four different alloy systems were studied in the work reported in this thesis: CuPt, NiPt, AgPd and CuPd. All form face centred cubic (FCC) lattices and all were prepared so that the ordering in the samples was kept to a minimum. In this chapter, the methods for determining the charge transfer and disorder broadening are discussed. This methodology is used in the analysis of the results obtained for the four alloys in the next chapter.

The next section describes the history and theory of charge transfer and disorder broadening.

3.11 Charge Transfer

Charge transfer is a very hard quantity to define. Many scientists will dismiss it because it is not a quantum mechanical observable. When we mix two or more elements to form an alloy, the electronic configuration of each component must change even if we only consider basic electrostatics. The problem arises when we try to define the charge present on each atom. The charge density associated with each lattice site is heavily dependent on the definition of the atomic radius. How we assign a value to this can dramatically change the total charge density associated with each atom species. However, we note that the valence charge of an element in an alloy can alter the atomic core potential and we expect that the effect of valence charge on the core potential will be approximately linear.

If we assume that the atom is a charged sphere, the potential at the core of the atom V, can be related to the valence charge q using classical electrostatics. Therefore the atomic core potential is: -

$$V = \frac{q}{a} \qquad 3.00$$

with 'a' the atomic radius. We can combine this idea with a more general potential model to analyse core level and Auger line shifts with respect to charge transfer.

3.12 Madelung Energies

Madelung [1] studied the electrostatic energy of an array of charges. However, the Madelung energy is often assumed to be zero in first principles treatments of the electrostatic energy of a disordered alloy. Recent work by Zunger and co-workers has shown [2] that it must be included for an accurate description of the electronic and physical structure of random alloys.

A Madelung energy arises from the interaction between the atomic charges in an alloy. A related quantity, the Madelung potential, V^M, will arise from the effect of the charge distribution of other atoms on the core potential of a specific atom. The core potential in an atom can be assumed to be a sum of the intra (valence charge) and extra (Madelung) atomic potentials.

$$V = V^V + V^M \qquad 3.01$$

where V^V is the intra and V^M is the extra atomic potential.

We model a random substitutional alloy by an array of charged spheres each centred on a lattice point *i* of the crystal structure. The nearest neighbour distance being R and hence the atomic radii is R/2, the potential at a lattice point *i* in the alloy relative to the elemental solid will be: -

$$V^i = \frac{14.4}{R}\left\{2Q^i + \sum_{m=1}^{\infty}\frac{1}{\rho_m}\sum_{j\in m}Q^j\right\} \qquad 3.02$$

where the first term is the intra atomic contribution to the core potential arising from the local valence charge Q and the second term is the Madelung potential. ρ_m is the distance between shells. The factor 14.4 is dropped in subsequent equations for brevity. If the charges $Q^{i(j)}$ are in units of *e* and the distances in Å then the potential will be in volts. The first summation in the Madelung term is over concentric spheres with radius $R\rho_m$ centred on site *i*

and the m^{th} is over the Z_m sites in the m^{th} shell. We consider an unspecified crystal lattice populated with A and B atoms and assign an occupation variable S^i to each site such that $S^i = +1$ or -1 depending on whether it is an A or B atom.

We need a model for the charge at each site, so that the distribution of potentials in the random alloy can be found. There are two methods used to model the charge at each site *i*: the Fixed Charge Model (FCM) and the Charge Correlated Model (CCM).

3.13 Fixed Charge Model (FCM)

For a random binary alloy A_xB_{1-x} we could assume that the charge on each lattice site *i* is governed only by the fractional composition of that element at that site c^i. The alloy as a whole must be charge neutral and so: -

$$-Q^A c^A = Q^B c^B \qquad 3.03$$

where $c^A = x$ and $c^B = 1-x$. The FCM implies that the charges on the sites are identical for a particular atomic species and do not change even if the local environment changes. That means that all of the A and separately all of the B atoms have the same charge. Using equation 3.03 with 3.02, the average potential for an A(B) site for a particular number of unlike neighbours N_u is [3]: -

$$\langle V(N_u)\rangle_{A(B)} = \frac{Q^{A(B)}}{R}\left(2 + Z_1 - \frac{N_u}{1-c^{A(B)}}\right) \qquad 3.04$$

where the angled brackets indicate averaging over all possible configurations of the alloy. Z_1 is the number of electrons in the first shell. In metallic alloys, the amount of charge transfer is expected to be of the order of ~0.1eV/atom

[3]. Using the FCM (3.04), would suggest a 1eV shift in potential per unit change in N_u and predicting an XPS core level line width of ~10eV. Clearly, the FCM overestimates variation in potential and we do not expect it to be a good description of the charge distribution in a disordered alloy.

3.14 Charge Correlated Model (CCM)

If we have an A_xB_{1-x} alloy, then it is reasonable to assume that an A(B) atom surrounded by all A(B) atoms will be charge neutral. Conversely, if an A(B) atom is surrounded by all unlike neighbours (B(A)) then we expect that atom to experience the maximum amount of charge transfer. This model has the characteristic that even though the site occupations are random, the site potentials are not. Instead they are correlated with the number of unlike neighbours. This charge correlated model (CCM) was suggested by Magri *et al* [4] and has the form:-

$$Q^i = \lambda \sum_{j \in nn^i} (S^i - S^j) = 2\lambda N_u S^i \qquad 3.05$$

where λ denotes the ionicity and nn^i denotes the set of sites that are nearest neighbours of site *i*. Q^i is the charge transfer for a specific site with N_u unlike neighbours. The contribution to the potential from the intra-atomic term in 3.02 is not dependant on composition and so the potential averaged over all configurations $\langle V(N_u) \rangle$ becomes [3]: -

$$\left\langle V(N_u) \right\rangle_{A(B)} = \frac{4\lambda N_u}{R} S^{A(B)} + \frac{1}{R} \sum_{m=1}^{\infty} \frac{1}{\rho_m} \left\langle Q_m(N_u) \right\rangle_{A(B)} \qquad 3.06$$

where

$$\left\langle Q_m(N_u)\right\rangle_{A(B)} = \left\langle \sum_{j\in m} Q^j \right\rangle \qquad 3.07$$

Now, if we substitute equation 3.05 into 3.07 and neglect all sites with $K_m=0$ (as these sites do not contribute anything to $<V(N_u)>$, we get (3.08) [3]: -

$$\left\langle V(N_u)\right\rangle_{A(B)} = 2\frac{\lambda}{R}S^{A(B)}Z_1(Z_1-1-\Sigma)(1-c^{A(B)}) + N_u 2\frac{\lambda}{R}S^{A(B)}(2-Z_1+\Sigma) \qquad 3.08$$

where Σ is the lattice-dependant constant:

$$\Sigma = \sum_{m=1}^{\infty} \frac{K_m Z_m}{\rho_m Z_1} \qquad 3.09$$

K, Z and ρ are structural parameters. Below in FIG3.1 we can see a diagram explaining the origins of the parameters. ρ_m is the nearest neighbour distance and K_m is the number of sites that are simultaneously nearest neighbours of the central site and a site in the *m*th shell.

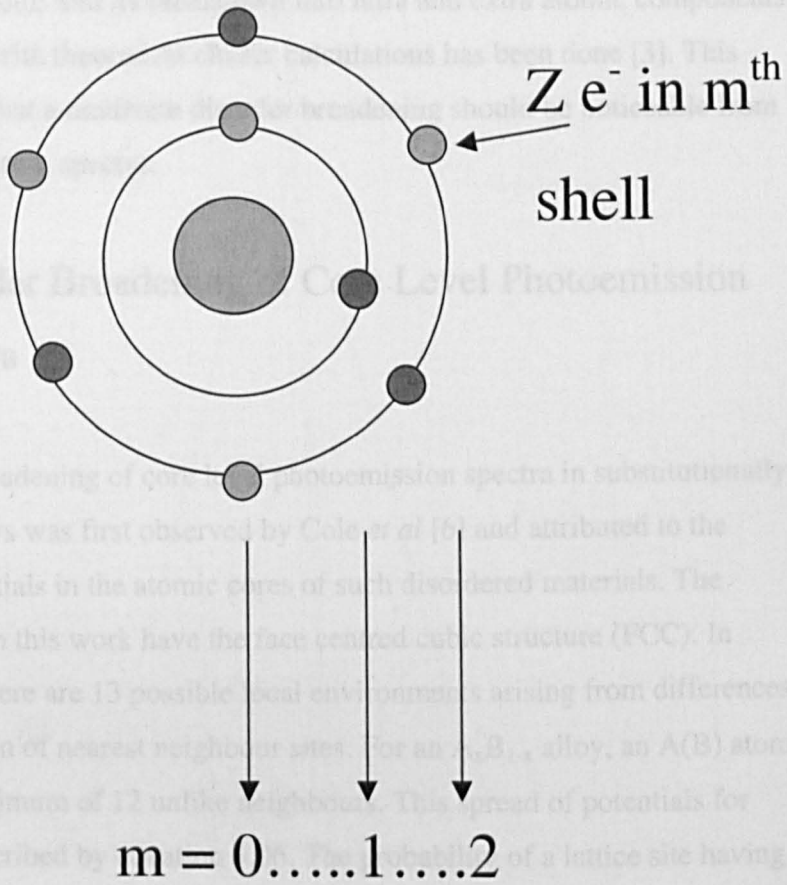

Figure 3.1: Diagram explaining the structural parameters used in the CCM.

Below, Table 3.2 [5] is a table showing the structural parameters for the FCC lattice.

			m					
Lattice	**Parameter**	**1**	**2**	**3**	**4**	**Σ**	**X**	**Y**
FCC	ρ_m	1	1.47	1.74	2	8.22	66.72	-3.56
	Zm	12	6	24	12			
	Km	4	4	2	1			

Table 3.2: Structural parameters for the FCC lattice.

The average potential $\langle V(N_u)\rangle_A$ for A sites surrounded by various numbers of B atoms and its breakdown into intra and extra atomic components then compared with theoretical cluster calculations has been done [3]. This work indicates that a moderate disorder broadening should be noticeable from X-ray photoelectron spectra.

3.2 Disorder Broadening of Core Level Photoemission Spectra

The broadening of core level photoemission spectra in substitutionally disordered alloys was first observed by Cole *et al* [6] and attributed to the spread of potentials in the atomic cores of such disordered materials. The alloys studied in this work have the face centred cubic structure (FCC). In such a lattice there are 13 possible local environments arising from differences in the population of nearest neighbour sites. For an A_xB_{1-x} alloy, an A(B) atom can have a maximum of 12 unlike neighbours. This spread of potentials for each site is described by equation 3.06. The probability of a lattice site having a specific number of unlike neighbours $P(N_u)$, is heavily dependent on the composition of the A_xB_{1-x} alloy ($c^{A(B)}$) [3]:

$$P(N_u)=\frac{Z_1!}{(Z_1-N_u)!N_u!}(c^{A(B)})^{Z_1-N_u}(1-c^{A(B)})^{N_u} \qquad 3.10$$

The probability for each site being populated is plotted against the corresponding local potential in FIG 3.3 [3].

Distribution of potentials obtained for an $A_{0.5}B_{0.5}$ FCC cluster for the indicated value of Nu.

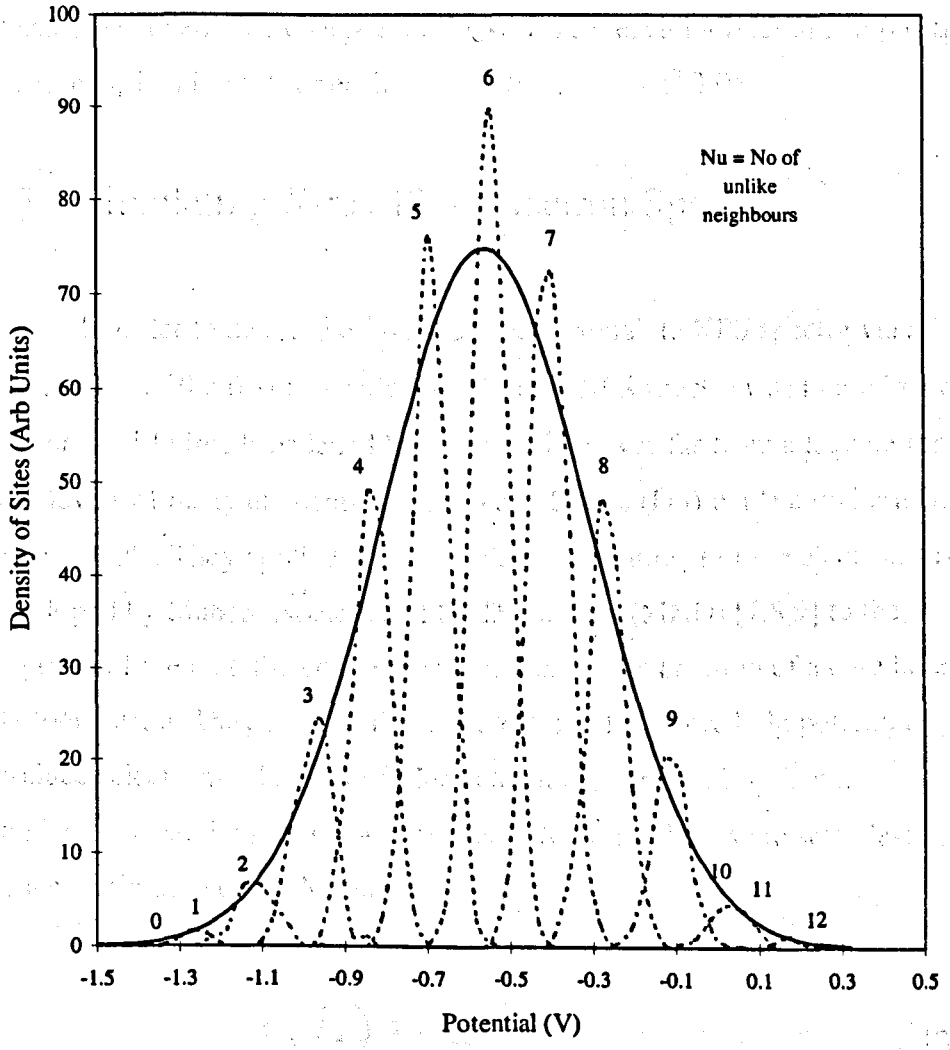

Figure 3.3: Probability Density for each Site with N_u against Potential.

We can see that the potential experienced at each site is separated from the next by a small potential, the value of this potential, or splitting can be found from (3.11): -

$$\langle V(N_u)\rangle = 14.4\,\frac{2\lambda}{R}\,S^i N_u\,(2 - Z_1 - \Sigma)$$

This equation shows that the splitting is proportional to the quantity λ/R. Therefore, we use core level XPS data to extract a value for λ/R and it

has been shown [6] that the total broadening of the photoelectron spectra is given by 4.2 times the individual component splitting. The value of λ is then inserted into equation 3.05 and the charge transfer found for each composition of sample studied. The charge transfer varies for each individual composition because N_u is different for each composition, as in eq^n 3.05.

3.3 Simulating X-ray Photoelectron Spectra

In order to determine λ/R, we need to simulate XPS spectra via a model. One of the first theoretical models for XPS spectra was that of a simple Lorentzian lifetime broadened lineshape, which was far from adequate for the core levels of many elements. Doniach and Sunjic (DS) made a major advance in the 1970's. They applied the many electron treatment of the electron gas developed by Mahan, Noziers and De Dominicas (MND) [7,8,9] to the response of the metallic conduction electrons to the creation of a core hole in photoemission. They showed that the creation of the core hole potential produces electron-hole pairs and leads to an asymmetric lineshape. Doniach and Sunjic [10] showed that core XPS lineshapes are well described by a combination of the Mahan function:-

$$I(E) = E^{\alpha-1} \qquad 3.12$$

where α is the asymmetry index and a Lorentzian representing the finite lifetime of a core hole (assuming that the hole is created instantaneously) giving:-

$$I(E) = \frac{\Gamma(1-\alpha)\cos[\frac{\pi\alpha}{2} + (1-\alpha)\arctan(\frac{E}{\gamma})]}{(E^2+\gamma^2)^{(\frac{1-\alpha}{2})}} \qquad (3.13)$$

for the photoemission lineshape, where Γ is the broadening due to the lifetime of the core hole state, 2γ is the full width half maximum (FWHM) of the core hole and α is the asymmetry index. This function is combined with the previous theory in this chapter for potential and probability calculation. Adopting the CCM we introduce an extra broadening contribution into the fitting procedure arising from the envelope of contributions $f^i(w)$ corresponding to particular local environments:

$$\left\langle f^{i}(w)\right\rangle = \sum_{N_u=0}^{Z_1} P(N_u) L^{\Gamma\alpha}[w, \left\langle v(N_u)\right\rangle \tag{3.14}$$

where $L^{\Gamma\alpha}$ is the DS lineshape with lifetime and asymmetry contributions Γ and α, $P(N_u)$ is the probability of a site having N_u unlike neighbours and $V(N_u)$ is the variation in local core potential with nearest neighbours N_u. W is the gaussian broadening term that arises from the experimental instrument.

3.31 Fitting the Photoemission Lineshapes

To analyse the core level X-ray photoelectron spectra a least squares (LS) fit approach using a parameterised function [11] was used. To judge the quality of a fit the residuals r_i between the theoretical curve and the experimental data were determined. These are calculated from $y_i - y_0(x_i)$, where $(x_i, y_0(x_i))$ is the set of simulated data points and (x_i, y_0) is the set of experimental data points [11,12]. If the LS method fit is a good measure of the actual experimental data then the residuals will represent fluctuations due to statistical noise. Systematic variations in the residuals indicate the inadequacy of the functional form chosen for y_0. For each fit, we quote the index "chi-squared per degree of freedom" χ^2_r which is calculated from: -

$$\chi_r^2 = \frac{1}{n_d - n_p} \sum_{i=1}^{n_d} \frac{(y_i - y_0(x_i))^2}{y_i} \qquad (3.15)$$

where n_p is the number of free parameters, n_d is the number of data points and (x_i,y_i) is the experimental data set.

3.32 Surface Contributions to Core Level XPS Spectra

When fitting XPS core level spectra, it is usual to allow for the surface contribution that accompanies a bulk signal. The characteristics of the surface component is different for each element and it has been shown by Citrin, Wertheim and Baer (CWB) [12] that it must be included in an accurate model for core level spectra. The technique used to identify the surface component from metals used by CWB was angle resolved photoemission. If XPS spectra are taken far from normal emission then the contribution from the surface of the element increases significantly [12]. Fig 3.5 illustrates the surface sensitivity of XPS spectra to take off angle and in Fig 3.4, the take off angle is defined with surface geometry: -

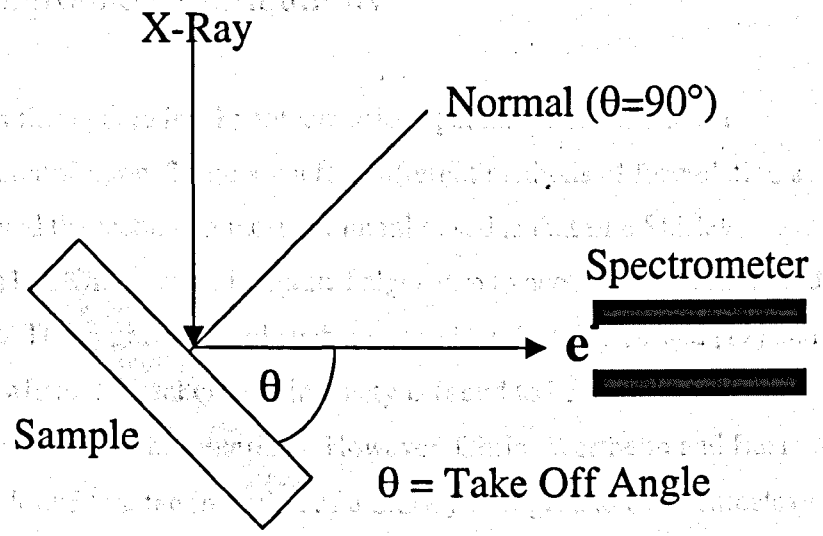

Figure 3.4: XPS Geometry.

Figure 3.5: Surface Peak Intensity versus Take-off Angle (90=Normal Emission).

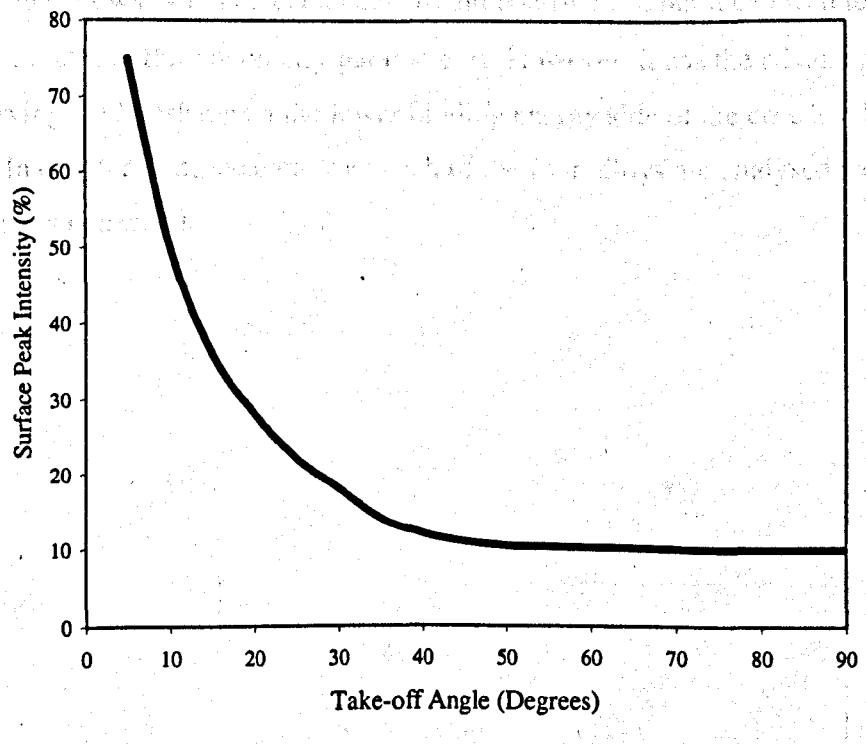

3.33 Background Contributions

When fitting core level photoemission spectra we can include a background contribution. There are a few different methods of formulating a background and the technique most commonly used is that of a Shirley background [13]. This uses an integrated algorithm to account for background contributions. The applicability of such a method has been discussed [11] and in situations where the background intensity is found to be small, including a Shirley background can be beneficial. However, Citrin, Wertheim and Baer (CWB) have found that the inclusion of a Shirley background overestimates the intensity of the core level photoelectron peak on the high kinetic energy side. This effect is accentuated when the asymmetry parameter α is included in the fitting procedure.

Therefore, in our fitting procedure we follow the methodology of CWB and limit the fitting of the core level photoelectron peak to a maximum of 3.5eV biased toward the lower binding energy side of the peak. This technique allows us to neglect a background contribution but it can lead to overestimates in the asymmetry parameter α. However, it has the advantage of preserving the lineshape on the lower binding energy side of the core level peak. In chapter four, the data from each of the four alloys are analysed and the results presented.

3.4 References

[1] E. Madelung. Z. Phys **19**, 524 (1918).

[2] A. Zunger. *"Statics and Dynamics of Alloy Phase Transformations." Ed P.E.A. Turchi and A Gonis (New York: Plenum)* 361-419 (1994)

[3] R.J. Cole and P. Weightman,J. Phys: Condens. Matter **9**, 5609 (1997).

[4] R. Magri, S.H. Wei and A. Zunger,Phys. Rev. B **42** 11388 {1990}.

[5] R.J. Cole and P. Weightman,J. Phys: Condens. Matter **10**, 5679 (1998).

[6] R.J. Cole, N.J. Brooks and P.Weightman,Phys. Rev. Lett. **78**, 3777 (1997).

[7] G.D. Mahan. Phys. Rev. Lett. **163**, 612 (1967).

[8] G.D. Mahan. Solid State Phys. **29**, 75 (1974).

[9] P. Nozieres and C.T. De Dominicis, Phys. Rev. **178**, 1097 (1969).

[10] S. Doniach and M. Sunjic,J. Phys. C **3**, 285 (1970).

[11] G.K. Wertheim and S.B. Dicenzo,J. Elec. Spectrosc. Relat. Phenom.**37**, 57(1985).

[12] P.H. Citrin, G.K. Wertheim and Y. Baer, Phys. Rev. B **27**, 3160 (1983).

[13] D.A. Shirley, Phys. Rev. B **5**, 4709 (1972).

CHAPTER 4

CuPt, NiPt, AgPd and CuPd Alloys.

4.1 Face Centred Cubic (FCC) Alloys

The four alloys studied in this work (CuPt, NiPt, AgPd and CuPd) form substitutionally disordered face centred cubic structures. The lattice constant of the alloys is very dependant on the constituent atom type and alloy composition.

The four main types of crystal structure that can be found when a metallic alloy is fabricated are, body centred cubic (BCC), simple cubic (SC), hexagonal closest packed (HCP) and face centred cubic (FCC). In this work only FCC lattices are studied. The unit cell is the smallest periodic structure that is present in all ordered crystal structures. In an FCC lattice the number of atoms that can fit into a unit cell is two. The co-ordination number for a FCC lattice i.e. the number of nearest neighbours is twelve.

In our work we form substitutionally disordered FCC alloys. This means that the crystal lattice is ordered in the FCC structure but the occupation by atoms of each lattice site in the alloy is determined randomly in accordance with the overall composition. This means that the probability of a lattice site being filled by a specific atom species can be found using a statistical analysis.

Therefore in general, we have long range order in the crystal but no macroscopic ordered phases. The details of alloy fabrication are given in later section of this chapter.

4.2 CuPt Alloys.

CuPt alloys adopt the face centred cubic crystal structure (FCC). The alloy phase diagram for CuPt is shown below in Fig 4.01: -

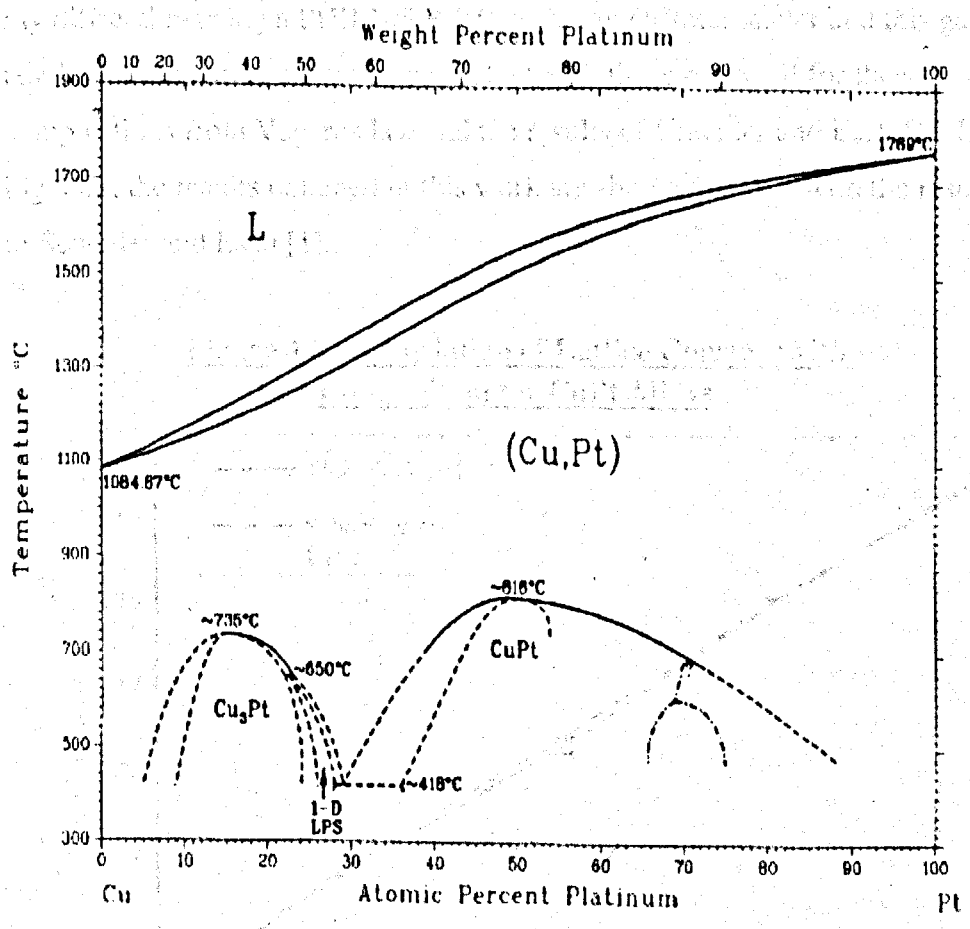

Figure 4.01: - Alloy Phase Diagram for CuPt Alloys.

One can clearly see definite ordered phases for CuPt alloys at two compositions. These are the equatorial composition and the Cu_3Pt composition. This means that there is a tendency for the alloys to form ordered phases at these compositions.

4.21 Fabrication and Analysis of CuPt Alloy Spectra

Specimens of $Cu_{75}Pt_{25}$, $Cu_{50}Pt_{50}$ and $Cu_{25}Pt_{75}$ were made from 99.99999 % purity material by co-melting in an Ar arc furnace as described in chapter 2. The disordered polycrystalline specimens were then analysed by X-ray diffraction using a PHILIPS PW1840 X-ray Diffractometer and this gave results for the lattice constants consistent with those expected for these compositions from Vegards law and the results of Scneider and Esch [1]. In Fig 4.02, the results obtained in this work are shown together with the results of Scneider and Esch [1].

Figure 4.02: - Variation of Lattice Constantwith Composition for CuPt Alloys

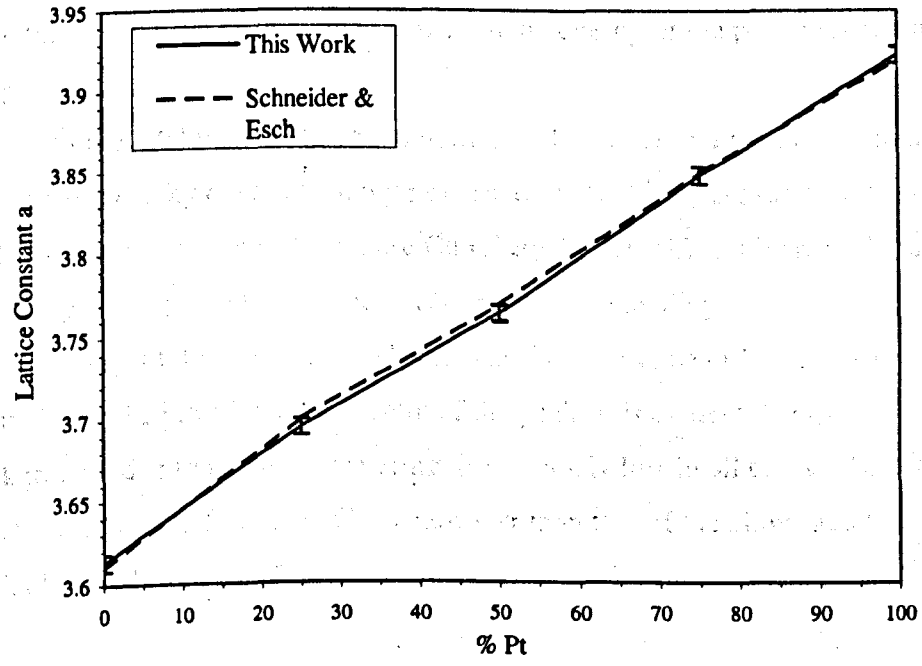

X-ray photoelectron spectroscopy measurements were performed on the alloys and on pure Cu and Pt using the Scienta ESCA 300 spectrometer at the RUSTI facility of the Daresbury laboratory. Prior to the XPS experiments the specimens were cleaned in situ by mechanical scraping at room temperature. The scraping produced clean surfaces as shown by the absence of XPS spectra from the 1s core levels of O and C.

After allowing for photoelectron cross-sections [2] and electron escape depths [3] the surface oxide contribution was found to be significantly less than 2% of a monolayer (Equation 1.7). High resolution XPS spectra of the Cu and Pt core levels were taken at near normal incidence and the energy scales referenced to the measured position of the Fermi energy. An analysis of measurements of the XPS spectrum of the Fermi level showed the spectrometer to have a Gaussian resolution of 0.29 ± 0.02eV at Full Width Half Maximum (FWHM). After allowing for photoelectron cross-sections [2] and electron escape depths [3] the relative intensities of $Cu2p_{3/2}$ and $Pt4f_{7/2}$ photoelectron lines gave compositions for the specimens of $Cu_{76}Pt_{24}$, $Cu_{52}Pt_{48}$ and $Cu_{28}Pt_{72}$ to an accuracy of ± 2% (Equation 1.7).

The experimental $Cu2p_{3/2}$ photoelectron spectra observed from Cu, $Cu_{75}Pt_{25}$, $Cu_{50}Pt_{50}$ and $Cu_{25}Pt_{75}$ are shown in Fig 4.03 & 4.04. The spectra observed from the alloys have been aligned at the kinetic energy of the peak maximum for pure Cu.

In Fig 4.03 the data has been normalised with respect to constant total integrated intensity over the energy range shown. In this figure the narrower width of the line observed from pure Cu results in a significant increase in the peak height compared to the spectra observed from the alloys.

In Fig 4.04 the peaks have been placed on the same ordinate scale by normalising the intensity at the centre of the peak. It is evident that the background, due to inelastic scattering, is extremely low in all cases. The spectrum observed from pure Cu is narrower than that of the alloys and the peak observed from $Cu_{50}Pt_{50}$ is the broadest.

Fig 4.03 Experimental Cu2p data normalised to integrated intensity and aligned in energy.

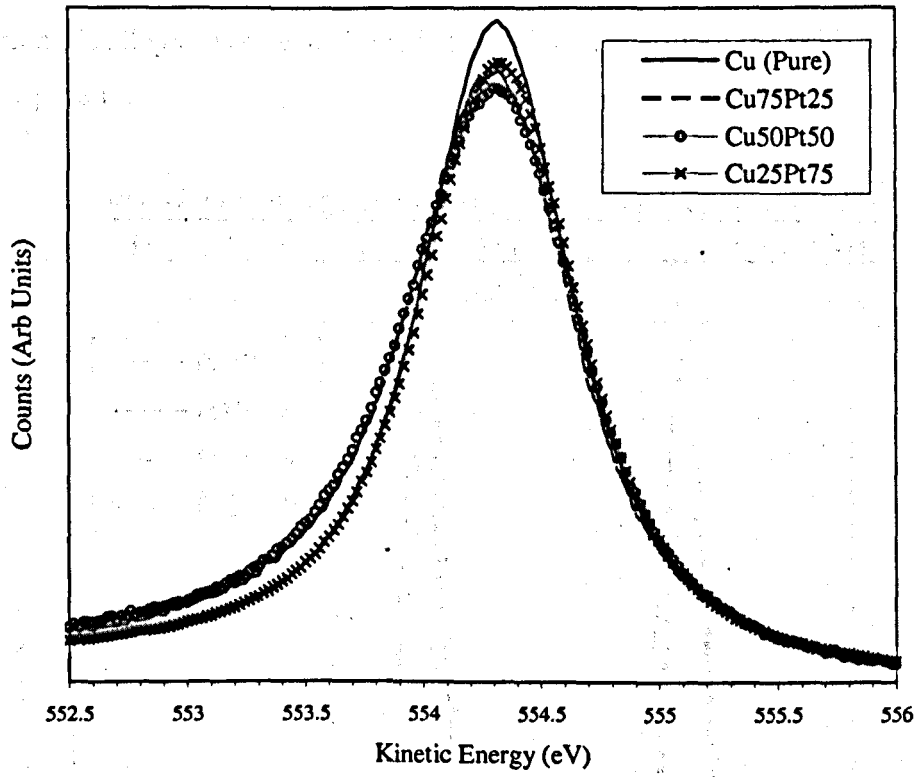

Fig 4.04: Experimental Cu2p data normalized to peak height and aligned in energy

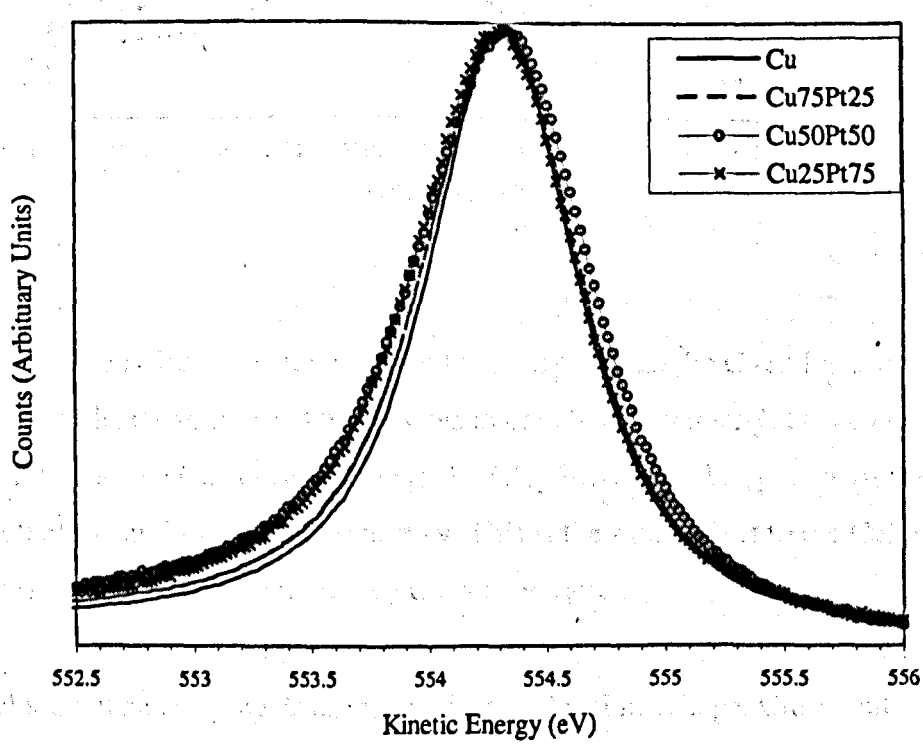

The experimental $Pt4f_{5/2}$ and $Pt4f_{7/2}$ photoelectron spectra observed from Pt, $Cu_{75}Pt_{25}$, $Cu_{50}Pt_{50}$ and $Cu_{25}Pt_{75}$ are shown in Fig 4.05. The spectra observed from the alloys have been aligned at the kinetic energy of the peak maximum for pure Pt.

Figure 4.05: Pt $4f_{5/2}$ & $Pt_{7/2}$ photoelectron lines in CuPt alloys. The peaks have been aligned in energy and normalised wrt peak height.

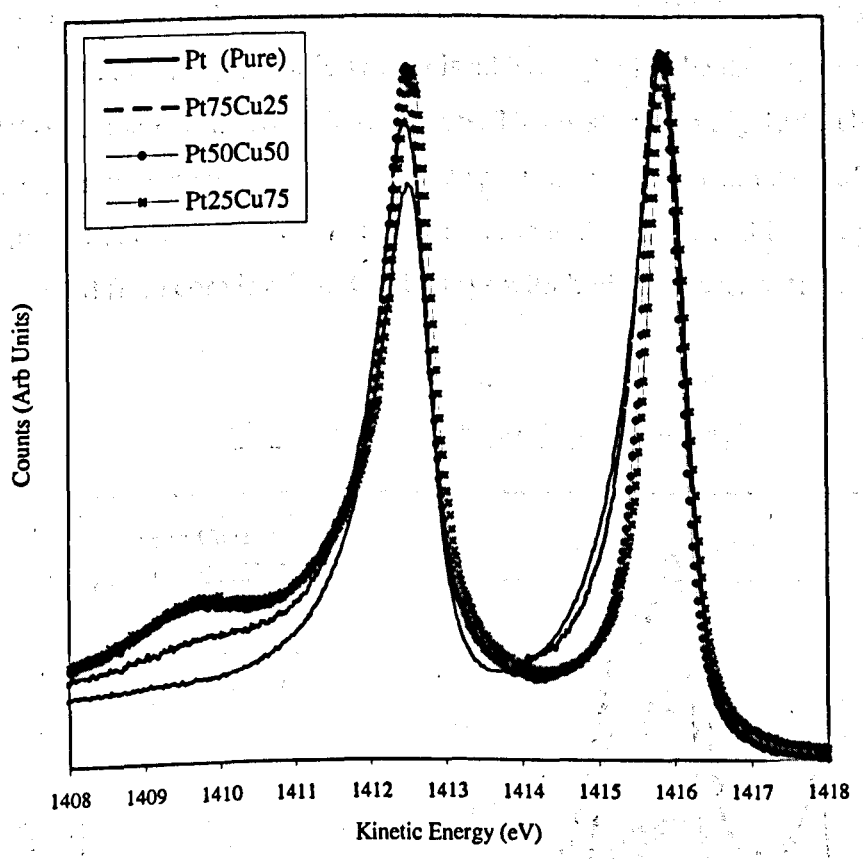

The Pt lines are more difficult to interpret than the Cu2p lines since they are clearly influenced by changes in core line asymmetry. However, it is clear that as the Cu concentration in the alloy increases, the spectra, of the Pt4f photoelectron lines (Fig 4.05) narrow. This is the same effect to the Cu2p (Fig 4.03) that narrows with increased Cu concentration.

We recall in the previous chapter, an asymmetry parameter α must be included in an accurate description of a core level lineshape. Citrin and Wertheim [4] studied the dependence of the asymmetry of a core level

lineshape on the density of states (DOS) at the Fermi level (E_f). They found that the amount of asymmetry present in the core level lineshape is proportional to the DOS at E_f. Therefore, if an elements contribution (in an alloy) to the DOS at E_f is large, then the spectral lineshape obtained from that element will be asymmetric. If the DOS at E_f is low however, the spectral lineshape will be approximately symmetric. However, if the Fermi level enters the d-band of the metal this simple relation no longer holds true and the size of the asymmetry is determined by a wider region of the DOS than that at E_f.

In our data, (Fig 4.05) as Cu is added to the Pt, the density of states (DOS) at the Fermi level (E_f) decreases. This is shown in Fig 4.06. This provides an explanation as to why the spectral lineshape from the CuPt alloys with low concentrations of Pt are symmetrical. Asymmetrical lineshapes are observed from core levels in CuPt alloys with high Pt concentration.

Fig 4.06: Valence bands in CuPt alloys.

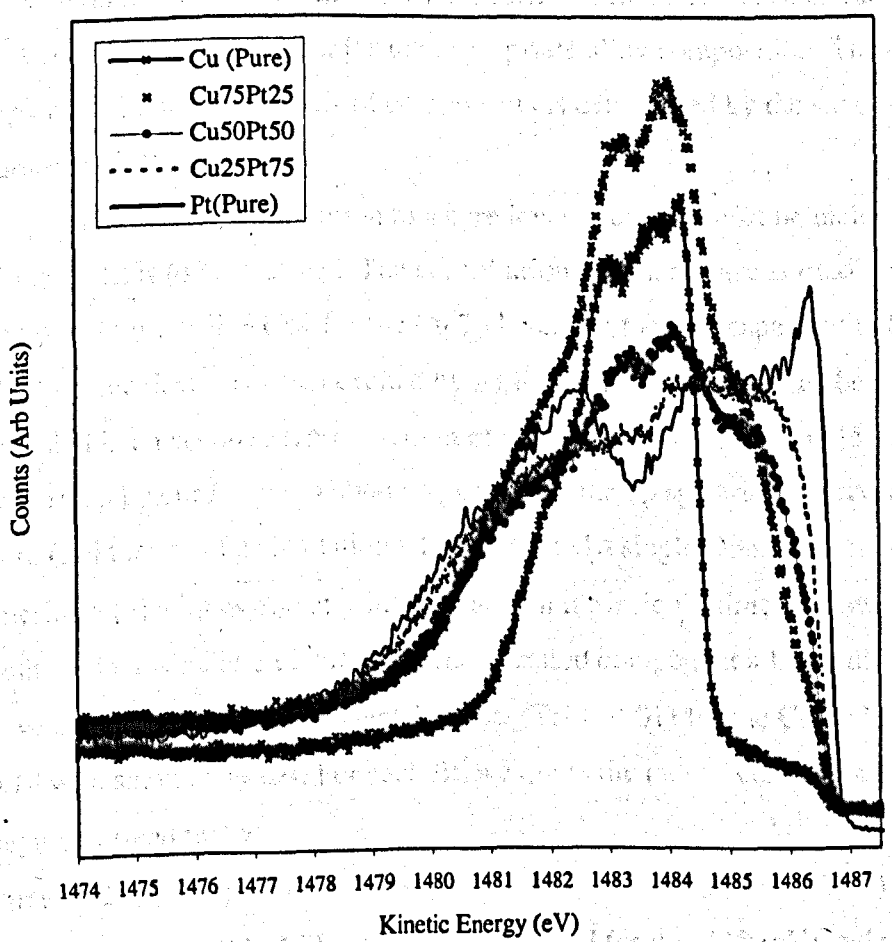

4.22 $Cu2p_{3/2}$ Core Level Analysis

In this work we fit core level spectral lineshapes obtained from substitutionally disordered polycrystalline alloys. The primary aim of the fitting procedures (chapter 3 section 3.2-3.3) is to enable us to determine the magnitude of charge transfer present between one alloy component and another in the four alloy species studied. This is done by determining the λ/R parameter from the fitting procedure.

The core level lineshape is fitted with one bulk and one surface component. The bulk component is split into thirteen other peaks. The number of components that contribute to the bulk peak is a constant (13), but the population density of each component depends on alloy composition (Equation 3.10).

The core level lineshape is fitted with one bulk and one surface component. The bulk component is split into 13 equally spaced peaks with a relative intensity given by the statistical variation in the presence of each particular local environment for the appropriate alloy composition. The separation between each pair of components is determined by the single free parameter λ/R.

The surface contribution to a core level lineshape must be included [5] if a good fit is to be obtained. The contribution from a surface shifted component is small, ~10% for the Cu 2p level due to the escape depth of the Cu 2p photoelectrons when excited by Al Kα radiation, but it must be included in an accurate representation of the photoemission spectra [5] as we confirmed by our failure to obtain a good fit to the 2p spectrum observed for pure Cu in terms of a simulation which assumed a single Doniach-Sunjic (DS) lineshape [6] with asymmetry index α and an intrinsic lifetime Γ. However, with the inclusion of an arbitrary surface shifted component a LS minimisation gave a good fit to the experimental results (Table 4.01) for the Cu 2p line χ^2_r = 0.18 with small residuals. For each fit, we quote the index "chi-squared per degree of freedom" χ^2_r.

Pure $Cu2p_{3/2}$. The fitting parameters obtained for this analysis (FIT 1) are shown below in Table 4.01. The values obtained for the shift (eV) and relative

intensity (in %) of the surface component relative to the main, bulk, line are in good agreement with the results of Citrin, Wertheim and Baer (CWB) [5]. The value obtained for the instrumental Gaussian broadening, W, from fitting the Cu 2p line is in excellent agreement with the result obtained from measuring the Fermi edge. The results of this fit are shown in Fig 4.07 together with the residuals which are small and statistical in origin except in the low energy region below the main peak were a systematic element arises from our neglect of an explicit treatment of the electron energy loss process. The background in our experimental results is low (Fig 4.03, 4.04) and we follow (CWB) and fit the spectrum to over 1.0eV to the higher kinetic energy side of the photoelectron line and make no explicit allowance for the background.

FIT :	FIT 1	FIT 2	FIT 3
Sample :	Cu	$Cu_{50}Pt_{50}$	$Cu_{50}Pt_{50}$
E_b^s	0.27 +/- 0.02	0.21 +/- 0.02	0.21 +/- 0.02
I_s	0.10 +/- 0.06	0.12 +/- 0.06	0.12 +/- 0.06
Γ	0.60 +/- 0.03	0.70 +/- 0.03	0.63 +/- 0.03
W	0.29	0.29	0.40 +/- 0.03
α	0.04 +/- 0.01	0.09 +/- 0.01	0.09 +/- 0.01
$\lambda/R(x10^{-3})$	–	–	–
χ_r^2	0.18	0.81	0.27

FIT :	FIT 4	FIT 5	FIT 6
Sample :	$Cu_{50}Pt_{50}$	$Cu_{75}Pt_{25}$	$Cu_{25}Pt_{75}$
E_b^s	0.21 +/- 0.02	0.23 +/- 0.02	0.21 +/- 0.02
I_s	0.12 +/- 0.06	0.12 +/- 0.06	0.12 +/- 0.06
Γ	0.6	0.6	0.6
W	0.29	0.29	0.29
α	0.09 +/- 0.01	0.05 +/- 0.01	0.08 +/- 0.01
$\lambda/R(x10^{-3})$	1.5 +/- 0.2	1.0 +/- 0.2	1.2 +/- 0.2
χ_r^2	0.25	0.21	0.28

Table 4.01: - Fitting Parameters for Cu2p in CuPt Alloys.

The values shown in Table 4.01 without error bars were held constant during the fitting procedure.

$Cu_{50}Pt_{50}$ Cu2p$3_{/2}$.

The values obtained for I_s, W and E_b^s in the fit to the Cu2p$_{3/2}$ spectrum (Table 4.01) were used as a starting point for an attempt to fit the Cu2p$_{3/2}$ spectrum of $Cu_{50}Pt_{50}$. This fit (FIT 2, Table 4.01) is poorer than that obtained for pure copper even after allowing α to vary and gave $\chi^2_r = 0.8$. It is notable that the parameters representing the surface contribution although allowed to vary freely in the fitting procedure were unable to account for the additional broadening observed in the alloy. Although, the minimisation procedure significantly increased the value of the lifetime parameter Γ, a Lorentzian, this did not reduce the residuals sufficiently suggesting that the additional broadening in this spectrum is not Lorentzian but Gaussian in character. This was confirmed in the next fit, Fit 3 (Table 4.01) were, after allowing the Gaussian parameter, W, to increase to an optimum value of 0.40 the χ^2_r reduced to 0.27. This increased W is greater than the experimental resolution and shows that another Gaussian broadening mechanism is present in the spectrum. We attribute this to "disorder broadening" of the electrostatic potential in the alloy. In Fit 4, the Gaussian parameter W was fixed at the instrumental contribution 0.29 eV and the λ/R parameter, as described previously, [7] allowed to vary. For $Cu_{50}Pt_{50}$ this additional broadening contribution caused the residuals to decrease significantly to $\chi^2_r = 0.25$. The value of λ/R was found to be $1.51 \times 10^{-3} \pm 0.20$eV. This fit is shown in Fig 4.08.

A similar analysis of the lineshape of the Cu 2p spectra observed from $Cu_{75}Pt_{25}$ and $Cu_{25}Pt_{75}$ produced the results shown in Table 4.01 (Fits 5 and 6). In both cases it was possible to obtain a good fit to the experimental results by an increase in the broadening contributions, whilst keeping the instrumental contribution W constant at its known value. The Lorentzian Γ and surface contributions (I_s, E_b^s) were allowed to vary freely within the intrinsic uncertainty. The values of α and λ/R obtained were 0.045 ± 0.005 and $0.95 \times 10^{-3} \pm 0.20$ eV for $Cu_{75}Pt_{25}$ and 0.079 ± 0.005 and $1.18 \times 10^{-3} \pm 0.20$ eV for $Cu_{25}Pt_{75}$ respectively.

Figure 4.07: Experimental (solid line) and simulations (circles) for the $Cu2p_{3/2}$ core line in Cu and the associated residuals as a percentage of peak height.

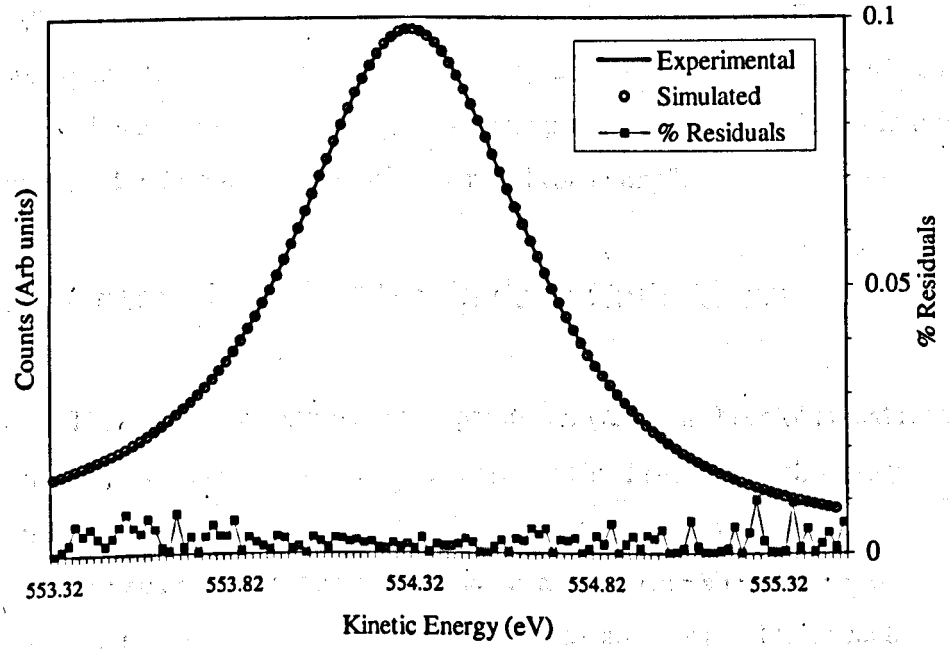

Figure 4.08: Experimental (solid line) and simulations (circles) for the $Cu2p_{3/2}$ core line in $Cu_{50}Pt_{50}$ and the associated residuals as a percentage of peak height.

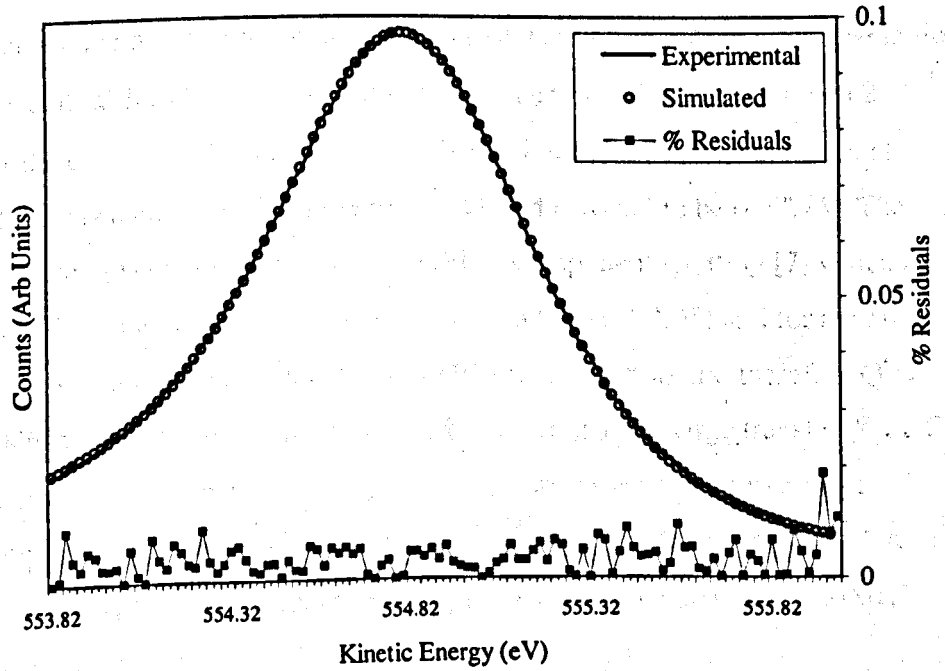

It can be seen that the contribution from disorder broadening was less in these alloys than in the $Cu_{50}Pt_{50}$ composition as expected on the basis of the CCM. However, the model predicts that the value of λ/R for the $Cu_{75}Pt_{25}$ and $Cu_{25}Pt_{75}$ should be the same. The smaller value obtained for $Cu_{75}Pt_{25}$ is probably due to local ordering of the $Cu_{75}Pt_{25}$ alloy that has a distinct ordered phase at this composition (see Fig 4.01). The presence of local ordering in this alloy would reduce the amount of "disorder broadening".

4.23 Charge Transfer Magnitude in CuPt Alloys

The size of the charge transfer parameter (λ/R) has been obtained from the fitting procedure for $Cu_{75}Pt_{25}$, $Cu_{50}Pt_{50}$ and $Cu_{25}Pt_{75}$. The methodology described in chapter 3 can be used to determine the charge transfer, broadening and splitting. The splitting is the amount (in eV) that the component peaks that contribute to the bulk peak are separated from each other. The total broadening is the amount (in eV) that the peak is broadened due to the effect of disorder in the samples.

To calculate the ionicity λ, the inter-atomic distance R (Å) for Cu atoms in CuPt is required. In an FCC lattice, the unit cell length is 'a', the inter-atomic distance for atoms in this crystal structure is then $a/\sqrt{2}$. The lattice constant 'a' for Cu is 3.61 Å and so the inter-atomic distance R is then 2.56 Å. For the equatorial composition, this gives $\lambda = 0.0038e^-$. The component splitting is then found from equation 3.11 and is found to be 0.077eV. The broadening is then 4.2 times the individual component splitting [7] which is 0.32eV. The total charge transfer is then $2*\lambda*N_u$ (eq^n 3.05) and for the 50/50 composition the average number of unlike neighbours is six, therefore $Q^i = 0.0461e^-$. The values for the splitting, broadening and charge transfer (for a Cu atom surrounded by six unlike neighbours) are shown for the two other compositions in Table 4.02. The errors determined for the charge transfer, broadening, splitting and λ are $\pm$ 0.01e$^-$, $\pm$ 0.05eV, $\pm$ 0.02eV and $\pm$ 0.001e$^-$ respectively.

SAMPLE	$Cu_{50}Pt_{50}$	$Cu_{75}Pt_{25}$	$Cu_{25}Pt_{75}$
λ/R	0.0015	0.0010	0.0012
λ	0.0038	0.0026	0.0031
Splitting (eV)	0.0769	0.0513	0.0615
Total Broadening (eV)	0.3230	0.2153	0.2584
ChargeTransfer (Q)	0.0461	0.0307	0.0369

Table 4.02: Charge Transfer (for $N_u = 6$) and Broadening Parameters for CuPt Alloys.

4.24 Conclusions

The broadening is largest for the $Cu_{50}Pt_{50}$ composition as expected on the basis of the correlated charge model (CCM). The CCM predicts that equal broadening should be observed in $Cu_{75}Pt_{25}$ and $Cu_{25}Pt_{75}$. However, we observed the $Cu2p_{3/2}$ line to be significantly narrower in $Cu_{75}Pt_{25}$ a finding we attribute to the presence of local ordering in the $Cu_{75}Pt_{25}$ specimen since the phase diagram shows an ordered phase at this composition [8].

A detailed analysis of the broadening in terms of the CCM yields values of the charge transfer parameter λ/R of $1.5x10^{-3}$ and $1.2x10^{-3}$ for $Cu_{50}Pt_{50}$ and $Cu_{25}Pt_{75}$, which as expected from the CCM, are compatible within the experimental uncertainty of $\pm 0.20x10^{-3}$. The smaller value of this parameter $0.95x10^{-3}$ obtained from the analysis of the results for $Cu_{75}Pt_{25}$ will be an underestimate if, as expected, ordering was present in this specimen.

The charge transfer value quoted above (Table 4.02) is for a Cu atom surrounded by six unlike and six like neighbours in the nearest neighbour shell. The $Cu_{25}Pt_{75}$ and $Cu_{50}Pt_{50}$ values are consistent within the experimental errors, but the $Cu_{75}Pt_{25}$ value is inaccurate. This magnitude of the charge transfer will be affected by the presence of local ordering in the sample.

4.3 Analysis of NiPt Alloys.

The alloy specimens were prepared as described in chapter 3 and examined using X-ray diffraction and XPS. The XRD experiments were used to confirm the composition of the NiPt alloys. Initial elemental compositions corresponded to $Ni_{75}Pt_{25}$, $Ni_{50}Pt_{50}$ and $Ni_{25}Pt_{75}$. Subsequent analysis using XPS and XRD yielded compositions of $Ni_{77}Pt_{23}$, $Ni_{49}Pt_{51}$ and $Ni_{25}Pt_{75}$.The lattice parameter for NiPt versus Pt concentration is shown below in Fig 4.09.

Figure 4.09: Lattice Parameter for NiPt alloys.

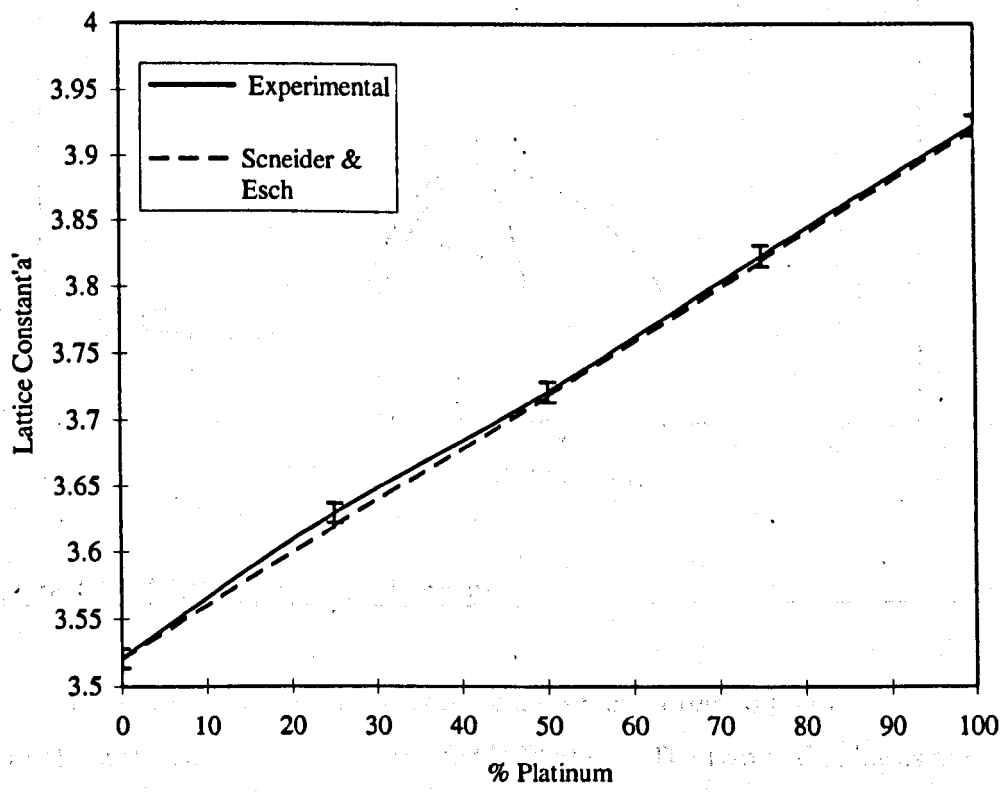

Since Ni lies above Pt in the periodic table we expect that the amount of charge transfer between each constituent element in the alloys will be very low.

NiPt alloys adopt the FCC lattice and the phase diagram is shown below in Fig 4.10 [9].

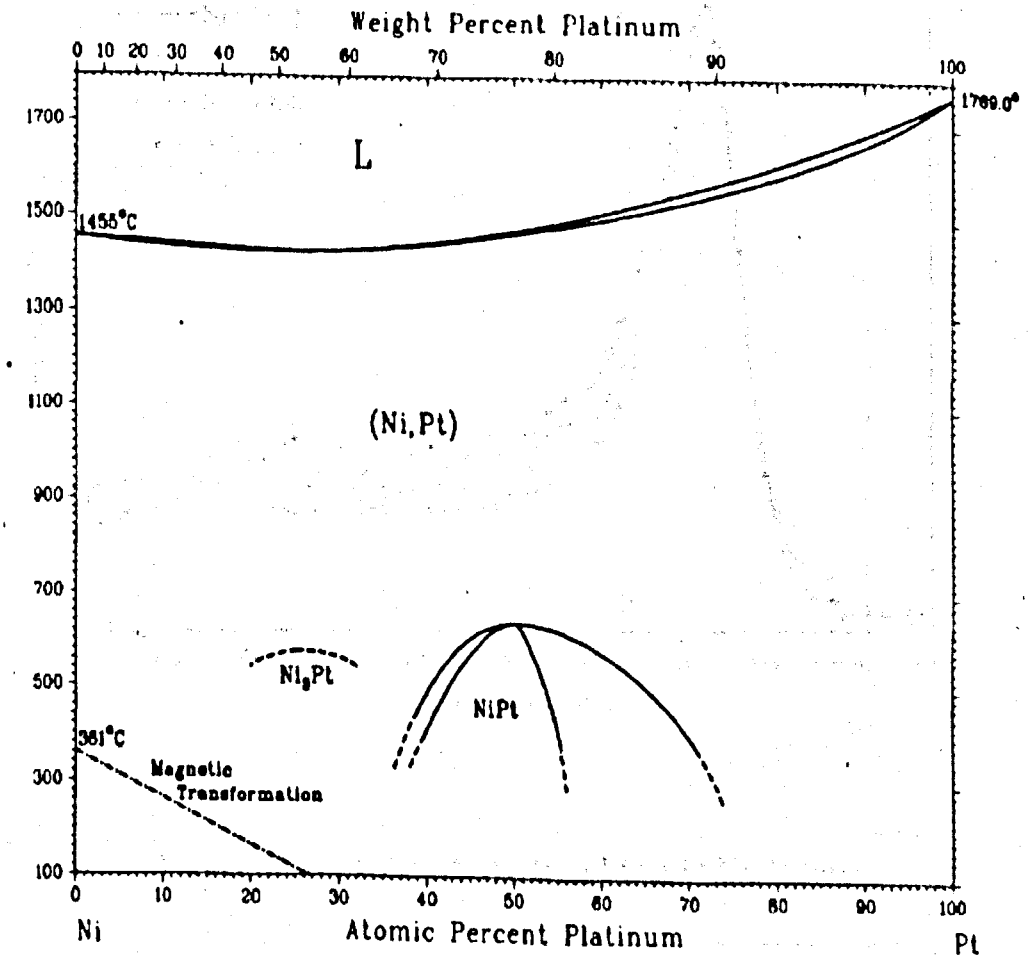

Figure 4.10: NiPt Alloy Phase Diagram.

It can be seen (Fig4.10) that there are several ordered phases throughout the compositional range for NiPt alloys. The two main phases are the NiPt and Ni_3Pt ordered structures that adopt the FCC lattice. Out of the three alloy compositions made for experiment, two are in these regions. Therefore, as a preliminary guess, one would expect the charge transfer and disorder broadening present in these alloys to be significantly less than in the composition where there are no ordered phases. The sample with no ordered phases is $Ni_{25}Pt_{75}$.

The experimental $Ni2p_{3/2}$, $Pt4f_{5/2}$ and $Pt4f_{7/2}$ spectra observed from Ni, $Ni_{75}Pt_{25}$, $Ni_{50}Pt_{50}$, $Ni_{25}Pt_{75}$ and Pt are shown in Fig 4.11 and 4.12.

Figure 4.11 :Ni2p Photoelectron Lines in NiPt alloys.

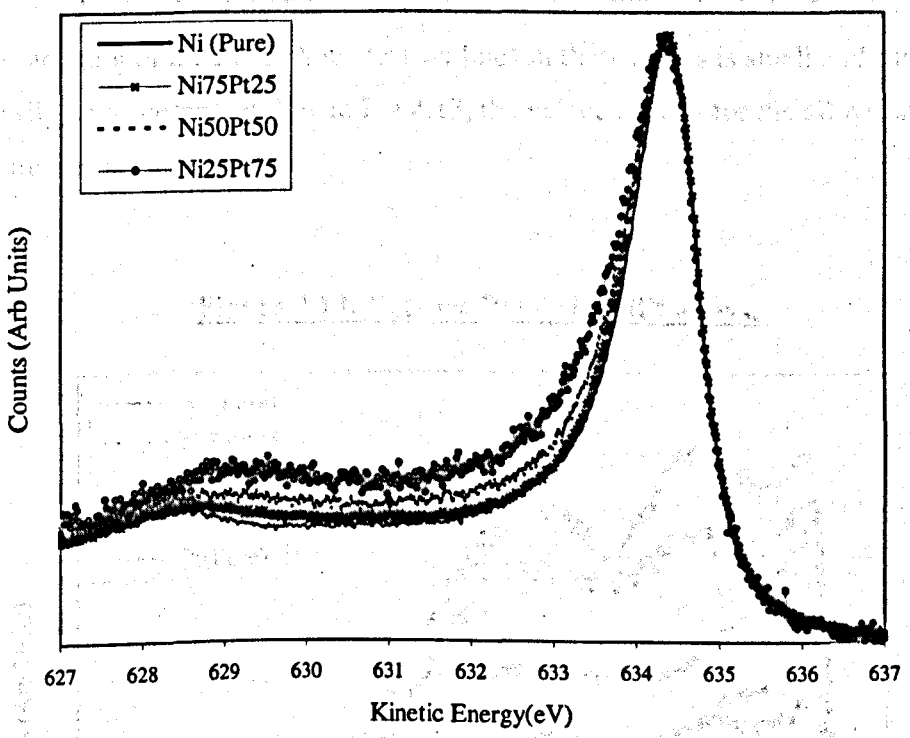

Figure 4.12: Pt4f Photoelectron Lines in Nipt alloys.

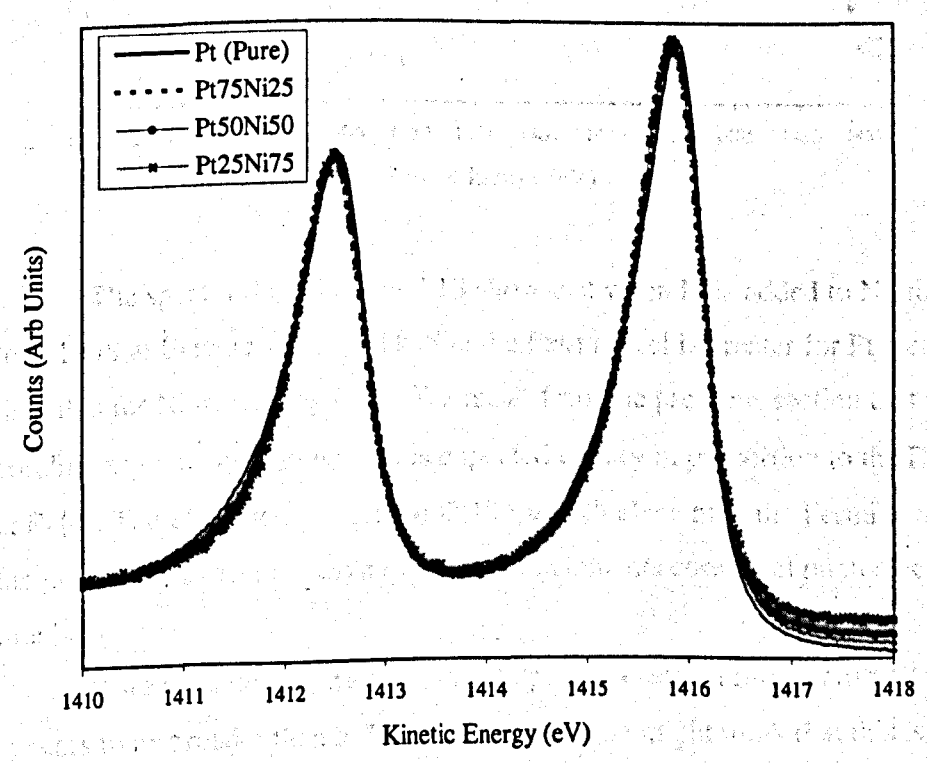

The spectra observed from the alloys have been aligned at the kinetic energy of the peak maximum for pure Ni and Pt respectively.

One can see from the above figures, any compositionally induced broadening of the Pt 4f photoelectron lines in these alloys is small and cannot easily be discerned. Below in Fig 4.13, the valence bands for the alloys and pure elements are shown: -

Figure 4.13: Valence Bands in NiPt alloys.

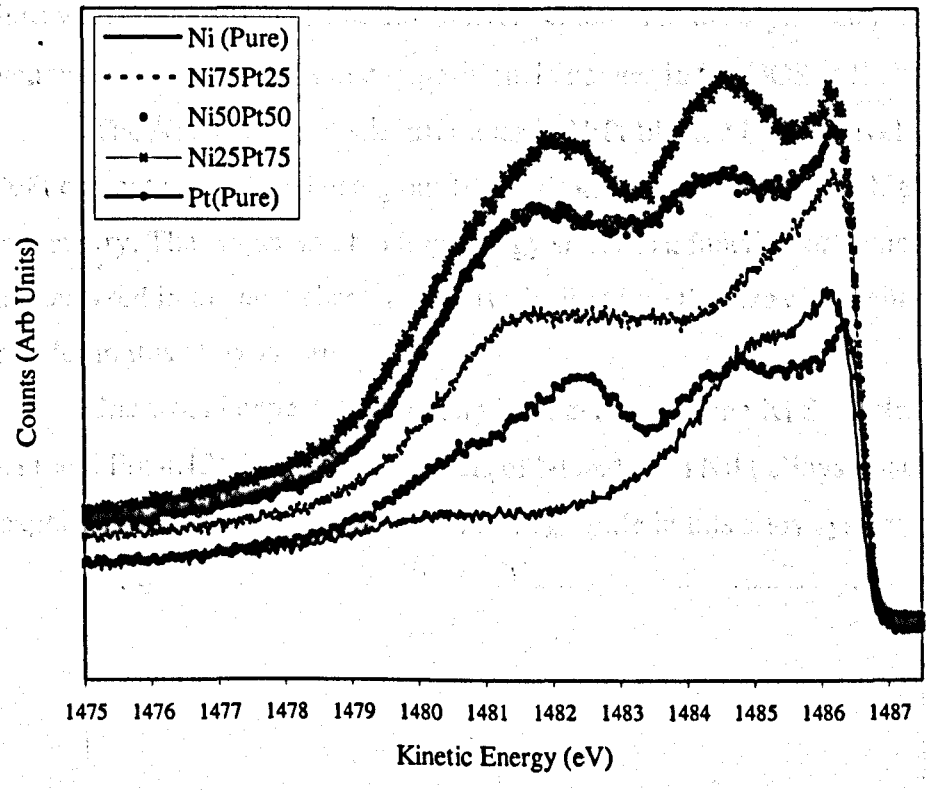

The spectra shown in Fig 4.13 show that when Pt is added to Ni, the total DOS at E_f increases. The DOS at the Fermi level is greater for Pt metal than it is for Ni metal (Fig 4.13). We recall from the previous section that the coreline asymmetry parameter α is expected to vary in proportion to the DOS at E_f [4]. Therefore, the greater the DOS for each element at the Fermi level, the greater we expect the asymmetry of that elements core level photoelectron line [4].

If we consider Figure 4.11, the Ni2p photoelectron line in NiPt alloys appears to be broader than in Ni metal. At first one might think that this is a

similar situation to the Cu2p line in CuPt alloys and that we are observing disorder broadening of the core level XPS spectra due to charge transfer. However, if we consider the DOS at the Fermi level, we see that the total DOS at E_f increases as we alloy with Pt. However, as there is no change in the asymmetry of the Pt4f photoelectron lines with composition this implies that the DOS at E_f for the Pt sites is almost constant.

The total DOS at E_f will be the sum of the separate contributions from the Ni sites and the Pt sites. It follows that if we neglect the effect of charge transfer and disorder broadening that the change in the Ni2p photoelectron lines with composition can be attributed to changes in the asymmetry parameter α that arises from compositional changes in the DOS at E_f.

The Ni and Pt photoelectron lines in NiPt like the Pt core levels in CuPt can not be analysed using our fitting procedure because of the high asymmetry. The Auger and binding energy shifts as a function of composition are analysed in the next chapter and give insight into the size of the charge transfer in this alloy system.

One would expect that from a visual analysis of the XPS spectra (Fig 4.11 and Fig 4.12) from the core levels of Ni and Pt in NiPt alloys, that the magnitude of the charge transfer will be negligible in this alloy system.

4.4 AgPd Alloys.

The $Cu2p_{3/2}$ photoelectron lines in CuPt were analysed earlier in this chapter using the potential model [7,10,11,12] in which the broadening is interpreted in terms of the local variations in the charge transfer. The broadening was found to be less in the $Cu_{75}Pt_{25}$ alloy than in the other alloys probably because of the existence of an ordered phase at this composition. AgPd is an important alloy to be studied in this context because the AgPd phase diagram does not contain ordered phases throughout its compositional range [13]. The phase diagram for AgPd alloys is shown below in Fig 4.14.

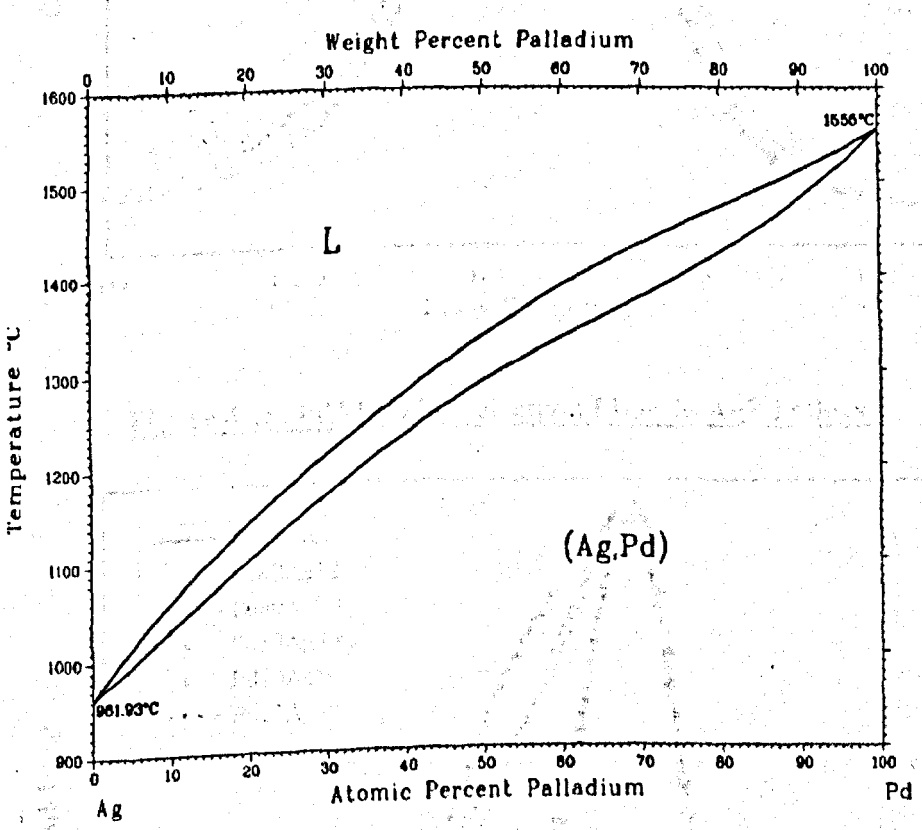

Specimens of $Ag_{12}Pd_{88}$, $Ag_{20}Pd_{80}$, $Ag_{50}Pd_{50}$, $Ag_{80}Pd_{20}$, and $Ag_{88}Pd_{12}$ were made from 99.99999% purity material by co-melting in an Ar arc furnace as described in chapter 2. XPS measurements were made using the Scienta instrument. The experimental data for the Ag3d and Pd3d core lines are shown in Fig 4.15 and 4.16 (only the $3d_{5/2}$ photoelectron line is shown for each sample but equivalent results were obtained for the $3d_{3/2}$ photoelectron lines).

Figure 4.15: Experimental $Ag3d_{5/2}$ in AgPd Alloys.

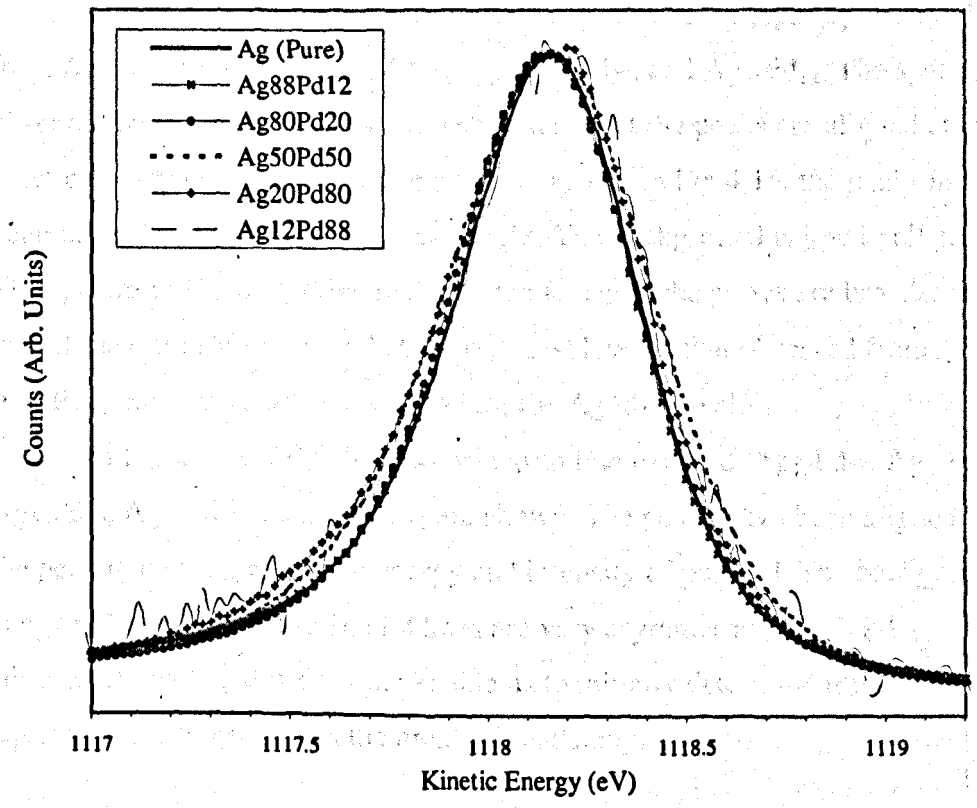

Figure 4.16: $Pd3d_{5/2}$ Photoelectron Lines in AgPd alloys.

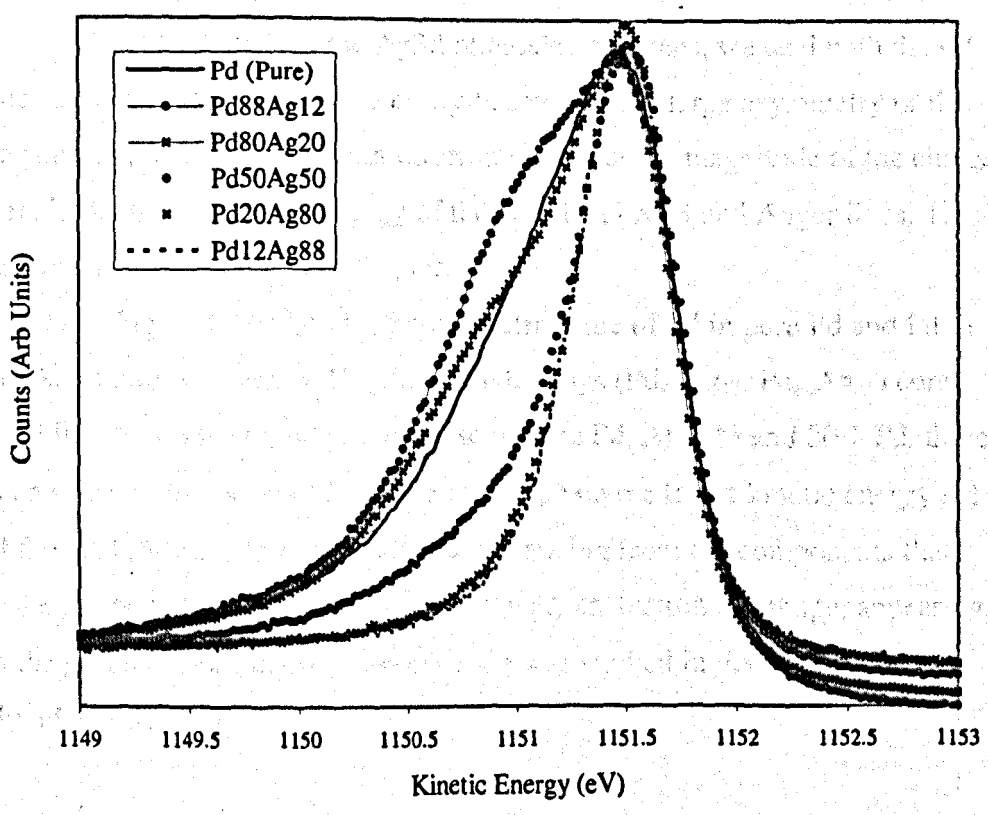

In Figure 4.15 and 4.16, the data has been aligned in energy and normalised with respect to peak height.

Figure 4.15 shows the photoelectron spectra of the $Ag3d_{5/2}$ observed from Ag, $Ag_{12}Pd_{88}$, $Ag_{20}Pd_{80}$, $Ag_{50}Pd_{50}$, $Ag_{80}Pd_{20}$, and $Ag_{88}Pd_{12}$. The spectra observed from the alloys have been shifted so that the peaks are aligned at the kinetic energy of the peak maximum for pure Ag. In Fig 4.15, the peaks have been normalised to a common peak height. The background is low in all cases. The spectra of Fig 4.15 show that the core levels of the alloys are broader than that of the pure element and that the broadest level is that observed from $Ag_{50}Pd_{50}$. Similar results were found for the $Ag3d_{3/2}$ level.

In Fig 4.16 the $Pd3d_{5/2}$ photoelectron line from Pd, $Ag_{12}Pd_{88}$, $Ag_{20}Pd_{80}$, $Ag_{50}Pd_{50}$, $Ag_{80}Pd_{20}$, and $Ag_{88}Pd_{12}$ are shown. The peaks have been aligned at the peak maximum in kinetic energy and intensity of pure Pd. The background is again, low in all cases. The Pd lines are very asymmetric at high Pd concentrations and this does not enable us to initially determine if the equatorial composition has the greater broadening.

4.41 Bulk Components Contribution to XPS Lineshape

Before we analyse the Ag3d photoelectron lines, we deal with the Pd lines as these cannot be treated easily because of the large asymmetry of the lineshape and we can only gain information about the magnitude of the charge transfer from the shifts in energy of the core level XPS and Auger lines. This analysis is given in the next chapter.

In Fig 4.16, the $Pd3d_{5/2}$ photoelectron line of Pd in pure Pd and Pd in the AgPd alloys is shown. For the Pd rich alloys ($Pd_{88}Ag_{12}$, $Pd_{80}Ag_{20}$) core level lineshapes are broader than those of pure Pd. At 88% and 80% Pd, there is an indication of a shoulder in the lineshape on the lower kinetic energy side of the peak. We interpret this shoulder as arising from the components that make up the bulk peak contribution to the photoelectron lineshape, appearing in the spectra. The $Pd_{88}Ag_{12}$ composition was studied in detail to try and elucidate this effect.

The population density of each of the thirteen sites in a disordered FCC lattice is given by statistics (equation 3.10). Several plots of the population density for each bulk component for various alloy compositions are shown in Fig 4.17a,b,c,d.

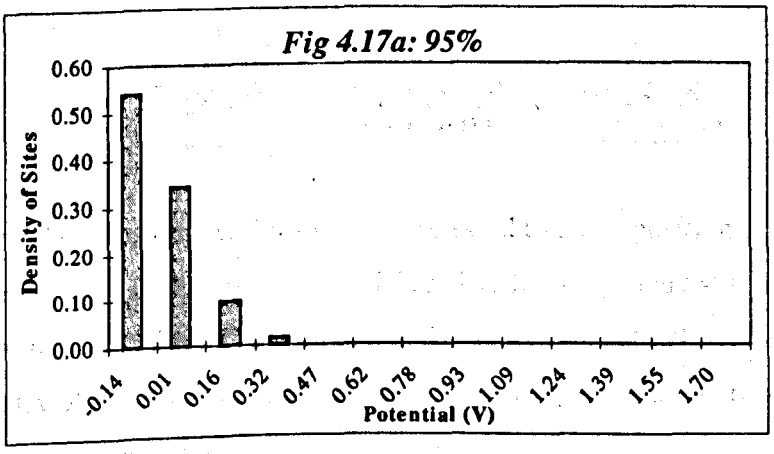

In Fig 4.17a, corresponding to the 95% composition, it can be seen that the probability of occurrence of 9 sites is so small that there contribution to the total XPS lineshape can be ignored. The observed lineshape would thus be dominated by contributions from three sites.

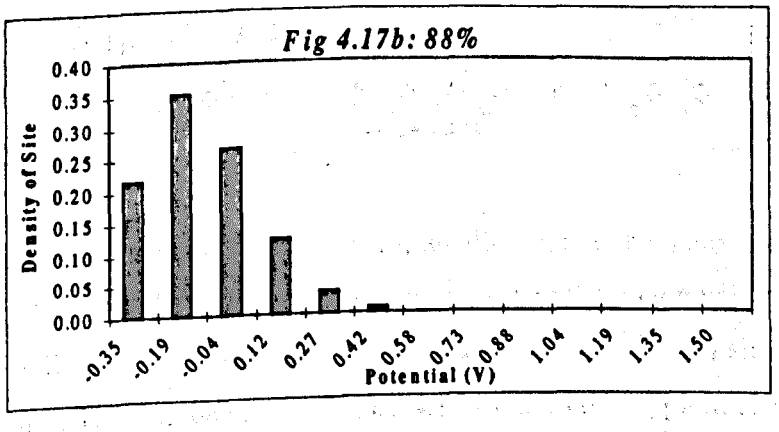

In Figure 4.17b, the 88% composition has four components with appreciable populations and one can see that the lineshape obtained at such a composition would be asymmetric and this could explain the shoulder seen in the Pd3d spectra for the $Pd_{88}Ag_{12}$ composition in Figure 4.16.

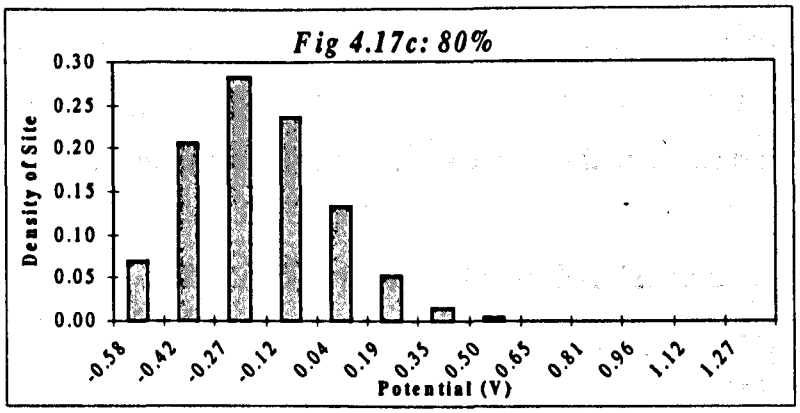

The populations of the various sites correspond to a composition of the major element of 80% is shown in Figure 4.17c. The lineshape may still have some visible structure in the XPS data due to the under lying structure, but the symmetry of the component population increases quickly as we reach the equatorial composition.

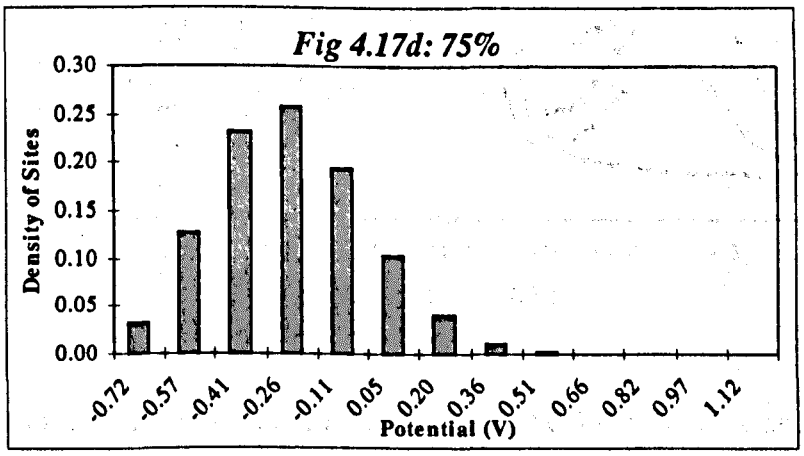

In Figure 4.17d the site populations for an alloy where the major element has a composition of 75% is shown. Any deformation in the core level lineshape due to bulk component population is gone as the distribution of sites is almost symmetric. This can be seen in Figure 4.16 for the $Pd3d_{5/2}$ photoelectron line in $Pd_{50}Ag_{50}$ where the shape of the peak is almost symmetric.

The site population density is not the only factor that governs the symmetry of a core level lineshape. In the section on NiPt alloys we noted that the asymmetry of a lineshape is proportional to the DOS at E_f [4]. Therefore, if the DOS at E_f fluctuates for either the Ag or Pd component in AgPd alloys this will also contribute to the core level lineshape.

AgPd is unusual, not only the fact that there are no ordered phases throughout the compositional range [13] but also because the DOS for the Ag and Pd components in AgPd alloys do not mix very well [14]. This is shown (Fig 4.18), with the Ag DOS to the left and the Pd DOS to the right near E_f.

Figure 4.18: Valence Band in AgPd alloys.

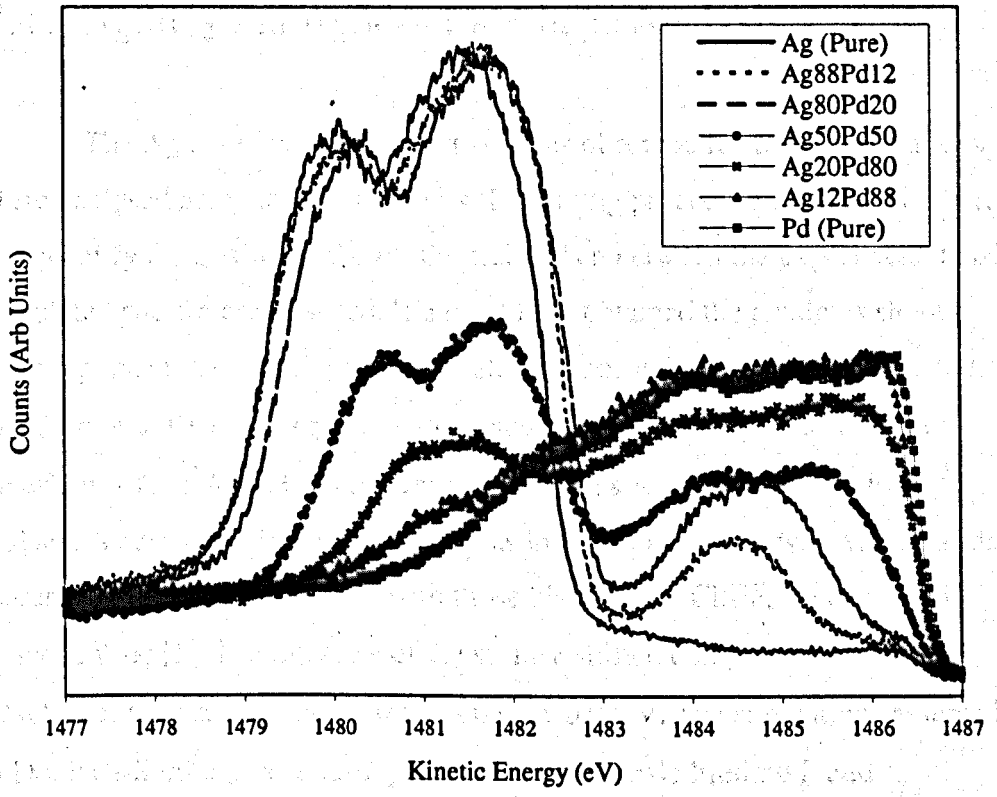

One can see by inspection of Figure 4.18 that the d-bands of Ag and Pd in AgPd alloys do not mix very well. The Ag d-band in pure Ag lies approximately 4eV from the Fermi level and from this point to E_f the valence band is s-p in character. The Pd d-band is at the Fermi level in pure Pd and so the density of states is high for Pd at E_f. The asymmetry of a core level is proportional to the DOS for that elemental species at E_f [4]. We thus expect that the Pd3d lines in pure Pd, $Pd_{88}Ag_{12}$ and $Pd_{80}Ag_{20}$ should have a highly asymmetric lineshapes. Figure 4.16 confirms this. The Pd3d lines become approximately symmetric at the 50:50 composition. This effect can be attributed to two factors; the bulk components become asymmetrically populated (Fig 4.17b) and the decrease in the Pd DOS at E_f.

The Ag3d photoelectron lines remain symmetric throughout the compositional range. This is due to the low Ag DOS at E_f because the Ag d-band never approaches the Fermi level. Only the s-p band in Ag and its alloys is close to the Fermi level [14] and so the lineshape remains symmetric (Fig 4.15).

4.42 $Ag3d_{3/2}$ and $Ag3d_{5/2}$ Lineshape Analysis

The Ag core-level photoelectron lines observed from the AgPd alloys were analysed using the least squares (LS) fitting procedure described earlier. To quantify the quality of the fit, the residuals r_i between the experimental and simulated spectra are reported. If a good fit is obtained the residuals should only represent the variations due to statistical noise. The index, 'chi-squared per degree of freedom' (χ^2_r) is also quoted. The fits to the photoemission lineshape of the Ag3d lines are very good, with small residuals and low χ^2_r values. A surface shifted component was included in the fits with values of the parameters in good agreement with those obtained by Citrin, Wertheim and Baer (CWB) [5]. The intensity of the surface shifted component found by CWB was 0.14 ± 0.03 with a shift of 0.08 ± 0.03eV. The simulations assumed a Doniach-Sunjic (DS) lineshape [6] with an intrinsic lifetime Γ and asymmetry index α. The Gaussian broadening, W, obtained from fitting the Ag3d lines is identical to that obtained from measuring the Fermi edge. The pure Ag3d photoelectron lines were fitted with a single DS lineshape [6] and a surface peak with characteristics given by the work of CWB [5]. The Ag3d lines from the AgPd alloys were fitted with 13 DS bulk component peaks and a surface peak. The charge transfer parameter λ/R was included for these fits.

The measured spectrum for the Fermi level was fitted with a step function to obtain the Gaussian resolution of the spectrometer. This was found to be 0.30 ± 0.02eV at Full Width Half Maximum (FWHM).

In FITS 1-12, Table 4.03 the results of the $Ag3d_{3/2}$ and $Ag3d_{5/2}$ line analysis in AgPd alloys is shown, the parameters without errors were held constant.

Fits of the $Ag3d_{3/2}$ Line in AgPd Alloys			
FIT :	FIT 1	FIT 2	FIT 3
Sample :	Ag	$Ag_{12}Pd_{88}$	$Ag_{20}Pd_{80}$
E_b^s	0.07	0.07	0.07
I_s	0.12	0.12	0.12
Γ	0.27	0.27	0.27
W	0.30	0.30	0.30
α	0.08 +/- 0.01	0.10 +/- 0.01	0.10 +/- 0.01
$\lambda/R(x10^{-3})$	_	1.7 +/- 0.2	1.7 +/- 0.2
χ_r^2	0.86	0.1	0.81
FIT :	FIT 4	FIT 5	FIT 6
Sample :	$Ag_{50}Pd_{50}$	$Ag_{80}Pd_{20}$	$Ag_{88}Pd_{12}$
E_b^s	0.07	0.07	0.07
I_s	0.12	0.12	0.12
Γ	0.27	0.27	0.27
W	0.30	0.30	0.30
α	0.07 +/- 0.01	0.05 +/- 0.01	0.07+/- 0.01
$\lambda/R(x10^{-3})$	1.8 +/- 0.2	1.7 +/- 0.2	1.7 +/- 0.2
χ_r^2	0.75	0.81	0.1

Fits of the $Ag3d_{5/2}$ Line in AgPd Alloys			
FIT :	FIT 7	FIT 8	FIT 9
Sample :	Ag	$Ag_{12}Pd_{88}$	$Ag_{20}Pd_{80}$
E_b^s	0.07	0.07	0.07
I_s	0.12	0.12	0.12
Γ	0.27	0.27	0.27
W	0.30	0.30	0.30
α	0.08 +/- 0.01	0.10 +/- 0.01	0.10 +/- 0.01
$\lambda/R(x10^{-3})$	_	1.7 +/- 0.2	1.7 +/- 0.2
χ_r^2	0.92	0.1	0.81
FIT :	FIT 10	FIT 11	FIT 12
Sample :	$Ag_{50}Pd_{50}$	$Ag_{80}Pd_{20}$	$Ag_{88}Pd_{12}$
E_b^s	0.07	0.07	0.07
I_s	0.12	0.12	0.12
Γ	0.27	0.27	0.27
W	0.30	0.30	0.30
α	0.07 +/- 0.01	0.05 +/- 0.01	0.07 +/- 0.01
$\lambda/R(x10^{-3})$	1.8 +/- 0.2	1.7 +/- 0.2	1.7 +/- 0.2
χ_r^2	0.79	1.24	0.1

Table 4.03: Fitting Parameters for Ag3d lines in AgPd Alloys.

The compositions of the samples were found to be $Ag_{11}Pd_{89}$, $Ag_{21}Pd_{79}$, $Ag_{52}Pd_{48}$, $Ag_{20}Pd_{80}$ and $Ag_{10}Pd_{90}$ to an accuracy of ±2%, after measuring the $Ag3d_{5/2}$ and $Pd3d_{5/2}$ intensities and correcting for photoelectron cross-sections [2] and escape depths [3] (Equation 1.7).

Ag3d (Pure Ag).

In FIT1, the parameters required to fit the Ag3d core lines observed from pure Ag are shown. The values obtained by CWB [5] for E_s^b, I_s, α, Γ are used and the spectrum is fitted in terms of two free parameters, the intensity and asymmetry. In Figure 4.19, FIT7 is shown graphically for the $Ag3d_{5/2}$ line, where it can be seen that the residuals (shown as a percentage of peak height) are negligibly small and are a representation of statistical noise. A good fit was obtained with $\chi_r^2 = 0.86$. The Gaussian broadening parameter W was unconstrained and a value of 0.30eV was found in good agreement with that found from fitting the Fermi edge. The parameter α was varied but is almost negligible because of the fact that Ag has a very small density of states at the Fermi edge (E_f)(Fig 4.18).

Ag3d (AgPd Alloys).

The Ag3d lines in AgPd alloys were fitted with 13 bulk components and one surface component as described earlier and the charge transfer parameter (λ/R) included. This yielded values of $\lambda/R=1.7\times10^{-3}$ eV for $Ag_{12}Pd_{88}$ ($\chi_r^2 = 0.10$) and $Ag_{88}Pd_{12}$ ($\chi_r^2 = 0.10$).

The Ag3d core level lineshapes from $Ag_{20}Pd_{80}$ and $Ag_{80}Pd_{20}$ were fitted and equal values of $\lambda/R=1.7\times10^{-3}$ eV, with χ_r^2 of 0.81 were obtained. The equatorial composition had the greatest broadening and a slightly greater value of $\lambda/R=1.8\times10^{-3}$ eV ($\chi_r^2 = 0.75$), as predicted by the charge correlated model. This fit is shown in Figure 4.20.

Figure 4.19: Experimental and Simulated spectra for the Ag3d5/2 line for pure Ag and the associated residuals as a percentage of peak height.

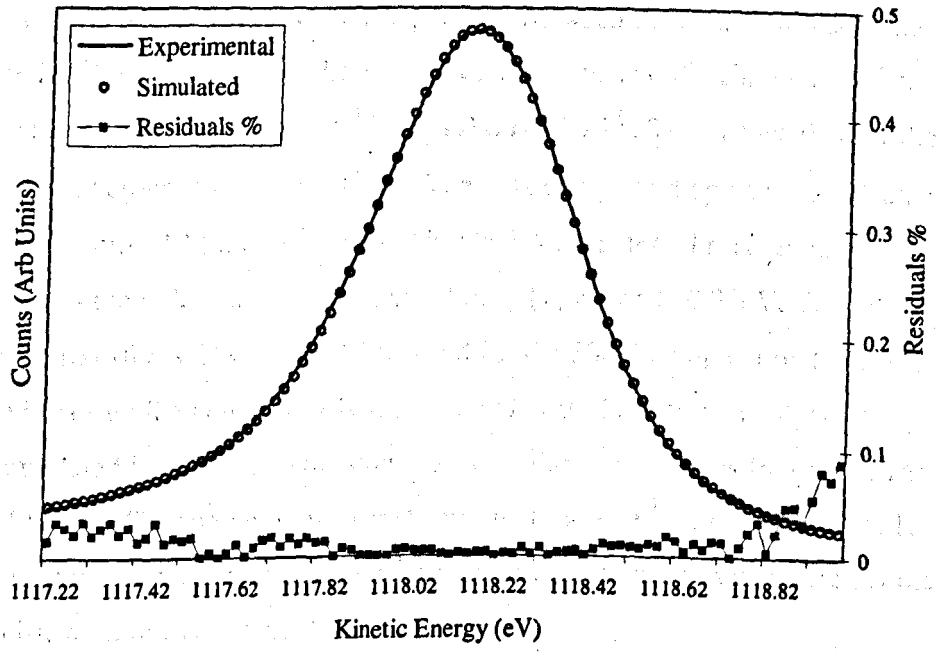

Figure 4.20: Experimental and Simulated spectra for the Ag3d5/2 line in Ag50Pd50 with the associated residuals as a percentage of peak height.

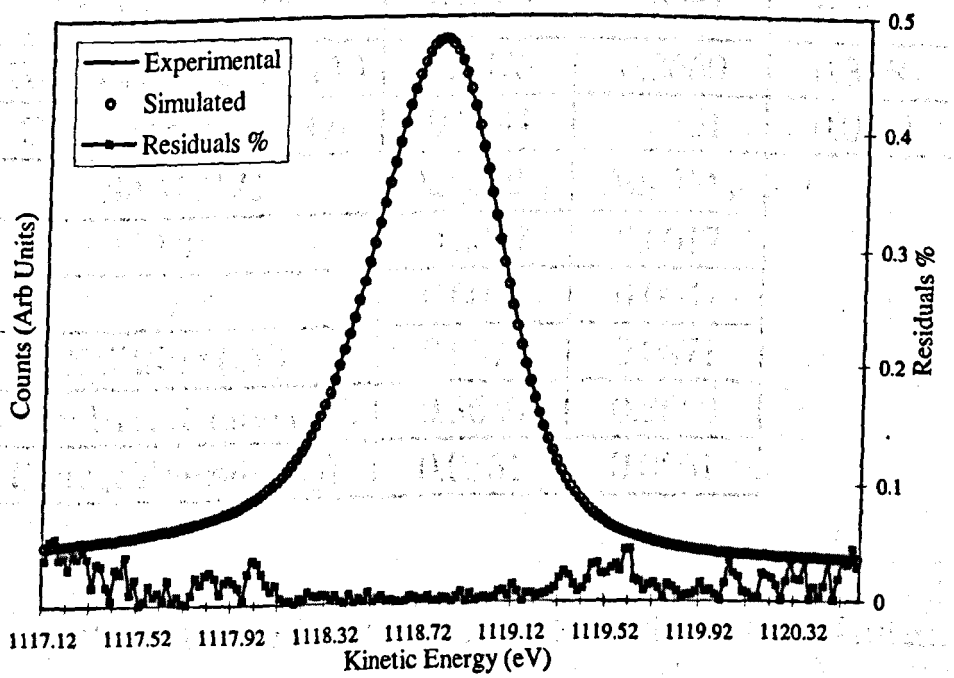

4.43 Magnitude of Charge Transfer in AgPd Alloys.

The charge transfer parameter λ/R has been determined from our fitting procedure. This gives the separation between the contributions to the core level lineshapes from the 13 bulk components and the charge transfer. The inter-atomic distance R (Å) for AgPd is ~2.75Å. This means that for the equatorial composition $\lambda = 0.005e^-$. The bulk component splitting is calculated from equation 3.11 and is found to be 0.092eV. The total broadening is then 4.2 times the individual component splitting [7] which is 0.39eV. The total charge transfer is $2*\lambda*N_u$ (eq^n 3.05) and for the 50/50 composition the average number of unlike neighbours is six giving $Q^i = 0.059e^-$. If the analysis is extrapolated for the four other compositions, the results are as follows in Table 4.04 below. The charge transfer is determined for a nearest neighbour shell with six unlike neighbours, hence the composition of alloy is different but the specific atomic environment is not

SAMPLE	$Ag_{50}Pd_{50}$	$Ag_{88}Pd_{12}$	$Ag_{80}Pd_{20}$
λ/R	0.0018	0.0017	0.0017
λ	0.0050	0.0047	0.0047
Splitting (eV)	0.0923	0.0871	0.0871
Total Broadening (eV)	0.3876	0.3660	0.3660
ChargeTransfer (Q)	0.0594	0.0561	0.0561
SAMPLE	$Ag_{20}Pd_{80}$	$Ag_{12}Pd_{88}$	
λ/R	0.0017	0.0017	
λ	0.0047	0.0047	
Splitting (eV)	0.0871	0.0871	
Total Broadening (eV)	0.3660	0.3660	
ChargeTransfer (Q)	0.0561	0.0561	

Table 4.04: Magnitude of Charge Transfer for Ag3d lines in AgPd Alloys.

The errors determined for the charge transfer, broadening, splitting and λ are $\pm$ 0.01e$^-$, $\pm$ 0.05eV, $\pm$ 0.02eV and $\pm$ 0.001e$^-$ respectively.

4.44 Conclusions

One can see that the values for the broadening and charge transfer are greater for AgPd alloys (Table 4.04) than those of CuPt alloys (Table 4.02). If we consider the broadening of the component peaks that make up the bulk contribution to the core level lineshape, in AgPd alloys, the broadening is ~0.4eV throughout the compositional range (Table 4.04) compared with CuPt alloys that at most have a broadening of ~0.3eV (Table 4.02). One reason for this is the fact that AgPd alloys have no ordered phases throughout the compositional range [13]. There will be no tendency for local order to occur in specimens of this alloy system and so all site environments are present. However, in CuPt alloys, there are ordered phases at certain compositions, which will mean that only specific site environments will be present in specimens of this species.

In table 4.04, the charge transfer for a Ag atom with six unlike (Pd) neighbours in varying alloy compositions is quoted. We can see that in all sample compositions, the amount of charge transfer from Ag to a Pd atom for this environment is the same in magnitude. This was not the case for CuPt alloys, where the charge transfer in all alloy compositions, for a Cu atom surrounded by six Pt atoms differed. We inferred that this was due to the tendency for local ordering to occur at the $Cu_{75}Pt_{25}$ composition.

The charge transfer in AgPd alloys is approximately 25% larger than that in CuPt alloys.

4.5 CuPd Alloys.

CuPd alloys adopt the face centred cubic structure (FCC). There are several ordered phases in particular regions of the compositional range. The phase diagram for CuPd alloys [15] is shown below in Fig 4.21: -

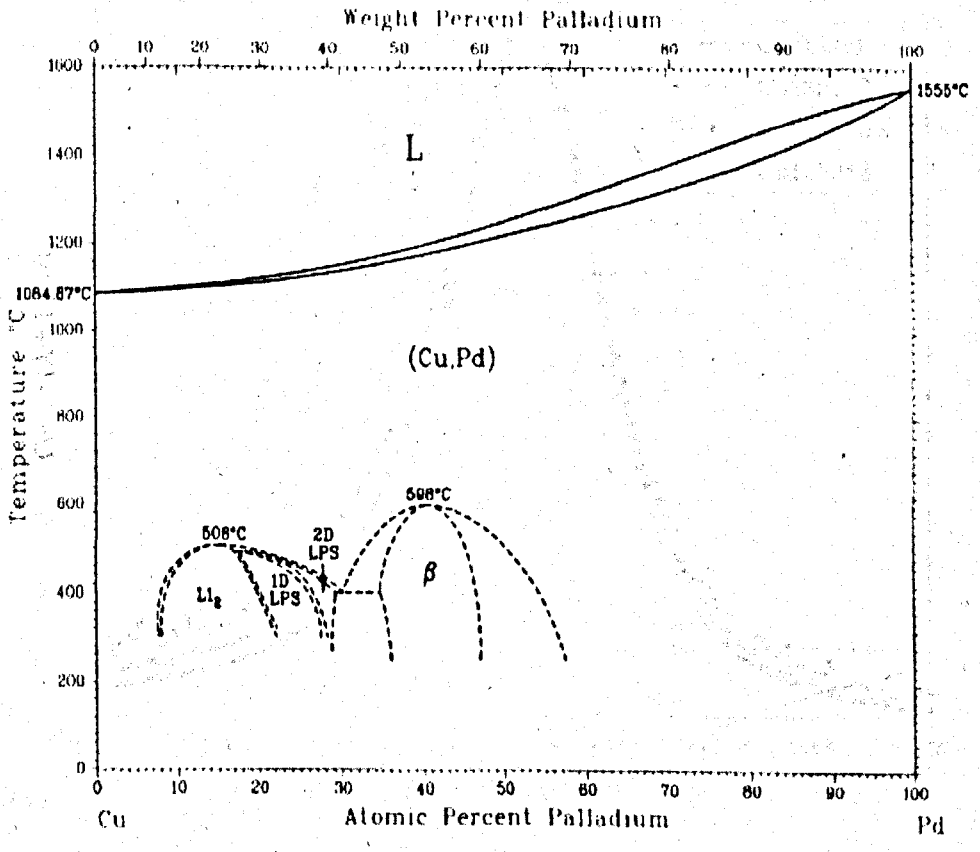

Figure 4.21: Alloy Phase Diagram for CuPd.

We can see (Fig 4.21) that from mid to high copper concentration in CuPd alloys, there are ordered phases. The alloys studied in this work are $Cu_{88}Pd_{12}$, $Cu_{50}Pd_{50}$ and $Cu_{12}Pd_{88}$, the corresponding pure elements were also studied. From the analysis of the CuPt alloy system earlier in this chapter, it is reasonable to expect that the Cu2p spectra from $Cu_{88}Pd_{12}$ and $Cu_{50}Pd_{50}$ samples will be broadened less than expected because of the ordered phases which may lead to local order at these compositions.

XPS measurements were taken on the Scienta instrument at Daresbury Laboratory, Warrington, UK. From the XPS spectra, the compositions of the

alloys were determined using the methodology explained in chapter 1 (Equation 1.7) and found to be: - $Cu_{90}Pd_{10}$, $Cu_{52}Pd_{48}$ and $Cu_{10}Pd_{90}$ to an accuracy of ± 2%.

Figure 4.22:$Cu2p_{3/2}$ Photoelectron lines in CuPd alloys.

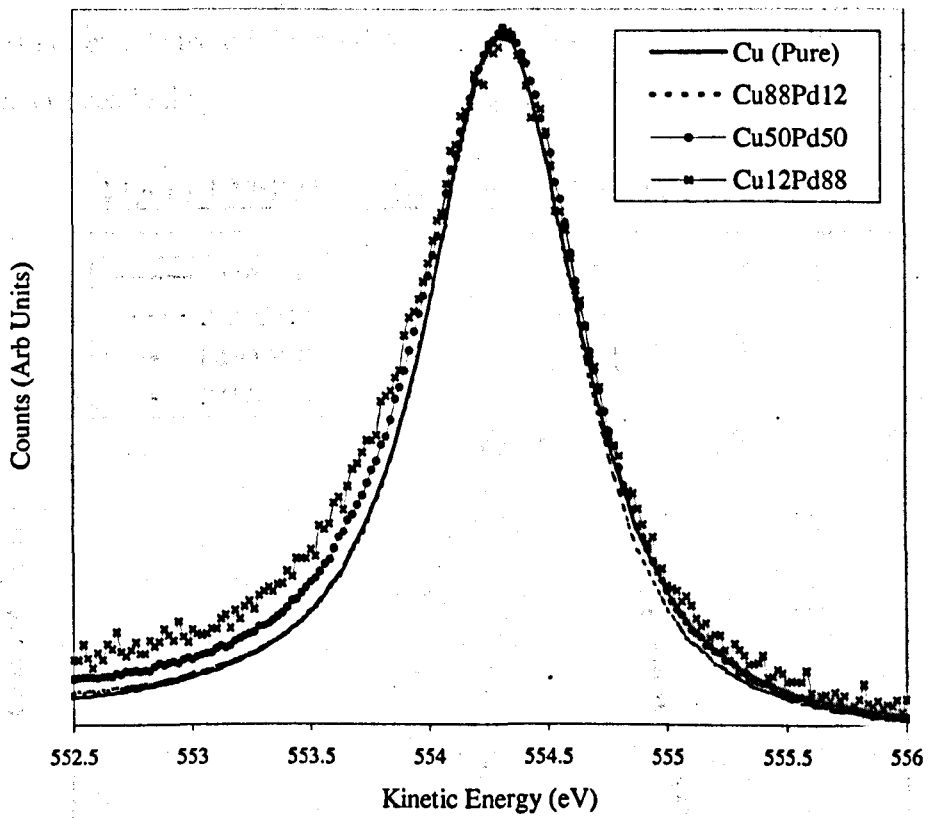

Figure 4.22 shows the photoelectron spectra of the $Cu2p_{3/2}$ observed from Cu, $Cu_{12}Pd_{88}$, $Cu_{50}Pd_{50}$ and $Cu_{88}Pd_{12}$. The spectra observed from the alloys have been shifted so that the peaks are aligned at the kinetic energy of the peak maximum for pure Cu. In Fig 4.22, the peaks have been normalised to a common peak height. The background is low in all cases. The spectra of Fig 4.22 show that the core levels of the alloys are broader than that of the pure element and that the broadest level is that observed from $Cu_{12}Pd_{88}$.

This is not what the charge correlated model (CCM) suggests [16] but the ordered phases at the other two compositions which will mean that there is a tendency for local ordering to occur at these compositions. This will reduce the broadening observed from the core level spectra. The effect of local

ordering at compositions where there is ordered phases was also seen in CuPt alloys, where the broadening was reduced in the $Cu_{75}Pt_{25}$ sample (Table 4.02). In Fig 4.23 the $Pd3d_{5/2}$ photoelectron line from Pd, $Cu_{12}Pd_{88}$, $Cu_{50}Pd_{50}$, and $Cu_{88}Pd_{12}$ are shown. The peaks have been aligned at the peak maximum in kinetic energy and intensity of pure Pd. The background is again, low in all cases. The Pd lines are very asymmetric at high Pd concentrations and this does not enable us to initially determine if the equatorial composition has the greater broadening.

Figure 4.23:$Pd3d_{5/2}$ photoelectron lines in CuPd alloys.

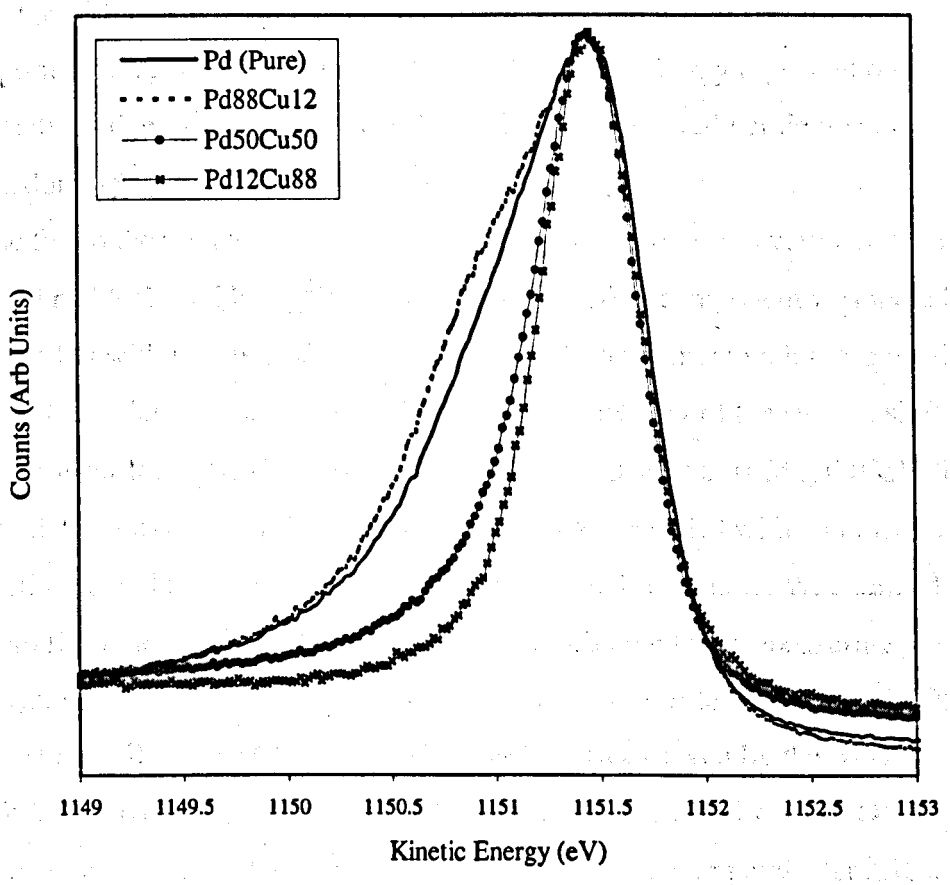

The highly asymmetric lineshapes obtained from the CuPd alloys with a high concentration Pd cannot be analysed using our fitting procedure described in chapter 3. We restrict the analysis to the Cu2p spectra of the alloys. The results are presented in the next section.

4.51 $Cu2p_{3/2}$ Lineshape Analysis

XPS measurements were taken on the Scienta instrument at the Daresbury Laboratory. After allowing for photoelectron cross-sections [2] and electron escape depths [3] the relative intensities of $Cu2p_{3/2}$ and $Pd3d_{5/2}$ photoelectron lines gave compositions of the alloys to be $Cu_{90}Pd_{10}$, $Cu_{52}Pd_{48}$ and $Cu_{10}Pd_{90}$ to an accuracy of ± 2%.

The core-level photoelectron lines were analysed using the least squares (LS) fitting procedure described earlier. To quantify the quality of the fit, the residuals r_i between the experimental and simulated spectra are reported. If a good fit is obtained the residuals should only represent the variations due to statistical noise. The index, 'chi-squared per degree of freedom' (χ^2_r) is also quoted.

The fits to the photoemission lineshape of the Cu2p lines are very good, with small residuals and low χ^2_r values. A surface shifted component was included in the fits with values of the parameters in good agreement with those obtained by Citrin, Wertheim and Baer (CWB) [5]. The intensity of the surface shifted component found by CWB was 0.12 ± 0.03 with a shift of 0.24 ± 0.03eV. The simulations assumed a Doniach-Sunjic (DS) lineshape [6] with an intrinsic lifetime Γ and asymmetry index α. The Gaussian broadening, W, obtained from fitting the Cu2p lines is identical to that obtained from measuring the Fermi edge. The pure Cu2p photoelectron lines were fitted with a single DS lineshape [6] and a surface peak with characteristics given by the work of CWB [5]. The Cu2p lines from the CuPd alloys were fitted with 13 DS bulk component peaks and a surface peak. The charge transfer parameter λ/R was included for the fits to the alloys.

The measured spectrum for the Fermi level was fitted with a step function to obtain the Gaussian resolution of the spectrometer. This was found to be 0.29 ± 0.02eV at Full Width Half Maximum (FWHM).

The fits to the Cu2p lineshape are shown in Fig 4.24 and 4.25 for pure Cu and the $Cu_{50}Pd_{50}$ alloy. The residuals are shown and are represented as a percentage of the total peak height

Figure 4.24: Experimental (solid line) and simulations (circles) for the $Cu2p_{3/2}$ core line in Cu and the associated residuals as a percentage of peak height.

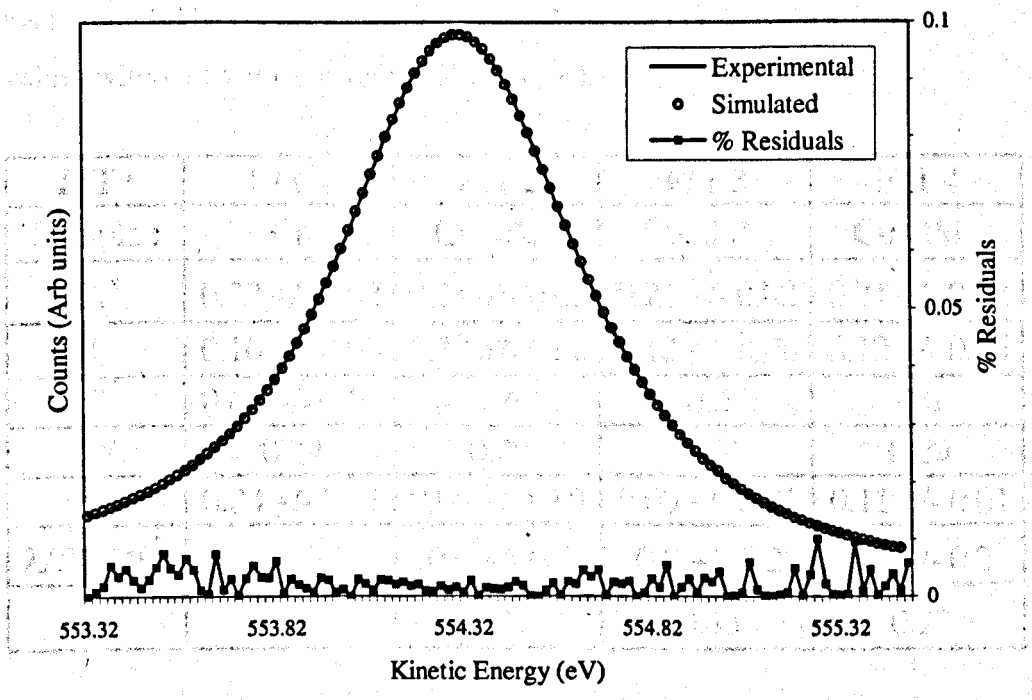

Figure 4.25: Experimental (solid line) and simulations(circles) for $Cu2p_{3/2}$ photoelectron lines for $Cu_{50}Pd_{50}$ alloy. The residuals are shown as a precentage of peak height.

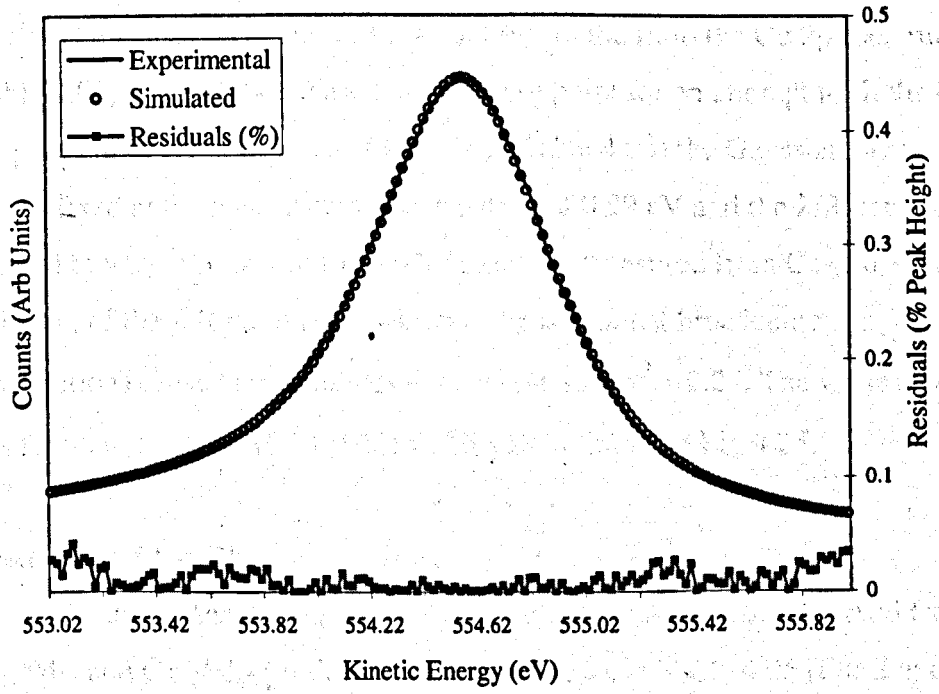

The background in our experimental results is low (Fig 4.22, 4.23) and we follow (CWB) and fit the spectrum to over 1.0eV to the higher kinetic energy side of the photoelectron line and make no explicit allowance for the background. The results for these fits are shown below in table 4.05 (the values without error bars were held constant).

FIT :	FIT 1	FIT 2	FIT 3	FIT 4
Sample :	Cu	$Cu_{88}Pd_{12}$	$Cu_{50}Pd_{50}$	$Cu_{12}Pd_{88}$
E_b^s	0.27 +/- 0.02	0.21 +/- 0.02	0.21 +/- 0.02	0.21 +/- 0.02
I_s	0.10 +/- 0.06	0.12 +/- 0.06	0.12 +/- 0.06	0.12 +/- 0.06
Γ	0.60 +/- 0.03	0.6	0.6	0.6
W	0.29	0.29	0.29	0.29
α	0.04 +/- 0.01	0.06 +/- 0.01	0.09 +/- 0.01	0.11 +/- 0.01
$\lambda/R(x10^{-3})$	_	0.9 +/- 0.2	0.9 +/- 0.2	1.5 +/- 0.2
χ_r^2	0.18	0.27	0.43	0.27

Table 4.05: Fitting Parameters for the Cu2p photoelectron line In CuPd Alloys.

$Cu_{50}Pd_{50}$.

The values obtained for I_s, W and E_b^s in the fit to the Cu 2p spectrum (Table 4.05, Fig 4.24) were used as a starting point for an attempt to fit the Cu 2p spectrum of $Cu_{50}Pd_{50}$. In this fit (FIT 3, Table 4.05) the Gaussian parameter W was fixed at the instrumental contribution of 0.29 eV and the λ/R parameter allowed to vary. For this fit to the Cu2p spectra measured from $Cu_{50}Pd_{50}$, the inclusion of the λ/R parameter (which is the additional broadening contribution) caused the residuals to decrease with χ^2_r =0.27. The value of λ/R was found to be $0.90x10^{-3} \pm 0.20$eV. This fit is shown in Fig 4.25.

$Cu_{88}Pd_{12}$ and $Cu_{12}Pd_{88}$.

A similar analysis of the lineshape of the Cu 2p spectra observed from $Cu_{88}Pd_{12}$ and $Cu_{12}Pd_{88}$ produced the results shown in Table 4.05 (Fits 2 and 4). In both cases it was possible to obtain a good fit to the experimental

results by an increase in the broadening contributions whilst keeping the instrumental Gaussian contribution W constant, at its known value. The values of α and λ/R obtained were 0.060 ± 0.005 and $0.90 \times 10^{-3} \pm 0.20$ eV for $Cu_{88}Pd_{12}$ and 0.110 ± 0.005 and $1.50 \times 10^{-3} \pm 0.20$ eV for $Cu_{12}Pd_{88}$ respectively. It can be seen that the contribution from disorder broadening was less in the high concentration Cu alloys. The broadening was greatest in the 12% Cu alloy as anticipated earlier. The reason for there being less broadening in the $Cu_{88}Pd_{12}$ and $Cu_{50}Pd_{50}$ composition alloys than in the $Cu_{12}Pd_{88}$ sample is probably due to the fact that there are ordered phases present in CuPd alloys at these concentrations [15] and this may lead to local ordering in these samples. In CuPt alloys, the broadening was reduced in a similar way in the $Cu_{75}Pt_{25}$ specimen.

4.52 Magnitude of Charge Transfer in CuPd Alloys.

We follow the same methodology for CuPd as used for the analysis of the charge transfer in CuPt alloys (section 4.13). The charge transfer parameter λ/R has been determined from our fitting procedure, and so the splitting of the bulk components, charge transfer and total broadening can be calculated using the theory described in chapter 3. The inter-atomic distance R (Å) for CuPd is equal to $a/\sqrt{2}$ where 'a' is the lattice constant. Therefore, R= 2.56Å. This means that for the equatorial composition ($Cu_{50}Pd_{50}$) $\lambda = 0.00230e^-$. The splitting between each of the bulk component peaks is calculated from equation 3.11 and is found to be 0.046eV. The total broadening is 4.2 times the individual component splitting [7] which is 0.19eV. The total charge transfer is then $2*\lambda*N_u$ (Eq^n 3.05) and for the 50/50 composition the average number of unlike neighbours is six, giving $Q^i = 0.0276e^-$. If the analysis is extrapolated for the two other compositions, the results are shown in Table 4.06 below. The errors determined for the charge transfer, broadening, splitting and λ are $\pm 0.01e^-$, ± 0.05eV, ± 0.02eV and $\pm 0.001e^-$ respectively.

SAMPLE	$Cu_{50}Pd_{50}$	$Cu_{88}Pd_{12}$	$Cu_{12}Pd_{88}$
λ/R	0.0009	0.0009	0.0015
λ	0.0023	0.0023	0.0038
Splitting (eV)	0.0461	0.0461	0.0769
Total Broadening (eV)	0.1938	0.1938	0.3230
ChargeTransfer (Q)	0.0276	0.0276	0.0461

Table 4.06: Charge Transfer Parameters for CuPd Alloys.

The determination of the charge transfer for CuPd alloys shown in Table 4.06 is the value for a Cu atom surrounded by 6 Pd atoms. Therefore, the lattice site environment is the same, but in different compositions of alloy. The amount of charge transfer for the $Cu_{88}Pd_{12}$ and $Cu_{50}Pd_{50}$ specimens is the same but approximately 40% less than that for the $Cu_{12}Pd_{88}$ sample.

Previous work by Cole *et al* [7,10,11,12] on the CuPd alloy system produced results for the charge transfer, broadening and component splitting shown below in Table 4.07.

SAMPLE	$Cu_{50}Pd_{50}$	$Cu_{80}Pd_{20}$
λ/R	0.0009	0.0012
λ	0.0023	0.0031
Splitting (eV)	0.0461	0.0615
Total Broadening (eV)	0.1938	0.2584
ChargeTransfer (Q)	0.0276	0.0369

Table 4.07: Charge Transfer Parameters for CuPd Alloys [7,10,11,12].

We can see that the results obtained are similar. The results obtained by Cole *et al* for the $Cu_{80}Pd_{20}$ specimen are slightly larger in magnitude than the results in this work for the $Cu_{88}Pd_{12}$ specimen. This is due to the fact that the 80% Cu alloy is not totally in an ordered phase region for CuPd alloys (Fig 4.21) unlike the 88% Cu alloy composition that is in an ordered phase region

for CuPd alloys. The tendency for local ordering to occur in the 80% Cu sample is likely to be reduced compared with that for the 12% Cu alloy.

4.53 Valence Bands in CuPd Alloys.

The valence band structure of Cu, Pd, $Cu_{88}Pd_{12}$, $Cu_{50}Pd_{50}$ and $Cu_{12}Pd_{88}$ is shown below in Figure 4.26.

Figure 4.26: Valence bands in CuPd alloys.

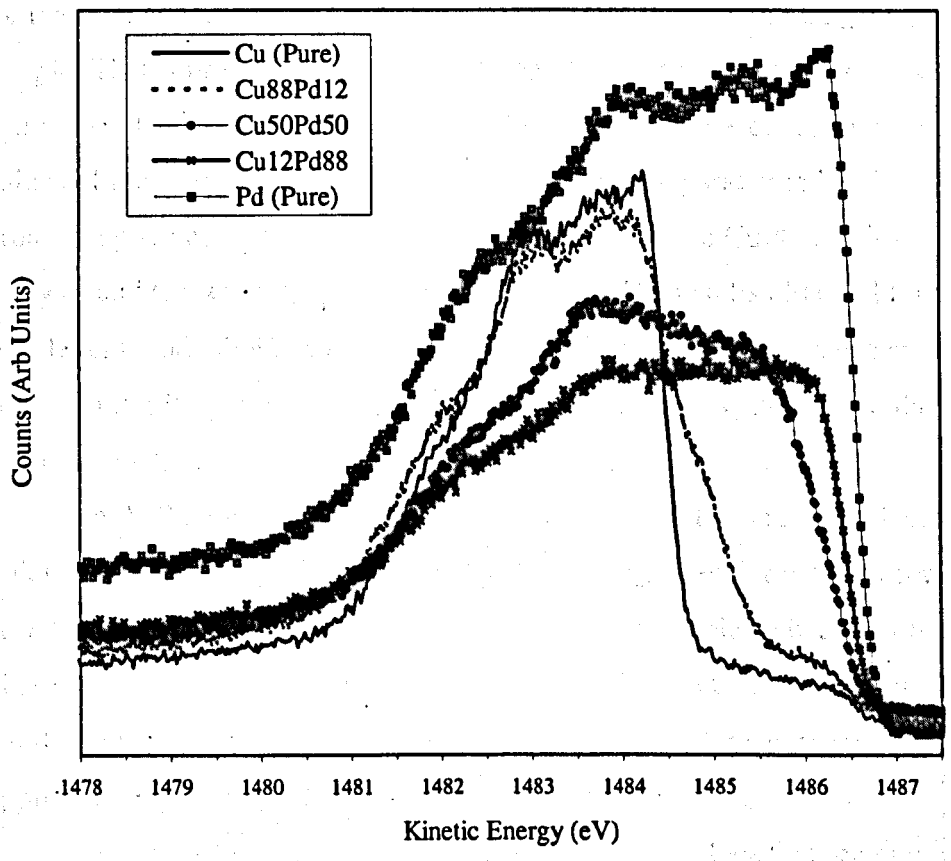

We can see from Fig 4.26, that the density of states for Pd metal at the Fermi level is high. The d-band for Pd in Pd metal is at the Fermi level. The DOS of the CuPd alloy at E_f decreases as we increase the Cu concentration.

The asymmetry parameter for a core level is α. This can be thought of as being proportional to the density of states at the Fermi level [4]. It is apparent that the data for the Pd3d photoelectron lines obey this rule (Fig 4.23) with the asymmetry of the spectra decreasing with the DOS for the alloy at E_f.

In Fig 4.22, Cu2p photoelectron lines in CuPd alloys are shown and they are symmetric. The d-band of Cu in Cu metal lies approximately 2eV below the Fermi level with the s-p band continuing to the Fermi level. This means that for all concentrations of alloy, the Cu component to the total alloy DOS will remain small at the Fermi level even with d-band mixing between the two constituent atomic species.

4.54 Conclusions

The values obtained for the charge transfer and core level broadening for the high concentration Cu alloys are much less than for the $Cu_{12}Pd_{88}$ sample. This is probably due to the ordered phases at these compositions, which may lead to local ordering in the specimens at these concentrations. The values of the charge transfer, bulk component splitting and core level broadening are comparable with those obtained from the CuPt samples analysis and the work of Cole *et al* [7,10,11,12]. The results obtained for the core level broadening of the Cu2p lines in CuPd and CuPt specimens are very similar and it is apparent that the charge transfer in both systems is of the same magnitude where no ordering is present in the alloys.

In AgPd alloys, there are no ordered phases that can result in local order in the specimens. The magnitude of the charge transfer is larger for AgPd than for CuPt or CuPd, even in the Cu based samples where no ordered phases are present. The magnitude of the broadening in CuPd alloys are similar to those in CuPt alloys, but less than in AgPd alloys with values of approximately 0.3eV, 0.3eV and 0.4eV respectively.

A similar trend is seen for the charge transfer values that are quoted for an atomic site that has six unlike neighbours with values of $0.045e^-$, $0.045e^-$ and $0.06e^-$ for CuPd, CuPt and AgPd respectively. A more detailed discussion is given in the next chapter when these values are compared with those calculated from the experimental binding energy and Auger line shifts.

4.6 Evaluation of the Surface Contribution to Core Level XPS Spectra

In Fig 4.23 we see that the lineshape for the $Pd3d_{5/2}$ line in the $Cu_{12}Pd_{88}$ alloy is broader on the low kinetic energy side of the peak than the spectra from the pure metal. This shoulder in the Pd3d spectra was first observed in AgPd alloys ($Ag_{12}Pd_{88}$ sample, Fig 4.16) and attributed to bulk component populations. It is also observable in the $Cu_{12}Pd_{88}$ $Pd3d_{5/2}$ line spectra (Fig 4.23).

The surface contributions to XPS lineshapes for many elements are well known and throughout this work the parameters obtained by Citrin, Wertheim and Baer (CWB) [5] for the surface peak intensity (I_s) and shift (E_b^s) have been quoted. The method used for obtaining the surface peak shift and intensity is to vary the take off angle i.e. angled XPS. Fig 3.4 and Fig 3.5, showed the geometry of such an experiment and the variance of intensity of the surface peak with respect to take off angle.

Samples were cleaned *in-situ* by means of mechanical scraping. This scraping technique was preferred to that of Ar ion bombardment because the bombarding technique can lead to surface enrichment. We need surfaces that are a true representation of the whole alloy composition and Ar ion bombardment can preferentially remove one alloy species. However, the scraping can cause corrugated surfaces as shown in Fig 4.27.

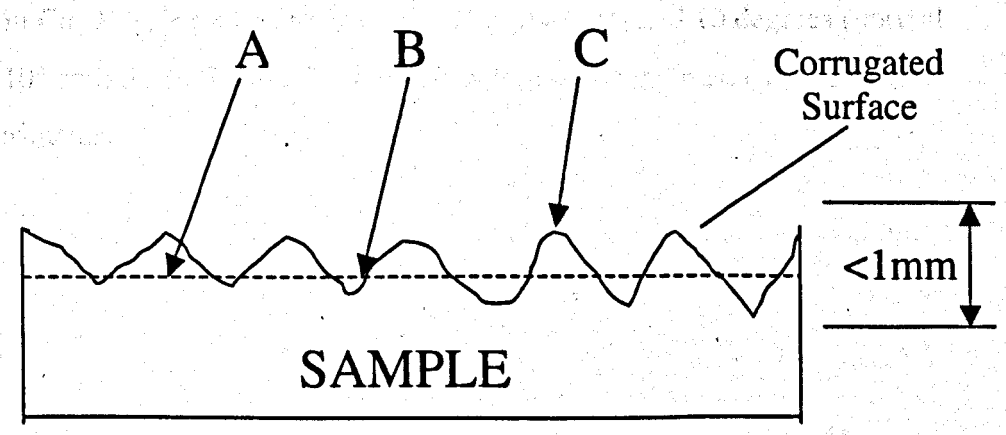

Figure 4.27: Diagram of Sample Surface After Mechanical Scraping.

The diagram (Fig 4.27) illustrates a sample surface after mechanical scraping, which is the technique used to remove contaminants off the sample surface, prior to experimentation. Three points on the sample have been marked: - A, B, and C. The broken line represents points of equal height from the sample base.

If we consider points A and B, they are both at the same height with respect to the sample base. However, a photoelectron exiting from point A will have bulk characteristics and a photoelectron from point B will have surface characteristics. A photoelectron coming from point C will also have surface characteristics. These considerations suggest that XPS measurements from a sample with a rough surface will have a higher percentage of its signal coming from the surface, as there is effectively more of it.

It is important to assess the extent to which the broadening effects studied in this work might be attributed to the effective greater surface peak intensity, being caused by the effect on the sample surface by mechanical scraping.

4.61 Fitting Core Level XPS and Surface Peak Intensity

In our fitting procedure good fits were obtained for spectra measured from scraped surfaces of pure Cu and Ag by using the values obtained by CWB [5] where single crystals were used. For the CuPd samples, angled XPS measurements were taken and below in Fig 4.28, the $Cu2p_{3/2}$ photoelectron line in $Cu_{50}Pd_{50}$ is plotted with a take off angle of 90 and 10 degrees (normal and 10° emission). See Fig 3.4 for description of the geometry in these XPS experiments.

Figure 4.28: $Cu2p_{3/2}$ Spectra from $Cu_{50}Pd_{50}$ Taken at 90 (Normal) and 10 Degree Emission.

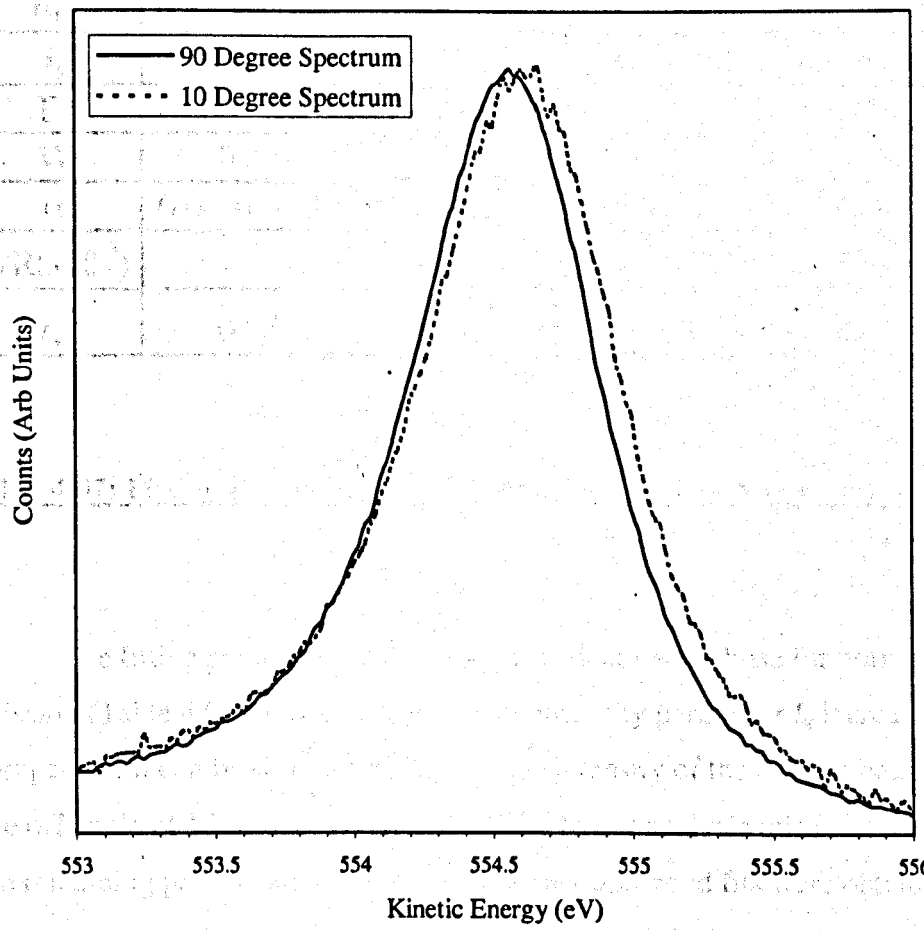

We can see (Fig 4.28) that the spectrum at 10° is indeed broader than that at normal emission. If this effect is due to an increase in the intensity of the surface peak then in a fit to the spectrum at low take off angles the λ/R parameter in our fitting function should not increase. The results of the fits to the $Cu2p_{3/2}$ photoelectron lines in Cu, $Cu_{88}Pd_{12}$, $Cu_{50}Pd_{50}$ and $Cu_{12}Pd_{88}$ at 10° take off angle (T.O.A) are shown in table 4.07.

FIT :	FIT 1	FIT 2	FIT 3	FIT 4
Sample :	Cu	$Cu_{88}Pd_{12}$	$Cu_{50}Pd_{50}$	$Cu_{12}Pd_{88}$
E_b^s	0.27 +/- 0.02	0.21 +/- 0.02	0.21 +/- 0.02	0.21 +/- 0.02
I_s	0.50 +/- 0.06	0.50 +/- 0.06	0.50 +/- 0.06	0.50 +/- 0.06
Γ	0.60 +/- 0.03	0.6	0.6	0.6
W	0.29	0.29	0.29	0.29
α	0.04 +/- 0.01	0.06 +/- 0.01	0.09 +/- 0.01	0.11 +/- 0.01
$\lambda/R(x10^{-3})$	_	0.9 +/- 0.2	0.9 +/- 0.2	1.5 +/- 0.2
χ_r^2	0.25	0.56	0.64	0.34

Table 4.07: Fitting Parameters for the Cu2p at 10° T.O.A in CuPd Alloys.

The fitting parameters (table 4.07) are identical to those for normal emission (Table 4.05) with only the surface intensity parameter I_s increasing as expected. It can be seen in Fig 3.4 that the intensity of the surface peak for a take off angle of 10 degrees should be ~50%. In our analysis this is confirmed. The remaining parameters were allowed to vary and good fits were obtained as seen by the low χ_r^2 values. The charge transfer term λ/R did not alter indicating that the broadening due to the underlying bulk components is not due to surface peak effects caused by the scraping of the sample surface but by the change in core potentials when lattice sites are populated randomly by either a Cu or Pd atom.

Angled resolved XPS measurements were also made for the Pd3d photoelectron lines. The results for the $Pd3d_{5/2}$ line in $Cu_{12}Pd_{88}$ are shown in Fig 4.29. In Fig 4.23 we observe a shoulder in the lineshape for the $Pd3d_{5/2}$ line spectra in the $Cu_{12}Pd_{88}$ alloy (the $Pd3d_{3/2}$ line is not shown for clarity). This effect was also observed in AgPd alloys ($Ag_{12}Pd_{88}$ sample, Fig 4.16) and was deduced to arise from the underlying bulk component populations being visible in the spectra. It is also evident in the $Cu_{12}Pd_{88}$ $Pd3d_{5/2}$ line spectra (Fig 4.23). In Fig 4.29, the shoulder in the $Pd3d_{5/2}$ spectra from $Cu_{12}Pd_{88}$ does not appear as large when the spectra is placed on the same axis as the XPS

measurements taken for this sample at 10° take off angle. This is because the surface peak intensity is increased to ~50%.

Figure 4.29: Pd3d5/2 in $Cu_{12}Pd_{88}$ Photoelectron line at 10 and 90 Degree Take Off Angle

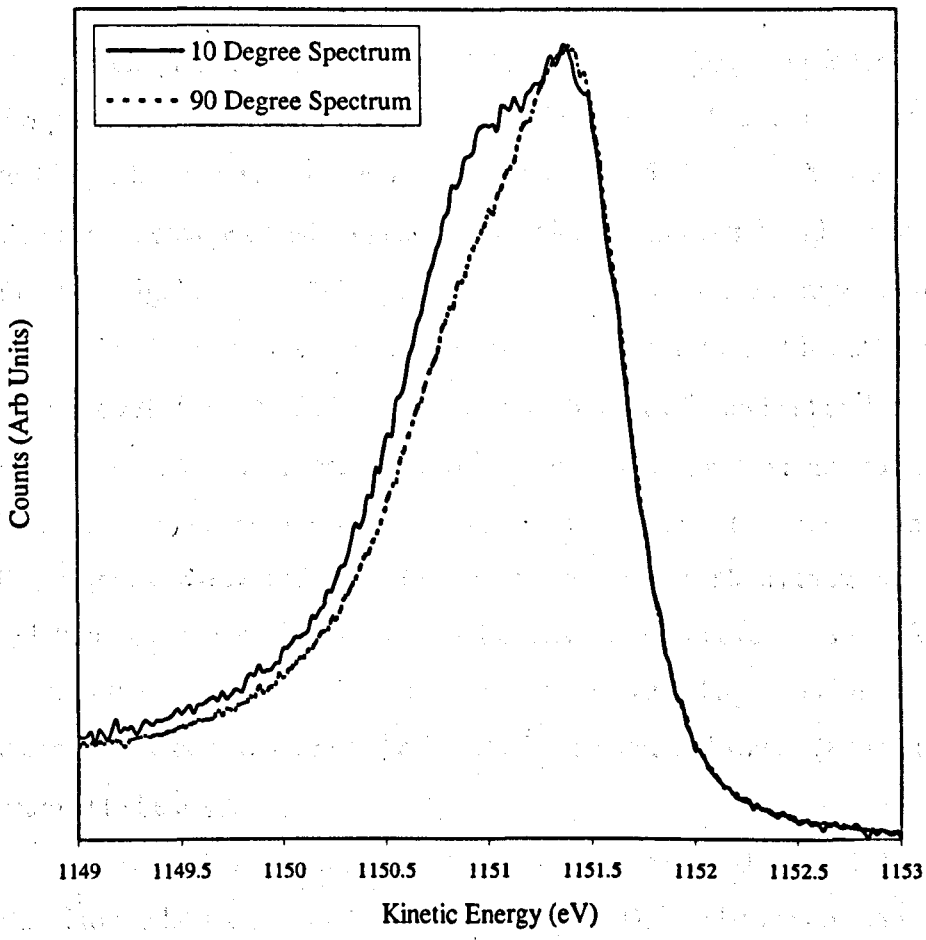

Therefore, the surface peak combines with the underlying bulk peaks that make up the core level lineshape to almost produce a doublet in the $Pd3d_{5/2}$ lineshape. A similar effect was observed for the $Pd3d_{3/2}$ photoelectron line.

We conclude that the broadening in the XPS core level lineshape is indeed due to the spread of potentials in the ground state of the atoms and not an effect of surface peak intensity. The larger surface contribution to the XPS lineshape could have been caused by the preparation of the sample surface by means of mechanical scraping. However, after fitting the $Cu2p_{3/2}$ photoemission lineshape for several CuPd alloys at 10° and 90° take off angle,

the sample preparation technique was found to have no effect on the surface peak intensity.

4.7 Controversy Over The Inter-Nuclear Distance (R)

In chapter 3, the theory behind the charge transfer and broadening of XPS photoelectron spectra was discussed. The inter-nuclear distance R has great importance in such calculations. Equation 3.05, describes how to calculate the charge transfer Q using the ionicity parameter λ and the number of unlike neighbours N_u. N_u is governed by statistics and the composition of the sample. The size of λ does not depend on the magnitude of R but as we determine λ/R from the fitting function, the choice of R can lead to differences in the magnitude of λ. Therefore, it is vital that a reasonable value of R is used if accurate results are to be obtained for the magnitude of the charge transfer in alloy systems. X-ray diffraction (XRD) experiments enable us to determine the lattice parameter 'a' of a crystal solid. XRD finds an average value for the length of the crystal unit cell because it samples over a large specimen volume. If we consider a FCC lattice, the inter-nuclear distance (R) might be assumed to be $a/\sqrt{2}$.

However, this assumes that the local inter-nuclear distance is linearly related to the lattice constant measured using XRD. The lattice constant determined is an average value and therefore, the local R may differ from the macroscopic R.

If we alloy two materials, the lattice parameter 'a' for the alloys normally differs from that of the constituent elements. This is confirmed by XRD experiments (Fig 4.02 and Fig 4.09). If the lattice parameter changes then should the inter-nuclear distance R also alter with it, and will this change be linear or not? This question is not easy to answer, as alloy theory has no way of defining the change in 'a' with a change in R. The problem with XRD experiments is that only information about separation of the crystal planes over large distances is obtained. If an alloy has one small and one large atom species in the unit cell, the dimensions of the unit cell do change. If the value of R was altered at each composition with the change in 'a' then the values

obtained for the charge transfer between atoms could either decrease or increase. EXAFS work on the CuPd and AgPd alloy systems [17,18] determined that the inter-nuclear distance is unchanged in the dilute alloy region for CuPd and AgPd alloys [17]. Further work on the CuPd alloy system [18], found that the inter-nuclear distance between a Cu and a Cu atom in both ordered and disordered Cu_3Pd was unchanged to that of pure Cu. The study on the CuPd alloy system [18] found that the distance between a Cu and a Pd atom is greater than the distance between a Cu and a Cu atom in pure Cu. The work [18] also found that the magnitude of the inter-atomic distances between a Cu atom and a Pd atom in the dilute alloy ($Cu_{99}Pd_1$) to those in ordered and disordered Cu_3Pd specimens did not change. Therefore, the inter-nuclear distance between a Cu atom and a Cu atom in CuPd is assumed to be the same as in the pure element. Conversely, the inter-nuclear distance between a Pd atom and a Pd atom in CuPd is assumed to be the same as in the pure element. The distance between a Cu atom and a Pd atom in CuPd is assumed to not change throughout the compositional range of the alloy.

However, if this was not the case, the maximum difference in 'a' between two elements that are alloyed and studied in this work are between Ni and Pt. With this combination of elements to alloy we have $a^{Ni} = 3.52$Å and $a^{Pt} = 3.92$Å. Therefore, this change in 'a' is 0.2Å for the 50:50 composition. This translates into approximately a 5% difference in 'a' and hence R (if R is assumed to change linearly with 'a'). Considering the errors involved in calculating λ/R, a 5% effect is not appreciable.

Another important issue relevant to this work is the distribution of the charge associated with each atom on a lattice site. Theoretical calculations have been performed [19,20] to find the net charges q^i within the standard Wigner-Seitz cells for the Bravais lattice. These charges were then used to calculate the Coulomb potentials V^i at each lattice site. The net charges are calculated for all the atoms in the alloys, and the average of these charges used as a measure of the charge transfer Q. This method uses the Muffin Tin Approximation (MTA), which means that the charge density is the sum of the core potential which produces a symmetric 'blob' of charge within the Muffin Tin radius. With this approach values have been obtained for the charge

transfer for CuPd and AgPd [21] that are different from those obtained in our experimental XPS data.

Our potential model assumes that the atoms are charged spheres that are centred on a lattice site. This will then exert a uniform potential on surrounding atoms in the nearest neighbour shell. Differences in how you assign the charge will affect the magnitude of charge transfer between nearest neighbour atoms and will lead to varying results.

4.71 A Brief Summary

In this chapter, the charge transfer (where possible with our fitting procedure) has been determined for the CuPt, NiPt, AgPd and CuPd alloy systems. The effects that were originally observed in the CuPd alloy system [7,10,11,12] have been confirmed by this work on CuPd. We expect that the analysis in the next chapter of the binding energy and Auger shifts will yield negligible values for the charge transfer in the NiPt system because there was no change in the core level lineshapes observed from the Pt4f and Ni2p.

The magnitude of the charge transfer found from the analysis of the Cu2p core level in CuPt and CuPd is similar. The measured amount of charge transfer decreases for alloys that have distinct ordered phases in their compositional range. This leads to a tendency for local ordering to occur in the samples at these concentrations. AgPd alloys form no ordered phases throughout their compositional range. This means that we do not expect there to be any local ordering in specimens of this alloy system. The results obtained from the analysis of the Ag3d core level support this view since we find the charge transfer for a specific atomic environment to be identical, independent of the alloy composition. The broadening observed from AgPd alloys was larger than for the other alloy species studied in this work. The surface peak contribution was investigated and it was found that its intensity did not alter due to surface treatments. Angled XPS measurements were measured for the CuPd Cu2p photoelectron line and the surface peak intensity changed to a value that was similar to the theoretical one.

4.8 References

[1] A. Schneider and U. Esch,Z. Electrochem, **50** 290 - 301 (1944).

[2] J.H. Schofield,J. Elec. Spectrosc. Relat. Phenom. **8**, 129 - 137 (1975).

[3] D.R. Penn,J. Elec. Spectrosc. Relat. Phenom. **9**, 29 - 40 (1975).

[4] G.K. Wertheim and P.H. Citrin, "Topics in Apllied Physics" vol26 ed M. Cardona and L. Ley, Berlin: Sringer (1978).

[5] P.H. Citrin, G.K. Wertheim and Y. Baer,Phys. Rev. B **27**, 3160 (1983).

[6] S. Doniach and M. Sunjic,J. Phys. C **3**, 285 (1970).

[7] R.J. Cole, N.J. Brooks and P.Weightman,Phys. Rev. Lett. **78**, 3777 (1997).

[8] T.B. Massalski, H. Okamoto, P. R. Subramanian and L. Kacprzak. Binary Alloy Phase Diagrams 2nd Edition, **2** pp 1460-1462 (ASM International 1990).

[9] T.B. Massalski, H. Okamoto, P. R. Subramanian and L. Kacprzak. Binary Alloy Phase Diagrams 2nd Edition, **2** pp 2843-2845 (ASM International 1990).

[10] R.J. Cole, N.J. Brooks and P.Weightman,Phys. Rev. B **56**, 12178 (1997).

[11] R.J. Cole and P. Weightman,J. Phys: Condens. Matter **9**, 5609 (1997).

[12] R.J. Cole and P. Weightman,J. Phys: Condens. Matter **10**, 5679 (1998).

[13] T.B. Massalski, H. Okamoto, P. R. Subramanian and L. Kacprzak. Binary Alloy Phase Diagrams 2nd Edition, 2 pp 72-74 (ASM International 1990).

[14] P. Weightman, P.T. Andrews, G.M. Stocks and H. Winter. J. Phys. C. Solid State Phys. **16** L81 (1983).

[15] T.B. Massalski, H. Okamoto, P. R. Subramanian and L. Kacprzak. Binary Alloy Phase Diagrams 2nd Edition, 2 pp 1454-1456 (ASM International 1990).

[16] R. Magri, S.H. Wei and A. Zunger,Phys. Rev. B **42** 11388 (1990).

[17] P. Weightman, H. Wright, S.D. Waddington, D. van der Marel, G.A. Sawatzky, G.P. Diakun and D. Norman. Rev. B **36** 9098 (1987).

[18] J.M.C. Thornton, P. Unsworth, M.A. Newell, P. Weightman, C. Jones, R. Bilsborrow and D. Norman. Europhys. Lett. **26** 259 (1994).

[19] J.S. Faulkner, Yang Wang and G.M. Stocks, Phys. Rev. B **55**, 7492 (1997).

[20] J.S. Faulkner, Yang Wang and G.M. Stocks, Phys. Rev. B **52**, 17106 (1995).

[21] J.S. Faulkner, Yang Wang and G.M. Stocks, Phys. Lett. B **81**, 1905 (1998).

CHAPTER 5

Binding Energy and Auger Peak Shifts in CuPt, NiPt, AgPd and CuPd Alloys.

5.1 Photoelectron Binding Energies

For this work, core level and Auger photoelectron spectra have been measured using X-ray Photoelectron Spectra (XPS). The Scienta instrument at the RUSTI facility at the Daresbury Laboratories, was used to collect the data from the four alloy systems (CuPt, NiPt, AgPd and CuPd).

The binding energy of an electron in an orbital *i* is described by: -

$$E_b(i)=h\nu-E_k(i) \qquad (5.01)$$

where $E_b(i)$ is the binding energy of the orbital *i*, hν is the energy of the incident photon and $E_k(i)$ is the kinetic energy of the photoelectron from orbital *i*.

However, if we remove an electron in an orbital *i* from an atom, it would be naive to assume that the remaining atomic system is unaffected. Equation 5.01 only considers the initial effect of removing an electron and makes no allowances for how the atomic system changes. These final state or relaxation effects are caused by the remaining orbitals in the atomic system changing in order to screen the hole created by the photoelectron. To take account of final state effects we write: -

$$E_b(i)=h\nu-E_k(i)-R \qquad (5.02)$$

where R is the relaxation energy. The relaxation reduces the binding energy of the state *i* because as a core hole is created, there is a flow of negative charge that tries to screen the hole. In the 1960's, Bagus [1] was the first to include atomic relaxation effects accompanying inner shell ionisation of atoms.

5.2 Auger Electrons

Pierre Auger first detected the radiationless emission of electrons by core-ionised atoms in cloud chamber experiments in 1925 [2]. He noticed that if the frequency of the incident radiation was increased, the length of one track in the cloud chamber increased while the other remained constant. The energy of an Auger electron (Fig 1.3) is only dependant on the electronic structure of the specific atomic species and unlike photoemission is independent of the exciting radiation.

Therefore, if an electron exits an atom after photoionisation, a core hole is created. If this electron was in the K shell, then an L shell electron can 'fall' into this hole. The electron in the L shell becomes more tightly bound once in the K shell and this excess of energy can cause another L shell electron to exit the atom. The energy 'given' to this secondary L electron is $E_b(K) - E_b(L)$ and hence the Auger electrons from a specific decay can tell us a lot about the electronic structure of elements because they are unique to each element. The KLL (in Auger notation) electron exits the atom with a kinetic energy E_k, of: -

$$E_k = E_b(K) - E_b(LL) \qquad (5.03)$$

where the term $E_b(LL)$ is the binding energy of the two L electron system. $E_b(LL)$ differs from twice the single L electron binding energy $E_b(L)$ due to the effects of relaxation and the interaction between the two holes in the final state. We express the kinetic energy of an Auger electron as: -

$$E_k = E_b(K) - E_b(L) - E_b(L) - \kappa + R^a + R^{ea} \qquad (5.04)$$

Where κ is the Coulomb interaction between the electrons, R^a is the intra-atomic relaxation energy and R^{ea} is the extra-atomic relaxation energy.

5.21 The Auger Parameter

The Auger parameter is defined as the sum of core level binding energies and Auger kinetic energies [3]. The advantage of using this parameter is that it eliminates referencing errors by combining the two measurements. When combining core level binding energies E_b and core-core-core (ccc) Auger kinetic energies E_k for different elements, the changes in the Auger parameter reflect both the changes in the initial ground state potential V and the final state relaxation R. It has been shown [4] that the differences in E_b and E_k are related to changes in V and R by:-

$$\Delta E_b = \Delta V - \Delta R \tag{5.05}$$

$$\Delta E_k \approx -\Delta V + 3\Delta R \tag{5.06}$$

we can separate ΔV and ΔR by defining the initial [5] and final state [6] Auger parameters, β and α respectively: -

$$\Delta\beta = \Delta E_k + 3\Delta E_b \approx 2\Delta V \tag{5.08}$$

$$\Delta\alpha = \Delta E_k + \Delta E_b \approx 2\Delta R \tag{5.09}$$

Therefore, we can use the core level and Auger peak shifts measured for the four alloy species to gain information about changes in the ground state potential and relaxation effects of the atom.

5.3 Fermi Level Shifts

When measuring the shift in peak position for either a core level or Auger peak, we need to reference the positions to a fixed point. In this work the shifts are referenced to the Fermi level, the position of which can be

determined directly in the XPS spectrum. However, problems arise in the interpretation of shifts in core level positions in terms of the potential model when the Fermi level changes upon alloying. The alloys studied in this work are CuPt, NiPt, AgPd and CuPd. It is known that the Fermi level in some alloys changes with alloy composition. The shift in the Fermi level with composition relative to the crystal zero has been calculated for the CuPd alloy system [7]. Unfortunately, such calculations have not been performed for the other three alloy systems studied here.

5.4 The Potential Model and Charge Transfer

To enable us to determine the charge transfer in the four alloys studied in this work, we need to be able to model how the ground state potential V alters in the atomic cores. A ground state potential model was developed by Siegbahn *et al* [8,9] who related core level binding energy shifts to differences in local potential between two chemical environments: -

$$\Delta E_b \approx \Delta V = \Delta V^V + \Delta V^M \qquad (5.10)$$

where ΔV is the change in local potential, ΔV^V is the intra-atomic potential that a core electron experiences from the valence electrons and ΔV^M is the extra-atomic or Madelung potential (assuming a point charge approximation) that arises from the charge distribution in other neighbouring atoms.
Using (5.10) we obtain the familiar 'Potential Model' [3,8,9]: -

$$\Delta V = \Delta q\left(k - 14.4\frac{\alpha_M}{R} \right) \qquad (5.11)$$

where R (Å) is the inter-atomic distance, k is the contribution per valance electron [3], q is the charge transfer and α_M is the Madelung potential constant. The Madelung energy constant for disordered alloys were obtained by Magri *et al* [10] and are shown in Fig 5.01: -

Figure 5.01: Madelung Constant for Varying Compositions of Disordered FCC Lattices

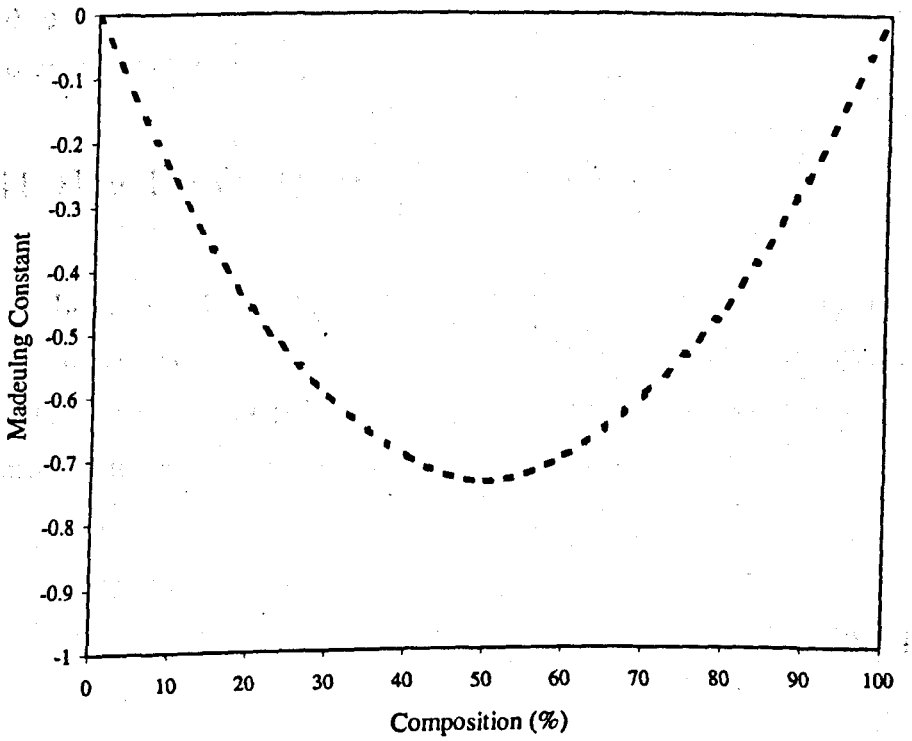

However, the Madelung potential constant for a random lattice is $\alpha_M \cong 1$. If we combine equation 5.08 with 5.11, we obtain the expression for the change in the initial state Auger parameter $\Delta\beta$: -

$$\Delta\beta \approx 2\Delta q\left(k - 14.4\frac{\alpha_M}{R}\right) \qquad (5.12)$$

with this approximation and rearrangement of equation 5.12 we can determine the charge transfer from:-

$$\Delta q = \frac{\Delta \beta}{2\left(k - 14.4 \frac{\alpha_M}{R} \right)} \qquad (5.13)$$

Therefore, we can determine the charge transfer from Auger and binding energy shifts. The same values of the inter atomic distance R (Å) for the four alloy systems as used in chapter 4 are used in the calculations of the charge transfer in this chapter.

5.41 How Do We Determine the Magnitude of k?

In equation 5.11 the parameter k is used. It is described as being the contribution of each valence electron to the core potential. Alternatively, it can be thought of as how the potential of the atomic core changes as each of the valance electrons is removed. It can be approximated to: -

$$k = 14.4 \frac{2}{R} \qquad (5.14)$$

where R (Å) is the inter atomic distance and 14.4 is a multiplicative constant. There has been considerable discussion of how to determine k [3,11,12] and depending on which method is chosen, the magnitude of k can differ for Cu for example by up to a factor of 2 [13]. The chosen method for determining k in reference 13 was equation 5.14. This method gave a value of k^{Cu} to be 11.2eV [13]. In this work we use this method for determining k. The values of k for the elements used in this work are in Table 5.01.

Element	Cu	Ni	Pt	Pd	Ag
Lattice Constant (Å)	3.61	3.52	3.92	3.89	4.09
R (Å)	2.55	2.49	2.77	2.75	2.89
k (eV)	11.28	11.57	10.39	10.47	9.96

5.5 Charge Transfer Determined from Auger and Binding Energy Shifts

5.51 CuPt Experimental Spectra

X-ray photoelectron spectroscopy (XPS) measurements were taken for the $Cu2p_{3/2}$ core level and the $L_3M_{2,3}M_{2,3}$ Auger line for Cu in CuPt alloys. Conversely, the $Pt4f_{5/2}$ and $Pt4f_{7/2}$ core level and $M_5N_{6,7}N_{6,7}$ Auger line for Pt in CuPt alloys were measured. The $Cu2p_{3/2}$ and Pt4f photoelectron spectra were shown in the previous chapter Fig 4.03 and Fig 4.05 respectively. In Fig 5.02, the Auger spectra for the Cu $L_3M_{2,3}M_{2,3}$ transition for Cu, $Cu_{75}Pt_{25}$, $Cu_{50}Pt_{50}$ and $Cu_{25}Pt_{75}$ are shown.

Figure 5.02:Cu $L_3M_{2,3}M_{2,3}$ Auger photoelectron line in CuPt alloys

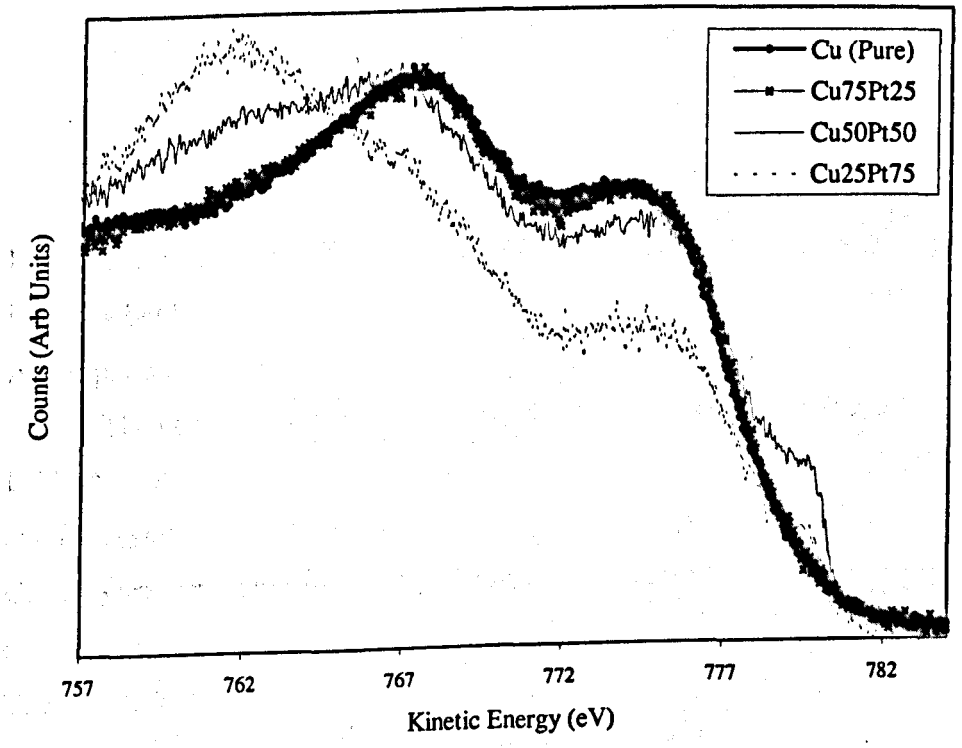

In Fig 5.03, the $L_3M_{4,5}M_{4,5}$ Auger lines for Pt in CuPt alloys are shown.

Figure 5.03: Pt $M_5N_{6,7}N_{6,7}$ Auger Photoelectron Line in CuPt alloys

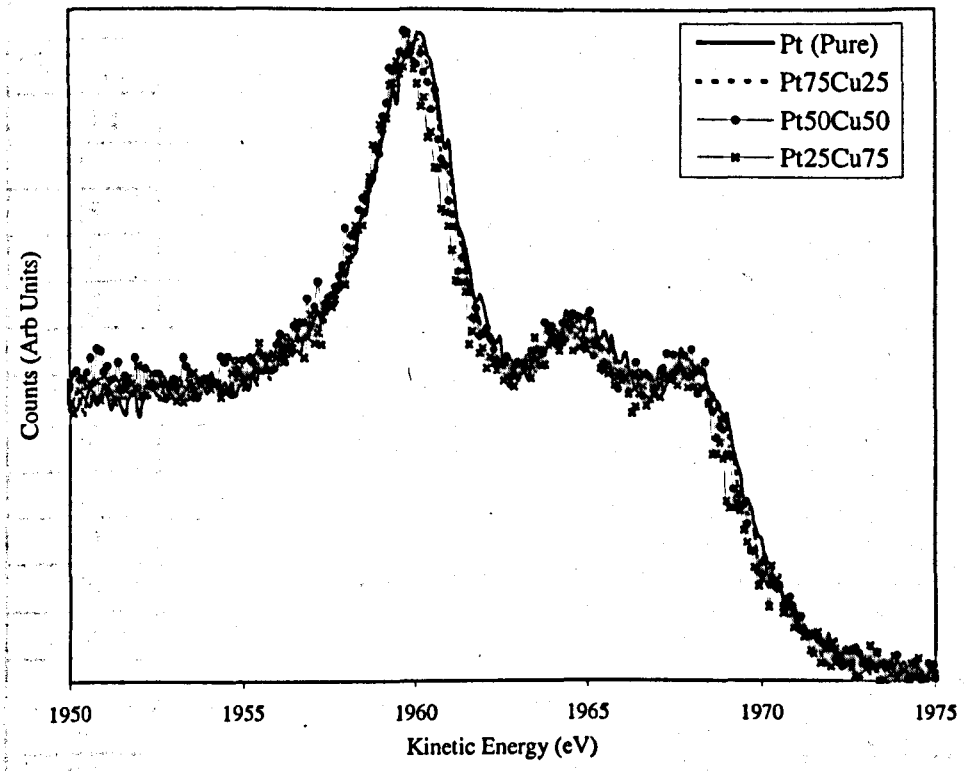

In both Fig 5.02 and Fig 5.03, the data has been normalised to a common peak intensity but has not been aligned in energy. One can see a definite shift in the Auger photoelectron peaks for both Pt and Cu.

The peak positions and shifts for the $Cu2p_{3/2}$ core level and the $L_3M_{2,3}M_{2,3}$ Auger line for Cu, $Cu_{75}Pt_{25}$, $Cu_{50}Pt_{50}$ and $Cu_{25}Pt_{75}$ and the $Pt4f_{5/2}$ and $Pt4f_{7/2}$ core levels and $M_5N_{6,7}N_{6,7}$ Auger line for Pt, $Cu_{75}Pt_{25}$, $Cu_{50}Pt_{50}$ and $Cu_{25}Pt_{75}$ are shown in Table 5.02. The positions of the largest Auger component peak were used as the reference point for measurements of shifts. The core level binding energy E_b and the shift in core level binding energy ΔE_b are all quoted to an accuracy of ± 0.02eV. The kinetic energy of the Auger spectra E_k and the shift in the Auger kinetic energy ΔE_k are all quoted to an accuracy of ± 0.10eV. The Auger parameter shifts $\Delta\alpha$ (which are a measure of the atomic relaxation) are also quoted to an accuracy of ± 0.10eV.

The larger error on the Auger peak shifts arise from the step width in such scans being bigger because of the larger energy range that the data was taken over.

Cu 2p 3/2					
% Pt	E_b	ΔE_b	E_k	ΔE_k	$\Delta\alpha = \Delta E_b + \Delta E_k$
0	932.68	0.00	767.35	0.00	0.00
25	932.44	-0.24	767.35	0.00	-0.24
50	932.20	-0.48	766.90	-0.45	-0.93
75	931.96	-0.72	766.90	-0.45	-1.17
Pt $4f_{5/2}$					
% Cu	E_b	ΔE_b	E_k	ΔE_k	$\Delta\alpha = \Delta E_b + \Delta E_k$
0	71.12	0.00	1960.10	0.00	0.00
25	71.12	0.00	1959.90	-0.20	-0.20
50	71.08	-0.04	1959.80	-0.30	-0.34
75	71.06	-0.06	1959.70	-0.40	-0.46
Pt $4f_{7/2}$					
% Cu	E_b	ΔE_b	E_k	ΔE_k	$\Delta\alpha = \Delta E_b + \Delta E_k$
0	74.48	0.00	1960.10	0.00	0.00
25	74.46	-0.02	1959.90	-0.20	-0.22
50	74.4	-0.08	1959.80	-0.30	-0.38
75	74.4	-0.08	1959.70	-0.40	-0.48

Table 5.02: Core Level and Auger Peak Shifts for CuPt Alloys.

If we consider the binding energy shifts ΔE_b for the Cu photoelectron lines in CuPt alloys, the shift is large with a maximum value of -0.72eV for the $Cu_{25}Pt_{75}$ sample and increases approximately linearly with composition (Fig 5.04). The shift in the Auger peak is not linear (Fig 5.04). There is no shift until 50% of the alloy is Pt and then the shift is –0.45eV.

If we combine the shift of the Auger and core level, we gain a measure of the atomic relaxation (Eq^{n} 5.09) from the shift in the Auger parameter $\Delta\alpha$. For Cu, the relaxation is rather large having a value of –0.59eV.

If we create a core hole, there is an effective positive charge created. The electron orbitals then shift to the +ve charge to try and neutralise it and become more bound because the core hole is in the orbital nearest to the

nucleus of the atom. This is one explanation of why the relaxation energy is high for Cu.

Figure 5.04: Cu2p Binding energy and Auger shifts as a function of Pt concentration in CuPt alloys.

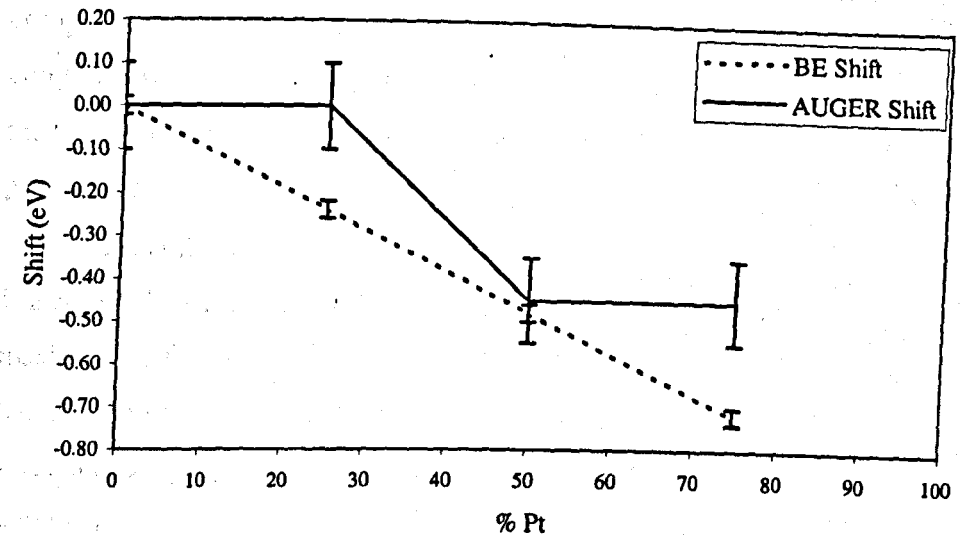

Figure 5.05: Pt4f5/2 Binding energy and Auger shifts as a function of Cu concentration in CuPt alloys.

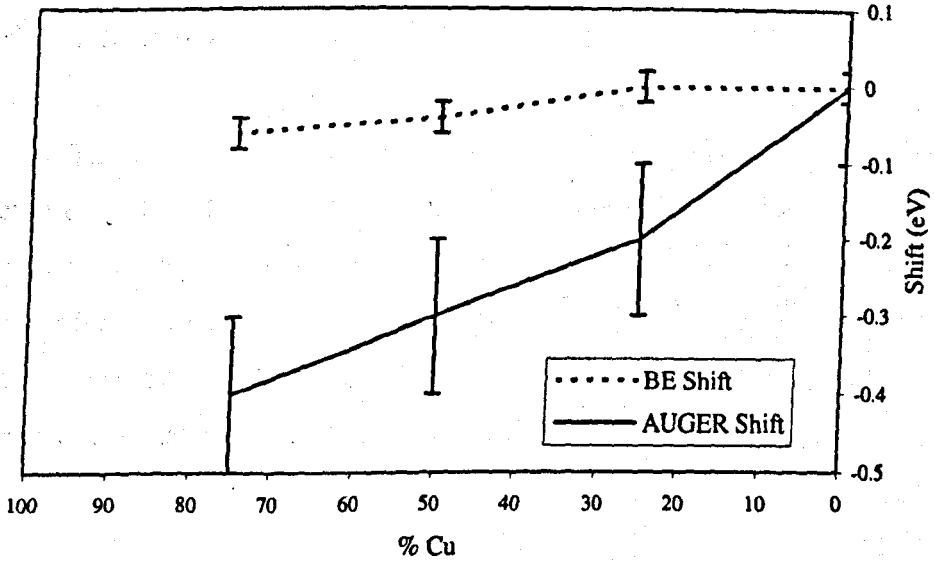

In Figure 5.05, the core level binding and Auger kinetic energy shifts for Pt in CuPt alloys are shown (only the shifts for the $Pt4f_{5/2}$ photoelectron

line is shown as the values are the same as those for the $4f_{7/2}$ peak). It is evident that the Pt4f photoelectron lines do not shift significantly as Pt is alloyed with Cu. The maximum shift is only -0.08eV which is small considering the error of ± 0.02eV.

The Pt $M_3N_{6,7}N_{6,7}$ Auger line (Fig 5.03) changes in energy with composition and the shift is almost linear with composition (Fig 5.05). When combined with the binding energy shift to obtain the Auger parameter shift for the $Cu_{75}Pt_{25}$, $\Delta\alpha$ is –0.48eV. The relaxation is then half this value, therefore ΔR = -0.24eV.

This relaxation energy is considerably less than that for Cu (-0.59eV). If a core hole is created by photoionisation, the effective +ve charge created is masked by a flow of electrons (negative charge) to that hole. Pt has a full d-band at the Fermi level throughout the compositional range of the alloys studied and so any effective change in charge in the atomic core will be screened.

It is reasonable to say then, that Cu cannot screen a core hole sufficiently, whereas in Pt the core hole only affects the atoms electronic structure by a small amount.

5.52 Magnitude of the Charge Transfer in CuPt alloys

The shifts for the Auger and core level photoelectron peaks have been measured and can be used to determine the charge transfer in CuPt alloys. We use the values of the shifts with equations 5.08 and 5.13 to calculate the charge transfer for each element in the alloy. The results are shown for Cu in CuPt alloys in Table 5.03. The results for Pt in CuPt alloys is shown in Table 5.04. The error calculated for the charge transfer parameter was ± 0.01e^-

Sample	α_M	$\Delta\beta$	k	R	Charge Transfer (e)
$Cu_{75}Pt_{25}$	1.000	-0.720	11.280	2.553	-0.064
$Cu_{50}Pt_{50}$	1.000	-1.89	11.280	2.553	-0.168
$Cu_{25}Pt_{75}$	1.000	-2.610	11.280	2.553	-0.231

Table 5.03: Charge Transfer Parameters for Cu in CuPt Alloys.

Sample	α^M	$\Delta\beta$	k	R	Charge Transfer (e)
$Cu_{75}Pt_{25}$	1.000	-0.260	10.390	2.774	0.025
$Cu_{50}Pt_{50}$	1.000	-0.42	10.390	2.774	0.040
$Cu_{25}Pt_{75}$	1.000	-0.580	10.390	2.774	0.056

Table 5.04: Charge Transfer Parameters for Pt in CuPt Alloys.

The asymmetry of the Pt4f core levels prevented an analysis of the broadening of the lineshape to determine the charge transfer for the Pt4f photoelectron lines in chapter 4 and so a comparison cannot be made. However, the charge transfer was determined from analysing Cu2p spectra for CuPt alloys. If we recall Table 4.02: -

SAMPLE	$Cu_{50}Pt_{50}$	$Cu_{75}Pt_{25}$	$Cu_{25}Pt_{75}$
λ/R	0.0015	0.0010	0.0012
λ	0.0038	0.0026	0.0031
Splitting (eV)	0.0769	0.0513	0.0615
Total Broadening (eV)	0.3230	0.2153	0.2584
ChargeTransfer (Q)	0.0461	0.0307	0.0369

Table 4.02: Charge Transfer and Broadening for Cu2p in CuPt Alloys.

5.53 Comparisons with XPS Core Level Analysis

In chapter 4, the charge transfer was determined from the analysis of core level XPS spectra for the $Cu2p_{3/2}$ photoelectron line in CuPt alloys. In this chapter a different methodology is used and the charge transfer is determined from the shifts in the Cu2p, Pt4f and Auger spectra. The two different sets of results can be compared for the Cu constituent in CuPt alloys, but unfortunately not for the Pt photoelectron lines.

5.54 $Cu_{75}Pt_{25}$ Specimen

Cu: -

The amount of the charge transfer determined for the $Cu2p_{3/2}$ core level in chapter 4 for this sample was found to be $0.03 \pm 0.01e^-$ (Table 4.02). This was for a Cu atom surrounded by 6 Pt atoms in a FCC unit cell. This magnitude of charge transfer was lower than expected and was deduced as being caused by the presence of local ordering in the specimen at this composition. A look at the alloy phase diagram for CuPt confirms that there is an ordered phase at this composition (Fig 4.01).

The analysis of the core level binding and Auger kinetic energy shifts for the Cu component in CuPt alloys in this chapter gave a value for the charge transfer of $-0.064 \pm 0.01e^-$ (Table 5.03). This value is for a Cu site surrounded by (on average) 3 Pt neighbours and 9 Cu neighbours. Therefore, if we use the charge transfer value obtained from the Cu2p core level analysis for a Cu site with six unlike neighbours and alter it to being a site with 3 unlike neighbours in the nearest neighbour shell, we get a value for the charge transfer to be $0.02 \pm 0.01e^-$. This value is only approximately 30% of that obtained from the binding energy and Auger shifts.

The magnitude of the charge transfer is less than for the $Cu_{50}Pt_{50}$ and $Cu_{25}Pt_{75}$ samples and this is because of the local ordering that exists in the specimen at this composition.

Pt: -

The charge transfer determined from the binding energy and Auger kinetic energy shifts for the Pt4f and $M_5N_{6,7}N_{6,7}$ for the $Cu_{75}Pt_{25}$ sample was 0.025 ± 0.01e⁻. This is considerably less than the value obtained for Cu from the spectral peak shifts, which is surprising because the total amount of charge should be conserved i.e. what one atom loses, another must gain. However, the results are comparable with those obtained from the Cu2p core level broadening analysis.

5.55 $Cu_{50}Pt_{50}$ Specimen

Cu: -

The amount of charge transfer was found to be 0.17 ± 0.01e⁻ from the core level and Auger peak shifts. The Cu2p core level lineshape analysis in chapter 4 gave a value of 0.05 ± 0.01e⁻. The magnitude of the charge transfer obtained from the core level lineshape analysis was again only approximately 30% of the value obtained from the spectral peak shifts.

Pt: -

The value of 0.04 ± 0.01e⁻ for the charge transfer determined from the Pt4f and Auger peak shifts is much smaller than the values obtained from the Cu spectra analysis (0.17 ± 0.01e⁻). It is similar however to the magnitude obtained from the Cu2p lineshape analysis in chapter 4 (0.05 ± 0.01e⁻).

5.56 $Cu_{25}Pt_{75}$ Specimen

Cu: -

The magnitude of charge transfer for this system determined from peak shifts was 0.23 ± 0.01e⁻. The value obtained from the core level analysis in chapter 4 was only 0.04 ± 0.01e⁻. However, this lesser value was for a Cu site with 6 unlike neighbours in the nearest neighbour shell and in this alloy composition there is on average 9 unlike neighbours. Therefore, when the charge transfer value is recalculated for this environment, the amount

increases to 0.07 ± 0.01e⁻, which is once again only approximately 30% of that obtained from the spectral peak shift analysis.

Pt: -

The charge transfer is again less than that obtained from the Cu spectra analysis with a value of 0.06 ± 0.01e⁻. It is consistent with the charge transfer value gained from the Cu2p core level analysis done in chapter 4 (0.07 ± 0.01).

5.57 Summary of CuPt Analysis

The magnitude of the charge transfer determined from binding energy and Auger peak shifts (for the Cu component) are approximately 30% of those values obtained from the Cu2p core level photoelectron lineshape analysis in CuPt alloys; carried out in chapter 4. These differences probably arise because of the neglect of the shifts in the Fermi level as Cu and Pt are alloyed. In deducing $\Delta V = V_{CuPt} - V_{Cu}$ we have ignored the contribution that would arise from the difference in Fermi energy of CuPt and pure Cu. The Fermi level shifts for the CuPt alloy system have not been calculated and there is no way of accounting for them. The magnitudes of the charge transfer obtained using the methodology in this chapter are an overestimate, if those obtained from the core level lineshape analysis are taken as the true values.

However, the magnitudes of charge transfer determined for the Pt components in CuPt alloys in this chapter are surprising. The values are consistent with those obtained from the Cu2p core level analysis in chapter 4. This corresponds well with the conservation of charge. The values of the charge transfer determined from spectral peak shifts are much less for the Pt than those obtained for the Cu component in CuPt alloys.

A contributory factor for the reduced value of the charge transfer obtained from the Pt photoelectron peak shifts is the determination of k. If we recall section 5.41, equation 5.14 was the definition chosen for k. Work on the Cu2p shifts in the CuPd alloy system [12] showed that the value of k chosen for a free atom differs greatly if we are dealing with s-p or d-band atoms. For

Cu, the difference between the values of k obtained from a consideration of d and sp valance electrons can be up to a factor of 2. The method chosen for this work (equation 5.14) gave results for the Cu component in CuPd alloys, which was in between the two extremes. In Pt, the valence structure is mostly d-band in character (Fig 4.06) and so the value of k chosen will be an underestimate. If this effect were taken into account and k was increased, the charge transfer determined from equation 5.14 would increase.

This model (equation 5.14) for k gives larger values for the charge transfer for Cu shifts in CuPt alloys compared with the Cu2p core level analysis in chapter 4. For Pt the d-band is at the Fermi level and so will mix with the s-p band of Cu. Any change in the two will lead to s-p and d-band changes which will alter the atomic parameters such as k considerably. This is a factor that will alter the magnitude of the Pt charge transfer in CuPt alloys and could account for the differences from those values obtained from the Cu spectral peak shifts analysis. Why the magnitude of the charge transfer is larger than those obtained from the Cu2p core level lineshape is probably mostly due to the fact that no Fermi level shifts were included in this work. If the Fermi level shifts had the effect of decreasing the binding energy and Auger shifts, then the amount of charge transfer would be reduced significantly.

5.6 NiPt Core Level and Auger Peak Shifts

In chapter 4, both the $Ni2p_{3/2}$ and the $Pt4f_{5/2}$ ($Pt4f_{7/2}$) core levels could not be analysed to determine charge transfer broadening using our fitting function because of the highly asymmetric lineshape. It was expected that the charge transfer and broadening in this alloy system would be negligible as there was no change in the spectral lineshape measured from Pt and only asymmetry changes in the Ni spectra. Also, the elements were in the same group in the periodic table. In this section we analyse the shifts in the core level and Auger peaks.

X-ray photoelectron spectroscopy (XPS) measurements were taken for the $Ni2p_{3/2}$ core level and the $L_3M_{2,3}M_{2,3}$ Auger line for Ni in NiPt alloys. The $Pt4f_{5/2}$ and $Pt4f_{7/2}$ core level XPS lines and $M_5N_{6,7}N_{6,7}$ Auger line for Pt in NiPt alloys were also measured. The $Ni2p_{3/2}$ and Pt4f photoelectron spectra are shown in the previous chapter Fig 4.11 and Fig 4.12 respectively. In Fig 5.05, the Auger spectra for the Ni $L_3M_{2,3}M_{2,3}$ Auger transition for Ni, $Ni_{75}Pt_{25}$, $Ni_{50}Pt_{50}$ and $Ni_{25}Pt_{75}$ are shown. The data have been normalised with respect to the peak height for pure Ni.

Figure 5.06: Ni Auger in NiPt Alloys.

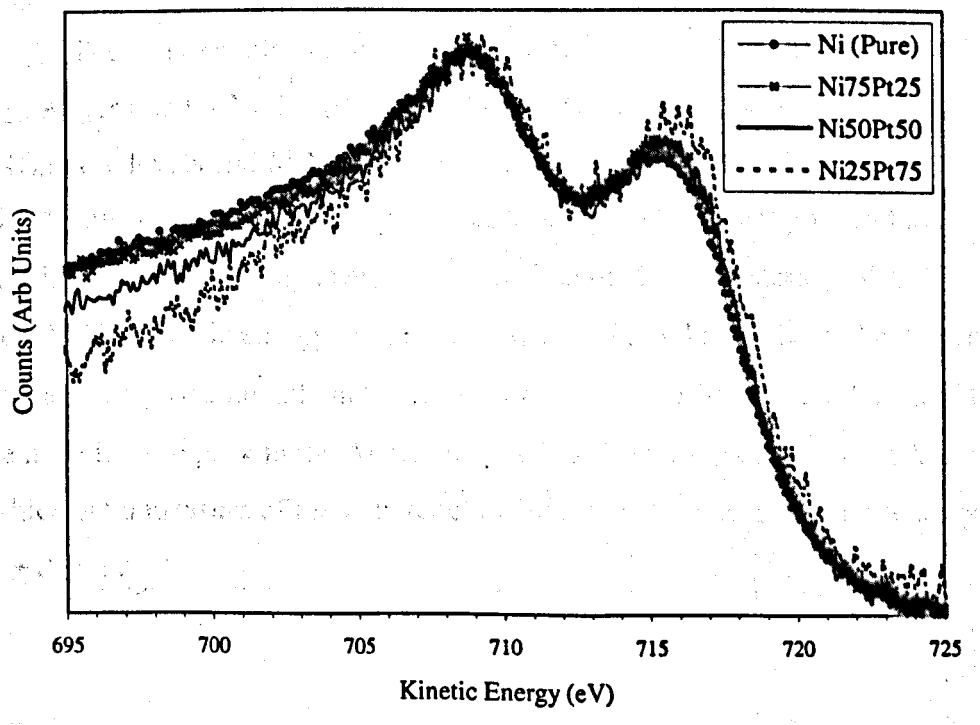

In Figure 5.07, the $M_5N_{6,7}N_{6,7}$ Auger spectra Pt in NiPt alloys are shown. The data has not been aligned in energy and only normalised with respect to the peak height for pure Pt.

Figure 5.07: Pt Auger in NiPt alloys.

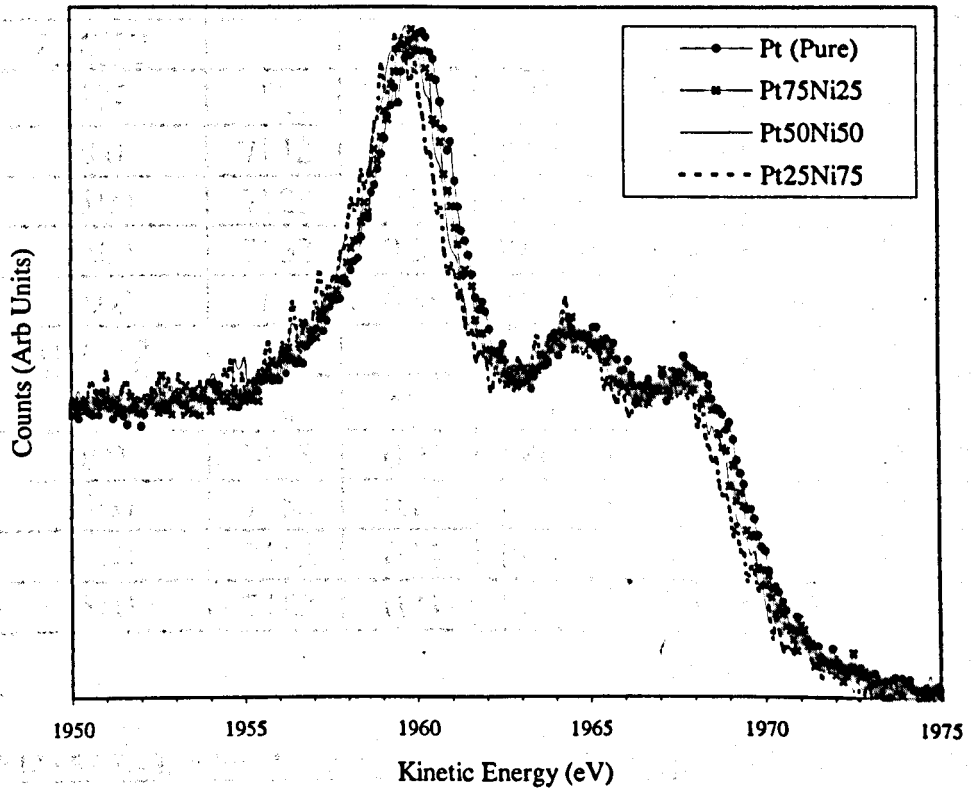

The peak positions and shifts for the $Ni2p_{3/2}$ core level and the $L_3M_{2,3}$ $M_{2,3}$ Auger line for Ni, $Ni_{75}Pt_{25}$, $Ni_{50}Pt_{50}$ and $Ni_{25}Pt_{75}$ and the $Pt4f_{5/2}$ and $Pt4f_{7/2}$ core levels and $M_5N_{6,7}N_{6,7}$ Auger line for Pt, $Ni_{75}Pt_{25}$, $Ni_{50}Pt_{50}$ and $Ni_{25}Pt_{75}$ are shown in Table 5.05. The core level binding energy E_b and the shift in core level binding energy ΔE_b are all quoted to an accuracy of ± 0.02eV. The kinetic energy of the Auger spectra E_k and the shift in the Auger kinetic energy ΔE_k are all quoted to an accuracy of ± 0.10eV and referenced to the most intense peak in the Auger spectra. The Auger parameter shifts $\Delta\alpha$ (which are a measure of the atomic relaxation) are also quoted to an accuracy of ± 0.10eV.

Ni 2P3/2					
%Pt	E_b	ΔE_b	E_k	ΔE_k	$\Delta\alpha = \Delta E_b + \Delta E_k$
0.00	852.60	0.00	708.70	0.00	0.00
25.00	852.52	-0.08	708.80	0.10	0.02
50.00	852.38	-0.22	708.90	0.20	-0.02
75.00	852.36	-0.24	709.00	0.30	0.06
Pt 4F5/2					
%Ni	E_b	ΔE_b	E_k	ΔE_k	$\Delta\alpha = \Delta E_b + \Delta E_k$
0.00	71.12	0.00	1960.10	0.00	0.00
25.00	71.28	0.16	1959.90	-0.20	-0.04
50.00	71.32	0.20	1959.70	-0.40	-0.20
75.00	71.46	0.34	1959.50	-0.60	-0.26
Pt 4F7/2					
%Ni	E_b	ΔE_b	E_k	ΔE_k	$\Delta\alpha = \Delta E_b + \Delta E_k$
0.00	74.48	0.00	1960.10	0.00	0.00
25.00	74.58	0.10	1959.90	-0.20	-0.10
50.00	74.62	0.14	1959.70	-0.40	-0.26
75.00	74.82	0.34	1959.50	-0.60	-0.26

Table 5.05:- Binding Energy and Auger Peak Shifts in NiPt Alloys.

If we consider the binding energy shifts ΔE_b for the Ni photoelectron lines in NiPt alloys, the shift is small with a maximum value of -0.24eV for the $Ni_{25}Pt_{75}$ sample and increases approximately linearly with composition (Fig 5.08). The shift in the Auger peak is linear with composition (Fig 5.08). If we combine the shift of the Auger and core level, we gain a measure of the atomic relaxation (Eq^{n} 5.09) from the shift in the Auger parameter $\Delta\alpha$. For Ni, the relaxation is negligible having a value of –0.06eV considering the error of ± 0.1eV. One might expect that the magnitude of the relaxation for both the Ni and Pt components in NiPt alloys will be small. This is because the d-band remains nearly completely filled for both elements throughout the compositional range and d-band screening of core holes is more effective than sp-band screening .

Figure 5.08: Ni2p Binding energy and Auger shifts as a function of Pt concentration in NiPt alloys.

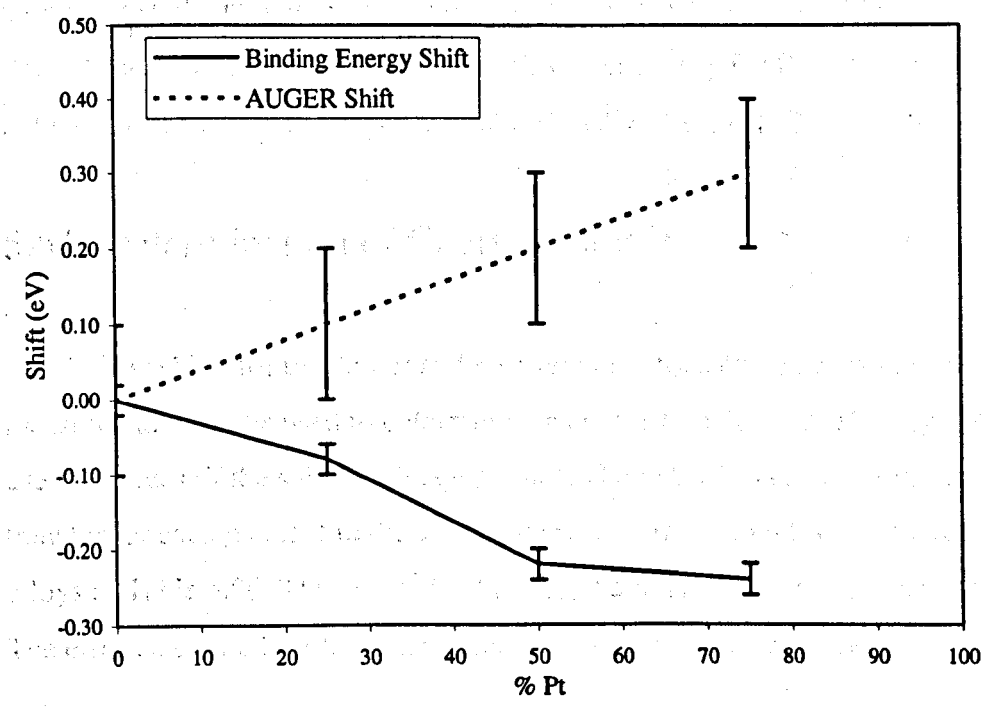

Figure 5.09: Pt4f5/2 binding energy and Auger shifts as a function of Ni concentration in NiPt alloys.

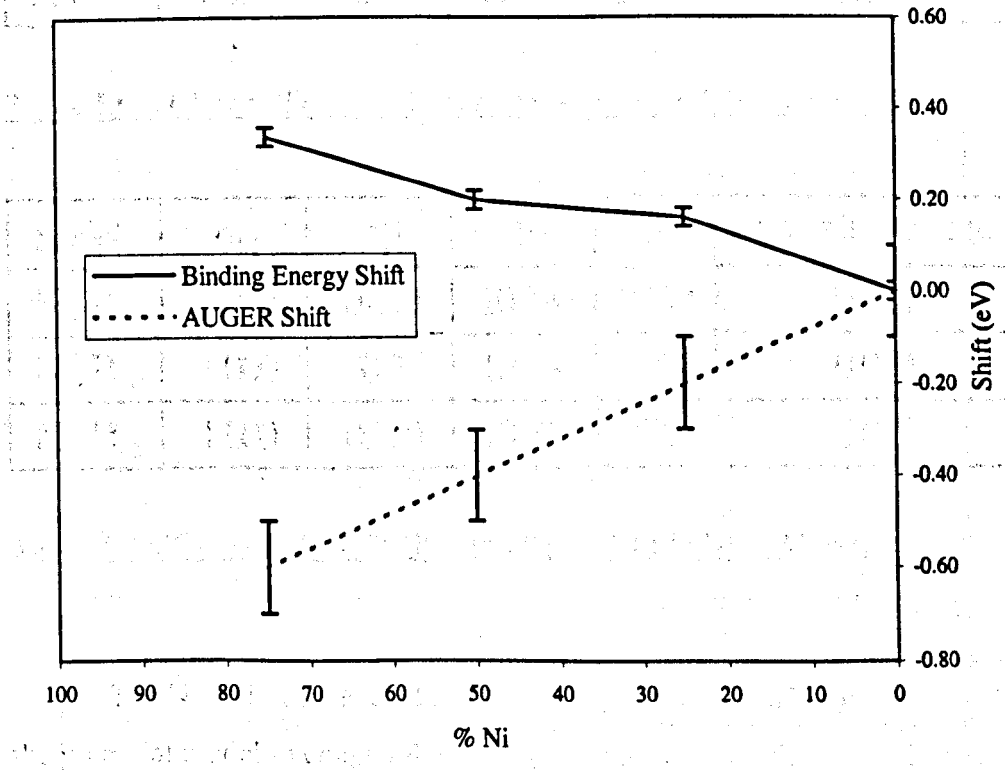

The Pt binding energy and Auger shifts are again almost linear with composition (Fig 5.09). When the shifts are combined to form the Auger parameter α, the magnitude is almost half that in CuPt alloys (Table 5.02), -0.26eV compared with -0.48eV. The relaxation energy for Pt in NiPt is then not significant within the experimental error $R^{Pt} = 0.1 \pm 0.1eV$.

5.61 Determination of Charge Transfer

The shifts for the Auger and core level photoelectron peaks have been measured and can be used to determine the charge transfer in NiPt alloys. We use the values of the shifts with equations 5.08 and 5.13 to calculate the charge transfer for each element in the alloy. The results are shown for Ni in NiPt alloys in Table 5.06. The results for Pt in NiPt alloys is shown in Table 5.07. The error calculated for the charge transfer parameter was $\pm 0.01e^-$.

Sample	α_M	$\Delta\beta$	k	R	Charge Transfer (e^-)
$Ni_{75}Pt_{25}$	1.000	-0.120	11.570	2.494	-0.010
$Ni_{50}Pt_{50}$	1.000	-0.46	11.570	2.494	-0.040
$Ni_{25}Pt_{75}$	1.000	-0.420	11.570	2.494	-0.036

Table 5.08: Charge Transfer Parameters for Ni in NiPt Alloys.

Sample	α_M	$\Delta\beta$	k	R	Charge Transfer (e^-)
$Ni_{75}Pt_{25}$	1.000	0.420	10.390	2.774	0.040
$Ni_{50}Pt_{50}$	1.000	0.2	10.390	2.774	0.019
$Ni_{25}Pt_{75}$	1.000	0.280	10.390	2.774	0.027

Table 5.09: Charge Transfer Parameters for Pt in NiPt Alloys.

The Ni and Pt core level lineshapes could not be analysed in terms of the potential model in chapter 4 and so a comparison with the photoelectron

peak shift analysis in this chapter cannot be made. Here, we have shown that an analysis of the binding energy and Auger peak shifts yields comparable values for each constituent element in NiPt alloys of the charge transfer. It can be seen (Table 5.08 and 5.09) that the magnitude of the charge transfer for the equatorial composition are Ni = -0.02 ± 0.01e^- and Pt = 0.04 ± 0.01e^-. For the 75% Ni specimen, Ni = -0.01 ± 0.01e^- and Pt = 0.04 ± 0.01e^- and for the 25% Ni specimen, Ni = -0.03 ± 0.01e^- and Pt = -0.03 ± 0.01e^-.

5.62 Conclusions Drawn from NiPt

The prediction in chapter 4 that there would be no charge transfer in NiPt alloys is justified, if the results from the Auger and binding energy shifts from the section on CuPt alloys are considered. The magnitude of the charge transfer determined from the Cu and Pt binding energy and Auger shifts was triple that found for the Cu2p core level analysis. If the results here are a factor of three out, then the amount of charge transfer in this alloy system will be negligible within the experimental error. NiPt alloys constituent elements are in the same group in the periodic table and there is no charge transferred from one atom species to another.

In CuPt however, the elements are in adjoining groups and the charge transfer is sizable. It is surprising to note that by altering one element in the alloy with the one next to it in the periodic table (Cu^{29} – Ni^{28}) that such drastically different results are obtained. The Pt4f and Cu2p photoelectron lineshapes in CuPt changed significantly but no change was evident for the Pt4f and only changes in the asymmetry of the Ni2p core level lineshape was evident in NiPt alloys.

5.7 AgPd Binding Energy and Auger Peak Shifts

Ag3d core level lineshapes from pure Ag and various AgPd alloys were analysed in chapter 4. The results for the charge transfer, component splitting and broadening were presented. The amount of charge transfer as a function of the number of unlike neighbours in this alloy system was consistent in magnitude for each alloy composition. This is in expectation of the charge correlated model.

An important factor in the choice of this alloy system was that AgPd alloys do not form any ordered phases throughout their compositional range (Fig 4.14) and so we do not expect that there will be any local order present in the specimens. The local ordering at compositions where there are definite ordered phases was the suggested explanation for the finding that the charge transfer in CuPt alloys was less than expected, particularly for the $Cu_{75}Pt_{25}$ sample.

X-ray photoelectron spectroscopy (XPS) measurements were taken for the Ag3d core levels and the $L_3M_{4,5}M_{4,5}$ Auger line for Ag in AgPd alloys. The Pd3d core levels and $L_3M_{4,5}M_{4,5}$ Auger line for Pd in AgPd alloys were also measured.

Figure 5.10: Ag Auger in AgPd Alloys

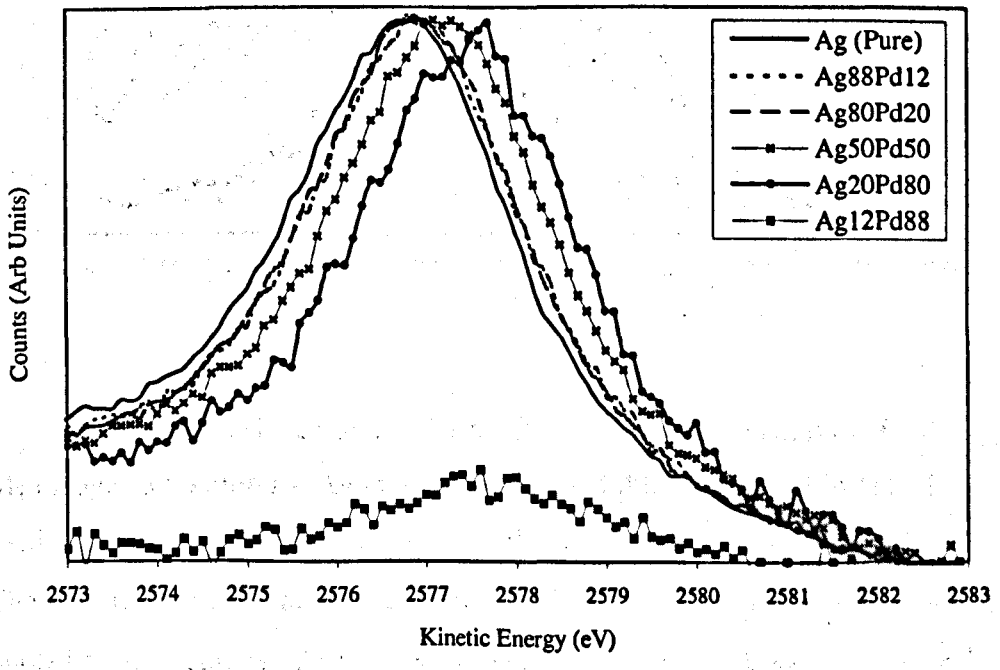

In Fig 5.10 above, the Auger spectra for the Ag $L_3M_{4,5}M_{4,5}$ Auger transition for Ag, $Ag_{12}Pd_{88}$, $Ag_{20}Pd_{80}$, $Ag_{50}Pd_{50}$, $Ag_{80}Pd_{20}$, and $Ag_{88}Pd_{12}$ are shown. The data has been normalised with respect to the vertical Auger peak height for pure Ag except for the $Ag_{12}Pd_{88}$ data where the signal to noise ratio was poor so this data was plotted on a smaller scale.

In 5.11 below, the Auger spectra for the Pd $L_3M_{4,5}M_{4,5}$ Auger transition for Pd, $Ag_{12}Pd_{88}$, $Ag_{20}Pd_{80}$, $Ag_{50}Pd_{50}$, $Ag_{80}Pd_{20}$, and $Ag_{88}Pd_{12}$ are shown. The data has been normalised with respect to the Auger peak height for pure Pd except for the $Ag_{88}Pd_{12}$ data where the signal to noise ratio was poor so this data was plotted on a smaller scale..

Figure 5.11: Pd Auger in AgPd alloys

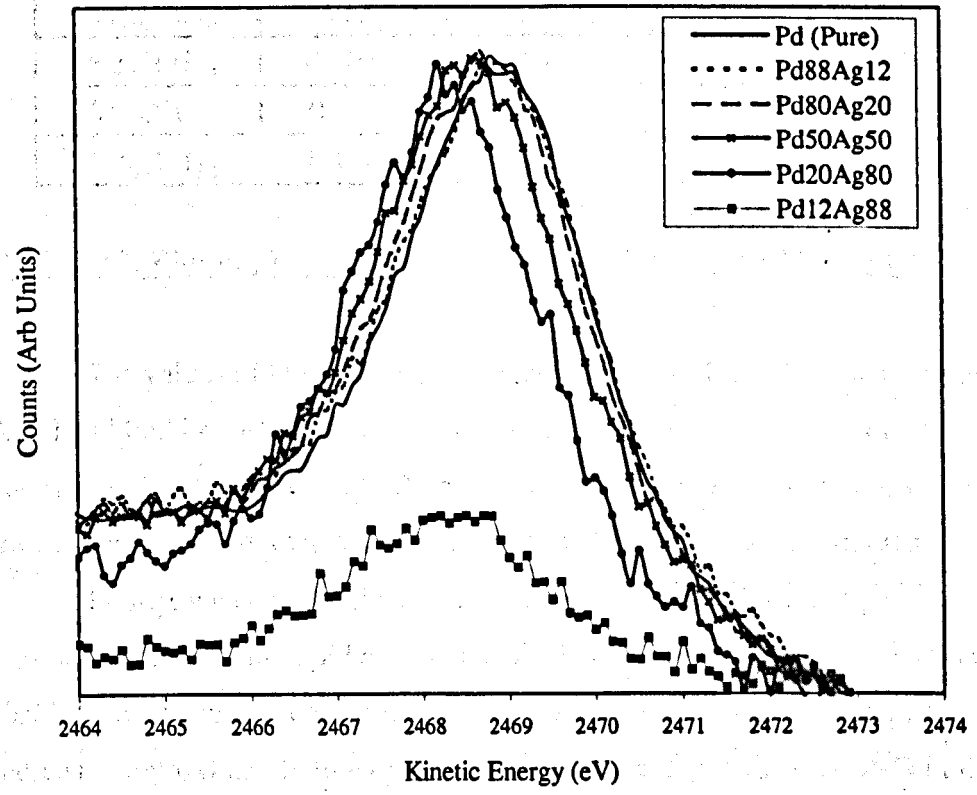

The peak positions and shifts for the Ag3d core level and the $L_3M_{4,5}$ $M_{4,5}$ Auger transition for Ag in AgPd alloys and the Pd3d core levels and $L_3M_{4,5}M_{4,5}$ Auger transition for Pd in AgPd alloys are shown in Table 5.10. The shift in core level binding energy ΔE_b (relative to the pure element) are all quoted to an accuracy of ± 0.02eV. The shift in the Auger kinetic energy ΔE_k

(relative to the main Auger peak for the pure element) are all quoted to an accuracy of ± 0.10eV. The Auger parameter shifts $\Delta\alpha$ (which are a measure of the atomic relaxation) are also quoted to an accuracy of ± 0.10eV.

Ag shifts (3d5/2)			
Sample	ΔE_b	ΔE_k ($L_3M_{45}M_{45}$)	$\Delta\alpha$
$Ag_{12}Pd_{88}$	-0.98	0.69	-0.29
$Ag_{20}Pd_{80}$	-0.91	0.69	-0.22
$Ag_{50}Pd_{50}$	-0.62	0.41	-0.21
$Ag_{80}Pd_{20}$	-0.31	0.10	-0.21
$Ag_{88}Pd_{12}$	-0.18	0.08	-0.10
Pd shifts (3d5/2)			
Sample	ΔE_b	ΔE_k ($L_3M_{45}M_{45}$)	$\Delta\alpha$
$Ag_{12}Pd_{88}$	0.00	0.00	0.00
$Ag_{20}Pd_{80}$	-0.15	-0.13	-0.28
$Ag_{50}Pd_{50}$	-0.20	-0.39	-0.59
$Ag_{80}Pd_{20}$	0.02	-0.71	-0.69
$Ag_{88}Pd_{12}$	0.08	-0.70	-0.62

Table 5.10: Binding Energy and Auger Peak Shifts in AgPd alloys.

The values of the various parameters quoted in Table 5.10 are for the Ag3d and Pd3d photoelectron lines in AgPd alloys. The magnitude of the parameters for the $Ag3d_{3/2}$ and $Ag3d_{5/2}$ were the same and so only the values for the $Ag3d_{5/2}$ are quoted. Similarly, only the $Pd3d_{5/2}$ values are quoted.

Firstly, we consider the binding energy shifts ΔE_b for the Ag photoelectron lines in AgPd alloys. The shift is large with a maximum value of -0.98eV for the lowest concentration AgPd sample. The binding energy shift increases approximately linearly with composition (Fig 5.12). The shift in the Auger peak is also almost linear with composition (Fig 5.12). If we combine the shift of the Auger and core level, we gain a measure of the atomic relaxation (Eq^n 5.09) from the shift in the Auger parameter $\Delta\alpha$. For Ag, the difference in relaxation energy across the compositional range is small, only 0.19eV at its maximum. This effect is negligible considering the error of ± 0.1eV. The screening of a core hole in a Ag atom is therefore very effective.

Figure 5.12: Auger and binding energy shifts of the Ag3d lines as a function of Pd concentration

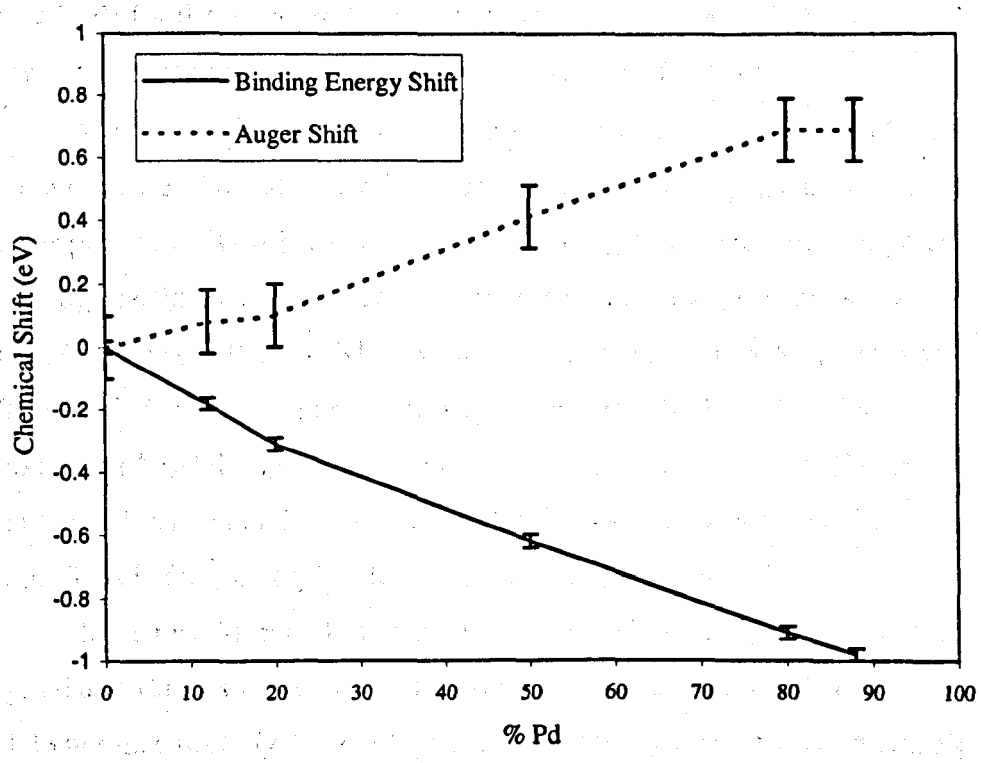

Figure 5.13: Pd Auger and Binding Energy Shifts as a function of Ag concentration

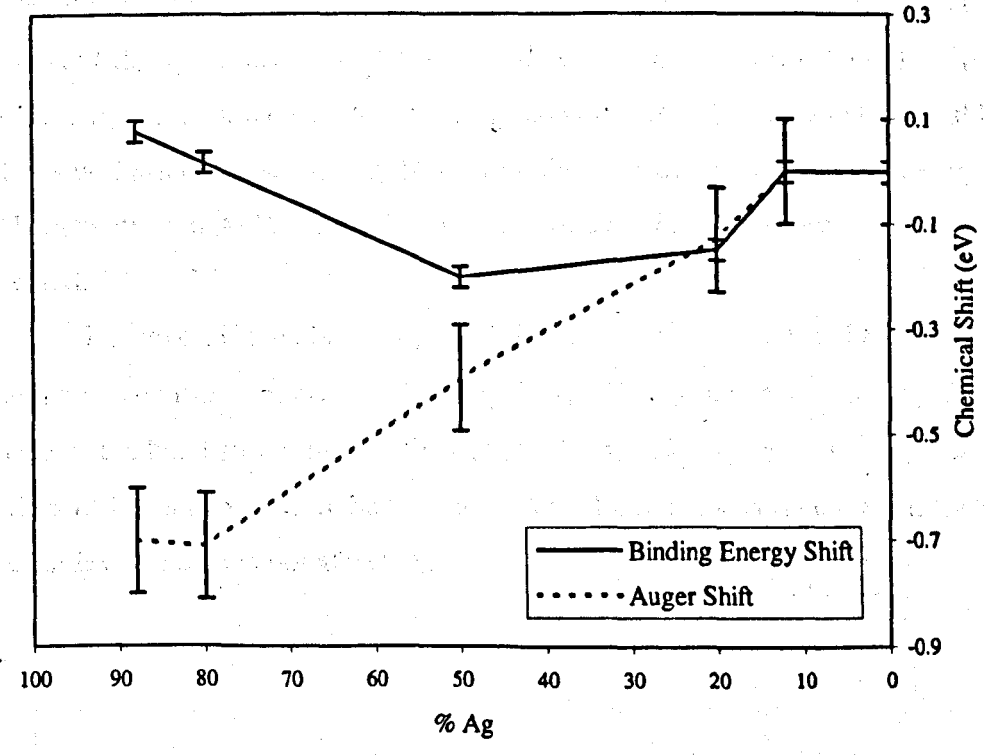

The binding energy shifts ΔE_b for the Pd photoelectron lines in AgPd alloys are far from linear (Fig 5.13). The shift is small with a maximum value of –0.20eV for the equatorial concentration AgPd sample. The Auger shift decreases approximately linearly with composition (Fig 5.13).

We can combine the shifts of the Auger and core level peaks ($\Delta\alpha$), to gain a measure of the atomic relaxation (Eq^n 5.09). For Ag, the difference in Auger parameter is –0.19eV at its maximum ($Ag_{12}Pd_{88}$ specimen compared to $Ag_{88}Pd_{12}$ specimen) therefore, the difference in relaxation energy is small having a value of –0.09eV. The screening of a core hole in a Ag atom is very effective. For Pd, the difference in Auger parameter is –0.69eV at its maximum ($Ag_{80}Pd_{20}$ specimen compared to $Ag_{12}Pd_{88}$ specimen). This means that the difference in relaxation energy for Pd is –0.35eV at its maximum value. This is far greater than for the Ag constituent in AgPd alloys.

If we recall figure 4.18, which showed the valence band spectra for Ag, Pd and various AgPd alloys. It was apparent that the d-bands of Ag and Pd do not mix strongly when alloyed and that the Ag d-band was several eV from the Fermi level and the Pd d-band was at the Fermi level. Therefore, in AgPd alloys low in Pd, the Pd component of the DOS at the Fermi level will be low giving rise to the symmetric lineshape measured from the Pd3d core level at these compositions (Fig 4.16). Also, the s-p band of Ag is in the same region of the spectrum as the d-band of Pd. This change in the d-band for Pd and the increased s-p character of the Ag component in low concentration Pd alloys will affect the screening. If a core hole is created in a Pd atom in a high Pd concentration AgPd alloy, the intense d-band at E_f will screen the hole created.

However, if the alloy is of low Pd concentration, then the d-band cannot screen this core hole sufficiently. This effect is not seen in the Ag data because the band structure near the Fermi level is only s-p in character, which offers little contribution to the screening. The d-band is several eV from the Fermi level and so is not affected.

5.71 Magnitude of the Charge Transfer in AgPd Alloys

The shifts for the Auger and core level photoelectron peaks have been measured and can be used to determine the charge transfer in AgPd alloys. We use the values of the shifts with equations 5.08 and 5.13 to calculate the charge transfer for each element in the alloy. The results are shown for Ag in AgPd alloys in Table 5.11. The results for Pd in AgPd alloys are shown in Table 5.12. The error calculated for the charge transfer parameter was ± 0.01e⁻.

Sample	α_M	$\Delta\beta$	k	R	Charge Transfer (e⁻)
$Ag_{12}Pd_{88}$	1.000	-2.25	9.960	2.896	-0.226
$Ag_{20}Pd_{80}$	1.000	-2.04	9.960	2.896	-0.205
$Ag_{50}Pd_{50}$	1.000	-1.45	9.960	2.896	-0.145
$Ag_{80}Pd_{20}$	1.000	-0.83	9.960	2.896	-0.083
$Ag_{88}Pd_{12}$	1.000	-0.46	9.960	2.896	-0.046

Table 5.12: Charge Transfer Parameters for Ag in AgPd Alloys.

Sample	α_M	$\Delta\beta$	k	R	Charge Transfer (e⁻)
$Ag_{12}Pd_{88}$	1.000	0.00	10.470	2.750	0.000
$Ag_{20}Pd_{80}$	1.000	-0.58	10.470	2.750	-0.055
$Ag_{50}Pd_{50}$	1.000	-0.99	10.470	2.750	-0.095
$Ag_{80}Pd_{20}$	1.000	-0.65	10.470	2.750	-0.062
$Ag_{88}Pd_{12}$	1.000	-0.46	10.470	2.750	-0.044

Table 5.13: Charge Transfer Parameters for Pd in AgPd Alloys.

There was no analysis of the charge transfer for the Pd3d photoelectron lines in chapter 4 and so a comparison between the two approaches cannot be made. However, the charge transfer was determined from analysing Ag3d spectra for AgPd alloys. If we recall Table 4.04: -

SAMPLE	$Ag_{50}Pd_{50}$	$Ag_{88}Pd_{12}$	$Ag_{80}Pd_{20}$
λ/R	0.0018	0.0017	0.0017
λ	0.0050	0.0047	0.0047
Splitting (eV)	0.0923	0.0871	0.0871
Total Broadening (eV)	0.3876	0.3660	0.3660
ChargeTransfer (Q)	0.0594	0.0561	0.0561
SAMPLE	$Ag_{20}Pd_{80}$	$Ag_{12}Pd_{88}$	
λ/R	0.0017	0.0017	
λ	0.0047	0.0047	
Splitting (eV)	0.0871	0.0871	
Total Broadening (eV)	0.3660	0.3660	
ChargeTransfer (Q)	0.0561	0.0561	

We can see that the values of the charge transfer determined from the core level analysis (Table 4.04) and binding energy and Auger peak shifts (table 4.13) do not correspond. This is because the values quoted in Table 4.04 are for a Ag atom surrounded by six Pd and six Ag atoms in the nearest neighbour shell. If we alter the environments in table 4.04 to those that match the composition of the specimens we get (Table 5.14): -

SAMPLE	$Ag_{50}Pd_{50}$	$Ag_{88}Pd_{12}$	$Ag_{80}Pd_{20}$
λ/R	0.0018	0.0017	0.0017
λ	0.0050	0.0047	0.0047
Splitting (eV)	0.0923	0.0871	0.0871
Total Broadening (eV)	0.3876	0.3660	0.3660
ChargeTransfer (Q)	0.0594	0.0135	0.0224
SAMPLE	$Ag_{20}Pd_{80}$	$Ag_{12}Pd_{88}$	
λ/R	0.0017	0.0017	
λ	0.0047	0.0047	
Splitting (eV)	0.0871	0.0871	
Total Broadening (eV)	0.3660	0.3660	
ChargeTransfer (Q)	0.0898	0.0987	

Table 5.14: Charge Transfer (From XPS) for Ag in AgPd Alloys.

Ag Results.

If we compare those values of the charge transfer obtained from the XPS lineshape analysis (Table 5.14) with those obtained from the analysis of the core level and binding energy shifts (Table 5.12) it is apparent that the two sets of results follow the trend expected from the charge correlated model (CCM). For an atom of Ag in AgPd alloys with a low concentration of Ag has the maximum charge transfer and an atom of Ag in AgPd alloys with high Ag concentration the least. The reason for this effect is that an atom of Ag in the lower Ag concentration alloys will have more unlike (Pd) neighbours in the nearest neighbour shell and hence the maximum charge transfer as predicted by the CCM. An atom of Ag in AgPd alloys with a high concentration of Ag will have less unlike (Pd) atoms in the nearest neighbour shell and hence the least charge transfer.

Pd Results.

The Pd binding energy and Auger peak shift analysis yielded the values for the charge transfer for the Pd component in AgPd alloys. These results are found in Table 5.13. The magnitude of the charge transfer for Pd is less than Ag. This is not logical because charge must be conserved and so the amount of charge one alloy component gains the other must lose. The differences in the magnitude of the charge transfer for Pd and Ag are similar to those evident in the CuPt alloy analysis. The reasons why the Pt results were less than the Cu results in CuPt are also true for AgPd and are discussed in the next section.

5.71 Summary of AgPd Results

AgPd alloys form no ordered phases throughout their compositional range (Fig 4.14). This means that there will probably be no local ordering present in AgPd specimens. The magnitude of the charge transfer obtained from the AgPd alloy system should not be reduced as in CuPt alloys by the effect of local ordering in the specimens. The magnitudes of the charge transfer determined from the binding energy and Auger peak shifts are

approximately triple the size of the values gained from the analysis of the Ag3d core level lineshape in chapter 4. The values of the charge transfer obtained from the binding energy and Auger peak shifts follow the trends set by the CCM. The magnitude is greater than expected from the initial Ag3d core level lineshape in chapter 4 and is probably explained by the lack of knowledge of the Fermi level shifts in AgPd alloys. In CuPt and NiPt, there had been no work on the shift in the Fermi level for each element in the alloy with composition. This produced values for the charge transfer in these alloy systems that were three times in magnitude those values obtained from core level lineshape analysis in chapter 4. For AgPd, the values obtained for the charge transfer from the binding energy and Auger peak shifts compared with core level analysis of the Ag3d photoelectron lines are consistent with this.

The charge transfer determined from the Pd binding energy and Auger peak shifts in AgPd alloys are considerably smaller than those determined for the Ag component. One of the reasons for this reduced value of the charge transfer obtained from the Pd photoelectron peak shifts is the determination of k. If we recall section 5.41, equation 5.14 was the definition chosen for k. Work on the Pd3d shifts in the CuPd alloy system [12] showed that the value of k chosen for a free atom differs greatly if we are dealing with s-p or d-band atoms. For a Cu atom in CuPd, the difference between the two values (sp or d-band) can be up to a factor of 2. The method chosen for this work (equation 5.14) gave results for a Cu atom in CuPd alloys that was in between the two extremes. In Pd, the valence structure is mostly d-band in character (Fig 4.18) and so the value of k should be closer to the d-band value (large) than that of the sp-band value (small). It is then reasonable that the Pd charge transfer is less than expected but to arbitrarily change k would lead to misleading results.

5.8 CuPd Binding Energy and Auger Peak Shifts

In chapter 4, the Cu2p photoelectron peaks from various CuPd alloys were measured and the charge transfer determined for the disorder broadening of the lineshape. We now analyse the $Cu2p_{3/2}$ and the Cu $L_3M_{4,5}M_{4,5}$ Auger peak shifts in CuPd alloys and the charge transfer determined using the methodology used for the CuPt, NiPt and AgPd systems earlier in this chapter. The $Pd3d_{5/2}$ and $Pd3d_{3/2}$ core levels and $L_3M_{4,5}M_{4,5}$ Auger peak shifts in CuPd are also measured to determine the charge transfer for the Pd component in the alloy.

The CuPd alloy system has been the subject of a previous study [14] and the analysis of the Cu2p photoelectron lineshape in terms of the potential model in chapter 4 yielded values in good agreement with previous work [13].

Figure 5.14: Cu $L_3M_{4,5}M_{4,5}$ in CuPd alloys.

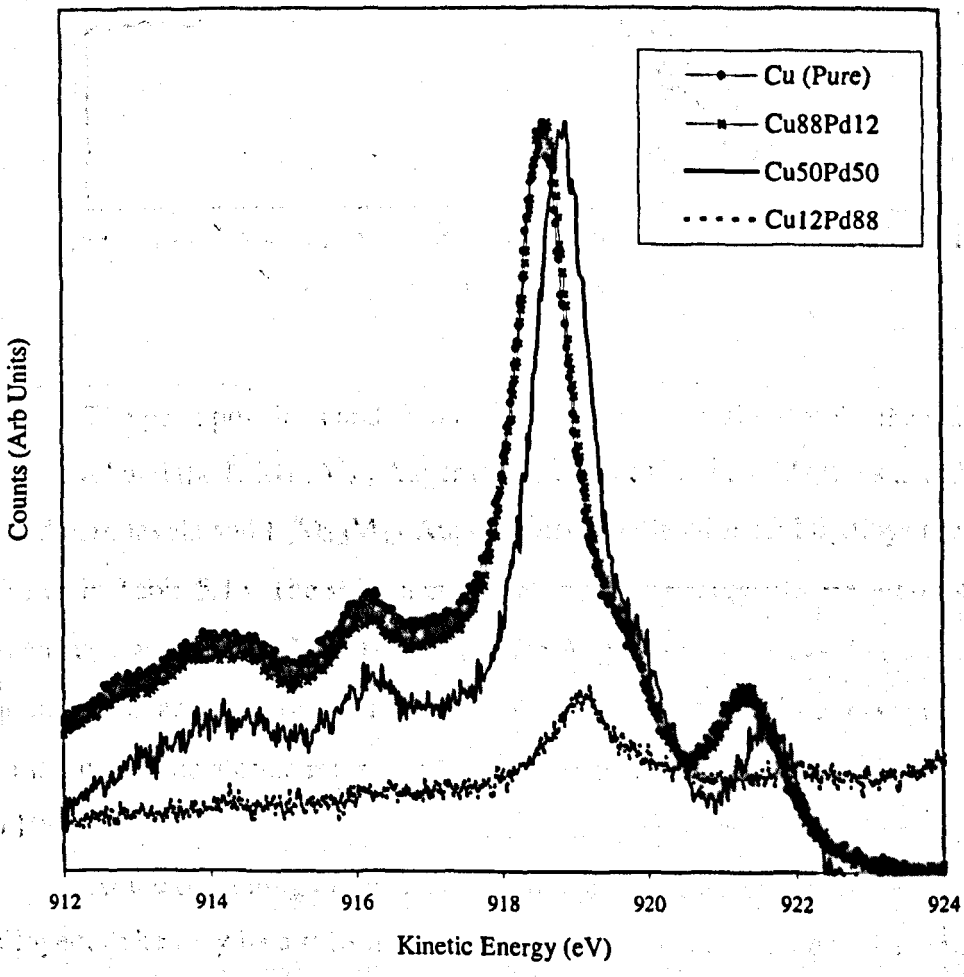

In Fig 5.14, the Cu $L_3M_{4,5}M_{4,5}$ Auger line for Cu, $Cu_{88}Pd_{12}$, $Cu_{50}Pd_{50}$ and $Cu_{12}Pd_{88}$ is shown. In Fig 5.15, the Pd $L_3M_{4,5}M_{4,5}$ Auger line for Pd, $Cu_{88}Pd_{12}$, $Cu_{50}Pd_{50}$ and $Cu_{12}Pd_{88}$ is shown.

Figure 5.15: Pd $L_3M_{4,5}M_{4,5}$ Auger in CuPd alloys

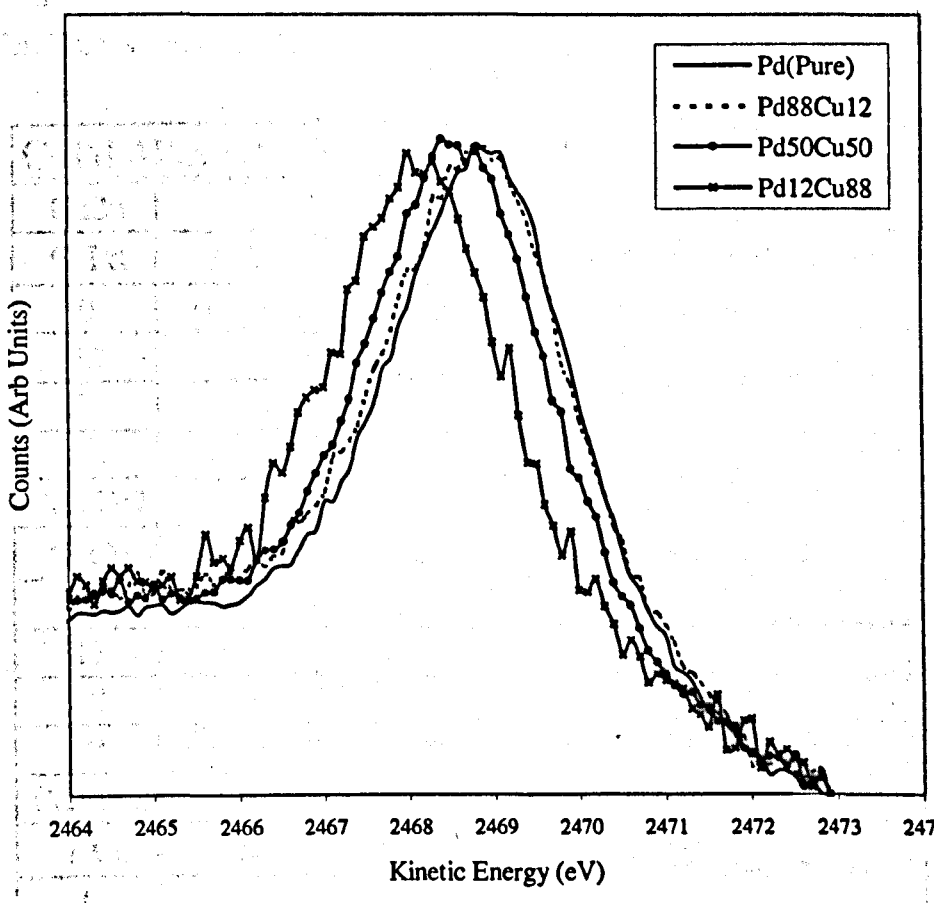

The peak positions and shifts relative to the pure element for the Cu2p core level and the $L_3M_{4,5}$ $M_{4,5}$ Auger transition for Cu in CuPd alloys and the Pd3d core levels and $L_3M_{4,5}M_{4,5}$ Auger transition for Pd in CuPd alloys are shown in Table 5.15. The shift in core level binding energy ΔE_b are all quoted to an accuracy of ± 0.02eV. The shift in the Auger kinetic energy ΔE_k are all quoted to an accuracy of ± 0.10eV. The Auger parameter shifts $\Delta\alpha$ (which are a measure of the atomic relaxation) are also quoted to an accuracy of ± 0.10eV.

At the beginning of this chapter, we noted that when two elements are alloyed, there may be a shift in the Fermi level of each constituent element.

These shifts have been calculated for the CuPd alloy system [7] and the respective binding energy and Auger peaks shifts in Table 5.16 changed to account for the shift in Fermi level (see beginning of chapter for explanation of ΔE_f). The shifts in E_b and E_k must be changed because the positions of the respective peaks are referenced to the Fermi level. Therefore, if there are shifts in the position of the Fermi level the measured positions of the peaks will differ. This is shown in Table 5.15 below.

CuPd Alloys Binding Energy and Auger Shifts			
Cu2p			
% Pd	ΔE_b	ΔE_k	$\Delta\alpha = \Delta E_b + \Delta E_k$
0	0.00	0.00	0.00
12	-0.08	0.07	-0.01
50	-0.64	0.29	-0.35
88	-0.97	0.57	-0.40
Pd3d3/2			
% Cu	ΔE_b	ΔE_k	$\Delta\alpha = \Delta E_b + \Delta E_k$
0	0.00	0.00	0.00
12	0.06	-0.22	-0.16
50	0.19	-0.41	-0.22
88	0.69	-0.83	-0.14
Pd3d5/2			
% Cu	ΔE_b	ΔE_k	$\Delta\alpha = \Delta E_b + \Delta E_k$
0	0.00	0.00	0.00
12	0.06	-0.22	-0.16
50	0.19	-0.41	-0.22
88	0.69	-0.83	-0.14

Table 5.15:- Uncorrected Binding Energy and Auger shifts for CuPd Alloys.

The data in Table 5.15 can be used to gain a measure of the relaxation energy (Equation 5.9) for CuPd alloys. For the Cu component in CuPd alloys, the difference in relaxation energy is at most –0.2eV. This value is similar to that obtained in the previous study of the CuPd alloy system [13]. The shifts in core level binding energy ΔE_b are all quoted to an accuracy of ± 0.02eV. The

shifts in the Auger kinetic energy ΔE_k are all quoted to an accuracy of ± 0.10eV. The Auger parameter shifts $\Delta\alpha$ (which are a measure of the atomic relaxation) are also quoted to an accuracy of ± 0.10eV.

For the Cu component in $Cu_{12}Pd_{88}$, the Auger parameter is at a maximum of -0.4 ± 0.10eV and hence the relaxation energy is only half that with R = -0.2 ± 0.10eV and only a small effect. The maximum relaxation energy for the Pd component was determined for $Cu_{50}Pd_{50}$. The magnitude of the relaxation was found to be -0.1 ± 0.10eV. This is negligible considering the experimental error.

5.81 Fermi Level Shifts in CuPd Alloys

Experimental binding energy shifts (ΔE_b) and Auger shifts (ΔE_k) (relative to the pure element) for solids are usually measured with respect to the Fermi level, while the zero of potential in the charge correlated model corresponds to the 'crystal zero' of the solid. It is therefore necessary to subtract from the measured shifts the contribution due to the to the variation in Fermi energy with alloy composition.

If we add Cu to Pd to form CuPd alloys, we do not expect a significant change in the position of the Fermi level until the Pd d-band is filled. When the Pd d-band is filled additional electrons must be accommodated in the rather flat s-p band. The will cause a slight increase in the Fermi level position with an increase in Cu concentration. Winter *et al* [7] found a ~0.35eV variation in the position of the Fermi level across the compositional range in CuPd alloys.

The corrected binding energy and Auger shifts are in Table 5.16.

Cu2p		
% Pd	ΔE_b	ΔE_k
0	0.00	0.00
12	-0.08	0.07
50	-0.35	0.64
88	-0.60	0.99
Pd3d3/2		
% Cu	ΔE_b	ΔE_k
0	0.00	0.00
12	0.06	-0.35
50	0.29	-0.76
88	0.55	-0.90
Pd3d5/2		
% Cu	ΔE_b	ΔE_k
0	0.00	0.00
12	0.06	-0.35
50	0.29	-0.76
88	0.55	-0.90

Table 5.16: Corrected Values for the Binding Energy and Auger Shifts in CuPd Alloys.

The corrected shifts tabulated above are presented graphically below in Figures 5.16 (Cu shifts) and Figure 5.17 (Pd shifts). Only the shifts for the $Pd3d_{5/2}$ line are presented graphically because the results are identical to those for the $Pd3d_{3/2}$ photoelectron line.

Figure 5.16: Binding and Auger Shifts for Cu2p in CuPd Alloys

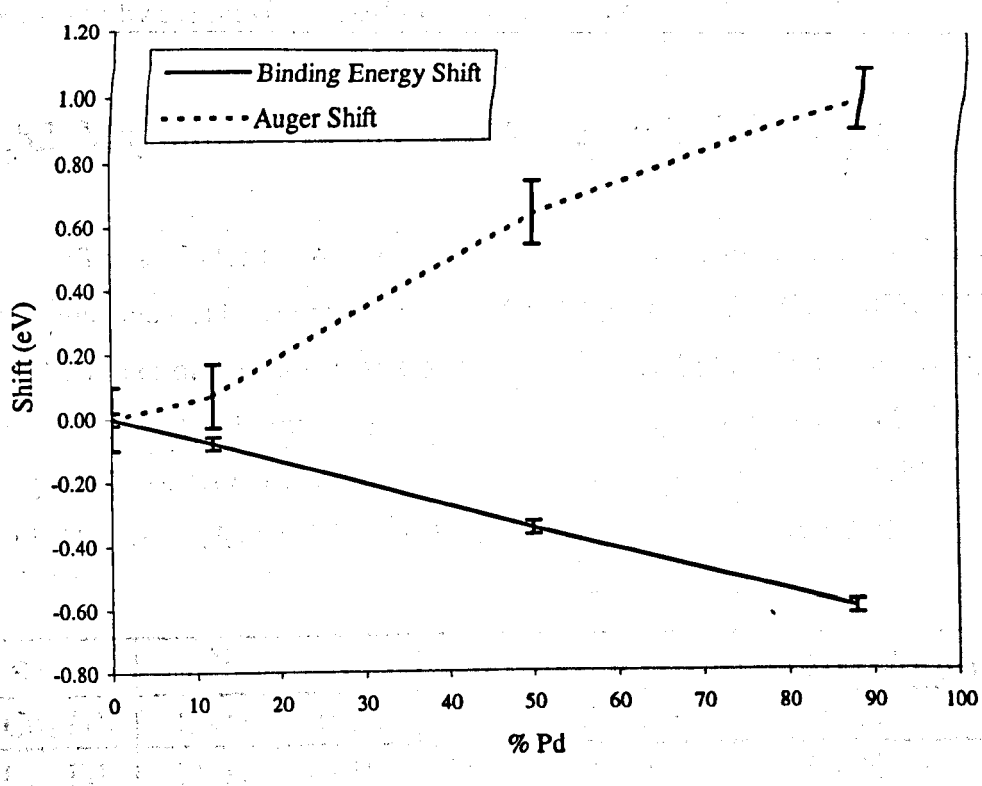

Figure 5.17: Pd3d binding energy and Auger shifts in CuPd alloys.

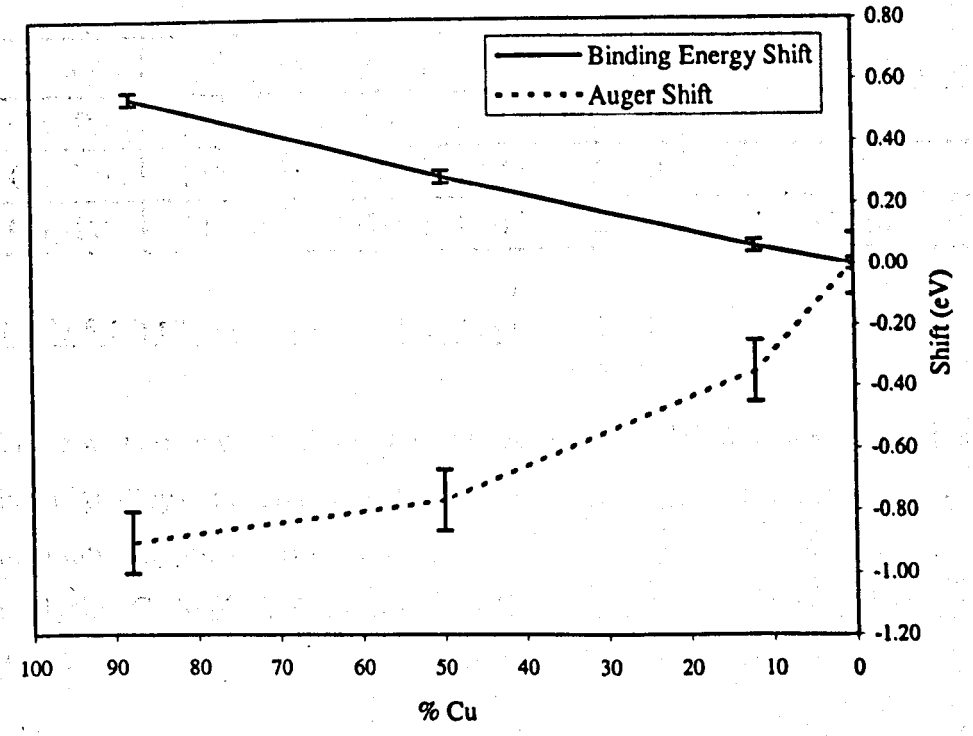

The binding energy and Auger shifts shown in Fig 5.16 and Fig 5.17 for Cu and Pd in CuPd alloys respectively are almost linear with composition. This is borne out by the previous results of Cole *et al* [13].

5.82 Magnitude of Charge Transfer in CuPd Alloys

The shifts for the Auger and core level photoelectron peaks have been measured and can be used to determine the charge transfer in CuPd alloys. We use the values of the shifts with equations 5.08 and 5.13 to calculate the charge transfer for each element in the alloy. The results are shown for Cu in CuPd alloys in Table 5.17. The results for Pd in CuPd alloys are shown in Table 5.18. The error calculated for the charge transfer parameter was $\pm 0.01e^-$.

Sample	α^M	$\Delta\beta$	k	R	Charge Transfer (eV)
$Cu_{88}Pd_{12}$	1.000	-0.170	11.280	2.553	-0.015
$Cu_{50}Pd_{50}$	1.000	-0.410	11.280	2.553	-0.036
$Cu_{12}Pd_{88}$	1.000	-0.810	11.280	2.553	-0.072

Table 5.17: Charge Transfer for Cu in CuPd Alloys.

Sample	α^M	$\Delta\beta$	k	R	Charge Transfer (eV)
$Cu_{88}Pd_{12}$	1.000	0.750	10.470	2.750	0.072
$Cu_{50}Pd_{50}$	1.000	0.110	10.470	2.750	0.011
$Cu_{12}Pd_{88}$	1.000	-0.170	10.470	2.750	-0.016

Table 5.18: Charge Transfer for Pd in CuPd Alloys.

There was no analysis of the charge transfer for the Pd3d photoelectron lines in CuPd alloys in chapter 4 and so a comparison cannot be made with the alternative approach. However, the charge transfer was determined from analysing Cu2p photoelectron spectra for CuPd alloys. If we recall Table 4.06:-

SAMPLE	$Cu_{50}Pd_{50}$	$Cu_{88}Pd_{12}$	$Cu_{12}Pd_{88}$
λ/R	0.0009	0.0009	0.0015
λ	0.0023	0.0023	0.0038
Splitting (eV)	0.0461	0.0461	0.0769
Total Broadening (eV)	0.1938	0.1938	0.3230
ChargeTransfer (Q)	0.0276	0.0276	0.0461

Table 4.06: Charge Transfer Parameters for CuPd Alloys.

We can see that the values of the charge transfer determined from the core level analysis (Table 4.06) and binding energy and Auger peak shifts do not correspond. This is because the values quoted in Table 4.06 are for a Cu atom surrounded by six Pd and six Cu atoms in the nearest neighbour shell. If we alter the environments in table 4.06 to those that match the composition of the specimens we get (Table 5.19): -

SAMPLE	$Cu_{50}Pd_{50}$	$Cu_{88}Pd_{12}$	$Cu_{12}Pd_{88}$
λ/R	0.0009	0.0009	0.0015
λ	0.0023	0.0023	0.0038
Splitting (eV)	0.0461	0.0461	0.0769
Total Broadening (eV)	0.1938	0.1938	0.3230
ChargeTransfer (Q)	0.0276	0.0060	0.0822

The value obtained for the charge transfer in the equatorial and high concentration Cu alloys from the Cu2p photoelectron lineshape are similar to those gained from the binding energy and Auger peak shifts analysis. $0.03 \pm 0.01e^-$ and $0.04 \pm 0.01e^-$ for the $Cu_{50}Pd_{50}$ sample respectively and $0.01 \pm 0.01e^-$ and $0.01 \pm 0.01e^-$ for the $Cu_{88}Pd_{12}$ specimen.

The $Cu_{12}Pd_{88}$ specimen results are similar with values of $0.08 \pm 0.01e^-$ and $0.07 \pm 0.01e^-$ for the magnitude of the charge transfer calculated from core level broadening and binding energy and Auger peak shifts analysis respectively. These results follow the charge correlated model which predicts that the maximum charge transfer will occur when an atom is surrounded by the maximum number of unlike neighbours. For a Cu atom in low Cu

concentration CuPd alloys, the number of unlike (Pd atoms) neighbours in the nearest neighbour shell will be greatest and hence the greater magnitude of the charge transfer. The two methodologies for determining the charge transfer in CuPd alloys yield values that are consistent with each other.

The Pd charge transfer values are consistent with those of Cu, apart from the value obtained for the equatorial composition. The Pd gains $0.02 \pm 0.01e^-$ and the Cu loses $0.04 \pm 0.01e^-$, which is not physical as what one atom gains in charge the other should lose.

5.83 Conclusions Drawn from CuPd

CuPd alloys have ordered phases at certain compositions in their compositional range (Fig 4.21). This means that the specimens at these compositions will have local ordering present ($Cu_{50}Pd_{50}$ and $Cu_{88}Pd_{12}$) in them. The magnitude of the charge transfer obtained from these samples was reduced as in $Cu_{75}Pt_{25}$ specimen by the effect of local ordering in the samples. The Pd binding energy and Auger peak shifts analysis in CuPd alloys (Table 5.17) produced values of the charge transfer that were similar to those for the Cu component in CuPd (Table 5.18) neglecting the $Cu_{50}Pd_{50}$ specimen.

The results obtained in this chapter for the charge transfer for the Cu binding energy and Auger peak shifts are in good agreement with those results determined from the Cu2p photoelectron lineshape analysis in CuPd alloys (chapter 4). The $Cu_{12}Pd_{88}$ sample has the largest value for the charge transfer because this composition is in a region of the phase diagram where there are no ordered phases (Fig 4.21) and also because a Cu atom in this specimen will have the maximum number of unlike neighbours in the nearest neighbour shell in accordance with the CCM.

The magnitude of the charge transfer determined from the binding energy and Auger peak shifts are similar. The results for the equatorial composition differ considerably and this could be because of the definition of k. This explanation also accounted for the differences in the charge transfer obtained for the Pt component in CuPt alloys and Pd component in AgPd alloys.

5.9 References

[1] P.S. Bagus, Phys. Rev. **139** A619-34.

[2] P. Auger, J. Phys. Radium. **6** 205 (1925).

[3] T.D. Thomas and P. Weightman, Phys. Rev. B **33** 5406 (1986).

[4] C.D.Wagner, Faraday Discuss. Chem. Soc. **60** 291 (1975).

[5] J.A. Evans, A.D. Laine, P. Weightman, J.A.D. Matthew, D.A. Woolf, D.I. Westwood and R.H. Williams, Phys. Rev. B **46** 1513 (1992).

[6] N. Lang and A.R. Williams, Phys. Rev. B **20** 1369 (1979).

[7] H. Winter, P.J. Durham, W.M. Temmerman and G.M. Stocks, Phys. Rev. B **33** 2370 (1986).

[8] K. Siegbahn *et al*, ESCA Applied to Free Molecules, North –Holland, Amsterdam, (1969).

[9] U. Gelius, Phys. Scr. **9** 133 (1973).

[10] R. Magri, S.H. Wei and A. Zunger, Phys. Rev. B **42** 11388 (1990).

[11] R.J. Cole and P. Weightman, J. Phys: Condens. Matter **6**, 5783 (1994).

[12] R.J. Cole, N.J. Brooks and P. Weightman, Phys. Rev. B **52** 2976 (1995).

[13] R.J. Cole, N.J. Brooks and P. Weightman, Phys. Rev. B **56** 12178 (1997).

[14] R.J. Cole, N.J. Brooks and P.Weightman,Phys. Rev. Lett. **78**, 3777 (1997).

CHAPTER 6.

Final Conclusions

6.1 Conclusions from XPS, Binding Energy and Auger Peak Shifts Analysis

The analysis of core level spectra measured using XPS was conducted in chapter 4 for CuPt, NiPt, AgPd and CuPd alloys. The same alloy systems were analysed using binding energy and Auger peak shifts in chapter 5. The conclusions from such analysis are as follows.

CuPt Alloy Results

The broadening was largest for the $Cu_{50}Pt_{50}$ composition as expected on the basis of the correlated charge model (CCM). The CCM predicts that equal broadening should be observed in $Cu_{75}Pt_{25}$ and $Cu_{25}Pt_{75}$. However, we observed the $Cu2p_{3/2}$ line to be significantly narrower in $Cu_{75}Pt_{25}$ a finding we attribute to the presence of local ordering in the $Cu_{75}Pt_{25}$ specimen since the phase diagram shows an ordered phase at this composition [1].

A detailed analysis of the broadening in terms of the CCM yields values of the charge transfer parameter λ/R of $1.5x10^{-3}$ and $1.2x10^{-3}$ for $Cu_{50}Pt_{50}$ and $Cu_{25}Pt_{75}$, which as expected from the CCM, are compatible within the experimental uncertainty of $\pm 0.20x10^{-3}$. The smaller value of this parameter $0.95x10^{-3}$ obtained from the analysis of the results for $Cu_{75}Pt_{25}$ will be an underestimate if, as expected, ordering was present in this specimen.

The charge transfer values quoted in Table 4.02 were for a Cu atom surrounded by six unlike and six like neighbours in the nearest neighbour shell. The $Cu_{25}Pt_{75}$ and $Cu_{50}Pt_{50}$ values are consistent within the experimental errors, but the $Cu_{75}Pt_{25}$ value is inaccurate. This magnitude of the charge transfer will be affected by the presence of local ordering in the sample.

The Pt4f photoelectron lines in CuPt alloys could not be analysed using our fitting function because of the highly asymmetric lineshapes obtained from these core levels.

The magnitude of the charge transfer determined from binding energy and Auger peak shifts (for the Cu component) are approximately 30% of those values obtained from the Cu2p core level photoelectron lineshape analysis in CuPt alloys; carried out in chapter 4. These differences were explained in

terms of the neglect of the shifts in the Fermi level as Cu and Pt are alloyed. The Fermi level shifts for the CuPt alloy system have not been calculated and there is no way of accounting for them. The magnitudes of the charge transfer obtained using the methodology are an overestimate, if those obtained from the core level lineshape analysis are taken as the true values.

However, the magnitudes of charge transfer determined for the Pt components in CuPt alloys are surprising. The values were in agreement with those obtained from the Cu2p core level analysis. This corresponds well with the earlier declaration that what one alloy component gains in charge the other must lose. The values of the charge transfer determined from spectral peak shifts are much less for the Pt than those obtained for the Cu component in CuPt alloys.

One of the reasons for this reduced value of the charge transfer obtained from the Pt photoelectron peak shifts is the determination of k. If we recall section 5.41, equation 5.14 was the definition chosen for k. However, work on the Cu2p shifts in the CuPd alloy system [12] showed that the value of k chosen for a free atom differs greatly if we are dealing with s-p or d-band atoms. For Cu, the difference between the two values can be up to a factor of 2. The method chosen for this work (equation 5.14) gave results for the Cu component in CuPd alloys, which was in between the two extremes. In Pt, the valence structure is mostly d-band in character (Fig 4.06) and so the value of k chosen will be an underestimate of what it should be. If this effect were taken into account and k was increased, the charge transfer determined from equation 5.14 would increase. It is then reasonable that the Pt charge transfer is less than expected but to arbitrarily change k would lead to misleading results.

This model (equation 5.14) for k gives larger values for the charge transfer for Cu shifts in CuPt alloys compared with the Cu2p core level analysis in chapter 4. For Pt the d-band is at the Fermi level and so will mix with the s-p band of Cu. Any change in the two will lead to s-p and d-band changes which will alter the atomic parameters such as k considerably. This is why the magnitude of the Pt charge transfer in CuPt alloys is lower than those obtained for the Cu spectral peak shifts analysis. Why the magnitude of the charge transfer is larger than those obtained from the Cu2p core level

lineshape is probably mostly due to the fact that no Fermi level shifts were included in this work. If the shifts had the effect of decreasing the binding energy and Auger shifts, then the amount of charge transfer would be reduced, significantly.

NiPt Alloy Results

The Ni and Pt photoelectron lines in NiPt like the Pt core levels in CuPt could not be analysed using our fitting procedure because of the highly asymmetric lineshapes obtained from these alloy components. The Auger and binding energy shifts as a function of composition were analysed in chapter 5 and give insight into the size of the charge transfer in this alloy system.

It was expected from a visual analysis of the XPS spectra (Fig 4.11 and Fig 4.12) from the core levels of Ni and Pt in NiPt alloys and an inspection of the Ni and Pt bandstructure that the magnitude of the charge transfer would be negligible in this alloy system. The prediction in chapter 4 that there would be no charge transfer in NiPt alloys is justified, if the results from the Auger and binding energy shifts from the section on CuPt alloys are considered. The magnitude of the charge transfer determined from the Cu and Pt binding energy and Auger shifts was triple that found for the Cu2p core level analysis. If the results here are a factor of three out, then the amount of charge transfer in this alloy system will be negligible within the experimental error. NiPt alloys constituent elements are in the same group in the periodic table and we expect charge transferred from one atom species to another to be small.

The NiPt alloy system was a vital part of this work as it showed that when the electronic structure of the two elements that are alloyed are similar that very little charge transfer is induced in the alloy. Admittedly the core level lineshapes could not be analysed but the Auger and binding energy shifts reinforced the fact that no charge transfer was present in this alloy.

In CuPt however, the elements are in adjoining groups and the charge transfer is sizable. It is surprising to note that by altering one element in the alloy with the one next to it in the periodic table (Cu^{29} – Ni^{28}) that such drastically different results are obtained but yet understandable considering

their drastically different bandstructure. The Pt4f and Cu2p photoelectron lineshapes in CuPt changed significantly but no change was evident for the Pt4f and Ni2p core level lineshapes in NiPt alloys.

AgPd Alloy Results

The values obtained from the XPS lineshape analysis in chapter 4 for the broadening and charge transfer are greater for AgPd alloys (Table 4.04) than those of CuPt alloys (Table 4.02). This was postulated earlier when the bandstructure and phase diagrams were studied. If we consider the broadening of the component peaks that make up the bulk contribution to the core level lineshape, in AgPd alloys, the broadening is ~0.4eV throughout the compositional range (Table 4.04) compared with CuPt alloys that at most have a broadening of ~0.3eV (Table 4.02). One reason for this is the fact that AgPd alloys have no ordered phases throughout the compositional range [3]. There will be no tendency for local order to occur in specimens of this alloy system and so all site environments are present. However, in CuPt alloys, there were ordered phases at certain compositions, which meant that only specific site environments were present in the specimens of this species.

In table 4.04, the charge transfer for a Ag atom with six unlike (Pd) neighbours in varying alloy compositions was quoted. It was clear that in all sample compositions, the amount of charge transfer from Ag to a Pd atom for this environment was the same in magnitude. This was not the case for CuPt alloys, where the charge transfer in all alloy compositions, for a Cu atom surrounded by six Pt atoms differed. We inferred that this was due to the tendency for local ordering to occur at the $Cu_{75}Pt_{25}$ composition and differences in the component elements electronic structure. The charge transfer in AgPd alloys is approximately 25% larger than that in CuPt alloys.

The magnitudes of the charge transfer determined from the binding energy and Auger peak shifts are (like those values obtained for CuPt and NiPt) approximately triple the size of the values gained from the analysis of the Ag3d core level lineshape in chapter 4. The values follow the trends set by the CCM and why the magnitude is greater than expected is explained by the lack of knowledge of the Fermi level shifts in AgPd alloys. In CuPt and NiPt, there had been no work on the shift in the Fermi level for each element in the

alloy with composition. This produced values for the charge transfer in these alloy systems that were three times in magnitude those values obtained from core level lineshape analysis in chapter 4. For AgPd, the values obtained from the binding energy and Auger peak shifts compared with core level analysis of the Ag3d photoelectron lines are consistent with this systematic error. The important point is that the values follow the trend as set by the CCM.

The Pd results for the charge transfer determined from the binding energy and Auger peak shifts are considerably smaller than those acquired for Ag. One of the reasons for this reduced value of the charge transfer obtained from the Pd photoelectron peak shifts is the value used for k. This was one of the reasons why the results for the Pt charge transfer in CuPt alloys were so small.

If we recall section 5.41, equation 5.14 was the definition chosen for k. However, work on the Pd3d shifts in the CuPd alloy system [2] showed that the value of k chosen for a free atom differs greatly if we are dealing with s-p or d-band atoms. The method chosen for this work (equation 5.14) gave results for the Cu component in CuPd alloys, which was in between the two extremes. In Pd, the valence structure is mostly d-band in character (Fig 4.18) and so the value of k chosen will be an underestimate of what it should be. If k was increased the charge transfer determined from equation 5.14 would increase. It is then reasonable that the Pd charge transfer is less than expected but again, to arbitrarily change k would lead to misleading results.

For Pd the d-band is at the Fermi level and so will mix with the s-p band of Ag [4]. Any change in the two separate DOS will lead to large differences in atomic parameters such as k. This is why the magnitude of the Pd charge transfer in AgPd alloys is lower than expected.

CuPd Alloy Results

It was found from the XPS core level lineshape analysis in chapter 4 that the values obtained for the charge transfer and core level broadening for the high concentration Cu alloys was much less than for the $Cu_{12}Pd_{88}$ sample. This was probably due to the ordered phases at these compositions, which may lead to local ordering in the specimens at these concentrations. The values of the charge transfer, bulk component splitting

and core level broadening found were comparable with those obtained from the CuPt samples analysis and the work of Cole *et al* [7,10,11,12] on CuPd. The results obtained for the core level broadening of the Cu2p lines in CuPd and CuPt specimens are very similar and it was apparent that the charge transfer in both systems was of the same magnitude where no ordering was present in the alloys.

In AgPd alloys, there was no ordered phases that could result in local order in the specimens. The magnitude of the charge transfer was larger for AgPd than for CuPt or CuPd, even in the Cu based samples where no ordered phases were present. The magnitude of the broadening in CuPd alloys was similar to that in CuPt alloys, but less than in AgPd alloys with values of approximately 0.3eV, 0.3eV and 0.4eV respectively. This trend was seen in the magnitude of the charge transfer, which was quoted for an atomic site that has six unlike neighbours. Values of $0.045e^-$, $0.045e^-$ and $0.06e^-$ for CuPd, CuPt and AgPd respectively were obtained.

CuPd alloys form ordered phases throughout their compositional range (Fig 4.21). This means that the specimens at these compositions will have local ordering present ($Cu_{50}Pd_{50}$ and $Cu_{88}Pd_{12}$) in them. The magnitude of the charge transfer obtained from these samples was reduced as in $Cu_{75}Pt_{25}$ specimen by the effect of local ordering in the samples.

The analysis of the Pd binding energy and Auger peak shifts analysis in CuPd alloys (Table 5.17) produced values of the charge transfer that were similar to those for the Cu component in CuPd (Table 5.18) neglecting the $Cu_{50}Pd_{50}$ specimen.

The results obtained for the charge transfer for the Cu binding energy and Auger peak shifts are in good agreement with those results determined from the Cu2p photoelectron lineshape analysis in CuPd alloys (chapter 4). The $Cu_{12}Pd_{88}$ sample has the largest value for the charge transfer because this composition is in a region of the phase diagram where there are no ordered phases (Fig 4.21) and also because a Cu atom in this specimen will have the maximum number of unlike neighbours in the nearest neighbour shell in accordance with the CCM.

The magnitude of the charge transfer determined from the binding energy and Auger peak shifts are similar. The results for the equatorial

composition differ considerably and this could be because of the definition of k. This explanation also accounted for the differences in the charge transfer obtained for the Pt component in CuPt alloys and Pd component in AgPd alloys.

6.2 Overall Results and Conclusions from the Four Alloy Systems

The greatest effect on the results obtained for the magnitude of the charge transfer from the analysis of core level lineshapes for the four alloy samples was the presence of local ordering in the specimens. CuPt, NiPt and CuPd all have ordered phases throughout their compositional range. This probably meant that there would be a tendency for local order to occur in the specimens from these three alloys at compositions where ordered phases were present. AgPd has no ordered phases present in its phase diagram and the results of the charge transfer in this alloy system were identical for each composition for an atom in a specific nearest neighbour environment. The other alloy systems were affected by local order as the magnitude of the charge transfer for alloy compositions where ordered phases were present was greatly reduced.

The analysis of the binding energy and Auger peak shifts produced values for the charge transfer that were three times the magnitude of those obtained from the core level analysis for CuPt, NiPt and AgPd. The results followed the predictions of the charge correlated model but were greater than expected from the values gained from the core level lineshape analysis. The results from the binding energy and Auger peak shifts analysis for the CuPd alloy system did not have this systematic error. This was because the Fermi level shift with composition had been calculated for this alloy system. If such calculations had been done for the other three alloy systems, we would expect to remove this systematic error.

6.2 References

[1] T.B. Massalski, H. Okamoto, P. R. Subramanian and L. Kacprzak. Binary Alloy Phase Diagrams 2nd Edition, **2** pp 1460-1462 (ASM International 1990).

[2] R.J. Cole, N.J. Brooks and P. Weightman, Phys. Rev. B **52** 2976 (1995).

[3] T.B. Massalski, H. Okamoto, P. R. Subramanian and L. Kacprzak. Binary Alloy Phase Diagrams 2nd Edition, **2** pp 72-74 (ASM International 1990).

[4] P. Weightman, P.T. Andrews, G.M. Stocks and H. Winter. J. Phys. C. Solid State Phys. **16** L81 (1983).

[5] R.J. Cole, N.J. Brooks and P.Weightman,Phys. Rev. Lett. **78**, 3777 (1997).

[6] R.J. Cole, N.J. Brooks and P.Weightman,Phys. Rev. B **56**, 12178 (1997).

[7] R.J. Cole and P. Weightman,J. Phys: Condens. Matter **9**, 5609 (1997).

[8] R.J. Cole and P. Weightman,J. Phys: Condens. Matter **10**, 5679 (1998).

6.3 Publications from this Work

[1] "Disorder broadening of core level photoemission spectra in Cu_xPt_{1-x} alloys."
A.W. Newton, A. Vaughan, R.J. Cole and P. Weightman.
Journal of Electron Spectroscopy and Related Phenomena. **107** 185 (2000).